TECHNISCHE UNIVERSITÄT DRESDEN

Microwave Photonic Applications – From Chip Level to System Level

Dr.-Ing. Niels Neumann

Fakultät Elektrotechnik und Informationstechnik
der Technischen Universität Dresden
zur Erlangung des akademischen Grades

Doktoringenieur habilitatus
(Dr.-Ing. habil.)

genehmigte Habilitation

Vorsitzender:	Prof. Dr.-Ing. habil. Jürgen Czarske
Gutachter:	Prof. Dr.-Ing. Dirk Plettemeier
	Prof. Dr. Juan Jose Vegas Olmos
	Prof. Dr.-Ing. Christian-Alexander Bunge

Tag der Einreichung:	10.12.2018
Tag des Vortrags mit Kolloquium:	29.09.2020

Diese Habilitationsschrift ist als Buch (ISBN 978-3-959470-42-1) im Jörg Vogt Verlag (http://www.vogtverlag.de) erschienen.

This habilitation is available as printed edition (ISBN 978-3-959470-42-1) from Jörg Vogt Verlag (http://www.vogtverlag.de).

Abstract

The hybridization between microwave and optical technologies – microwave photonics – is an emerging field with high potential. Benefitting from the best of both worlds, microwave photonics has many use cases and is just at the beginning of its success story. The availability of a higher degree of integration and new technologies such as silicon photonics paves the way for new concepts, new components and new applications.

In this work, first, the necessary basic building blocks – optical source, electro-optical conversion, transmission medium and opto-electrical conversion – are introduced. With the help of specific application examples ranging from chip level to system level, the electro-optical co-design process for microwave photonic systems is illustrated. Finally, future directions such as the support of electrical carriers in the millimeter wave and THz range and realization options in integrated optics and nanophotonics are discussed.

Contents

List of Figures

List of Tables

Nomenclature

AC	Alternating Current
AGC	Automatic Gain Control
APD	Avalance Photodiode
ASK	Amplitude Shift Keying
BER	Bit-Error Rate
BS	Base Station
CPU	Central Processing Unit
CS	Central Station
CW	Continuous Wave
DBR	Distributed Bragg-Reflector
DC	Direct Current
DFB	Distriubuted Feedback Laser
DGD	Differential Group Delay
DNA	Deoxyribonucleic acid
DP-QPSK	Dual Polarization Quarternary Phase Shift Keying
DPMZM	Dual Parallel Mach-Zehnder Modulator
DSB	Double Side-Band
DWDM	Dense Wavelength Division Multiplex
E/O	electro-optical
ECL	External Cavity Laser
EDFA	Erbium Doped Fiber Amplifier
EPIC	Electronic-Photonic Integrated Circuit
ESA	Electrical Spectrum Analyzer
FBG	Fiber Bragg Grating
FTTA	Fiber-to-the-Antenna
FWHM	Full Width at Half Maximum
FWM	Four-Wave Mixing
HD	High Definition
HPBW	Half Power Beam Width
HPC	High Performance Computing
IC	Integrated Circuit
IF	Intermediate Frequency
IL	Insertion Loss
IQ	Inphase and Quadrature
ISM	Industrial, Scientific and Medical
LAN	Local Area Network
LDD	Laser Diode Driver

LED	Light-Emitting Diode
LF	Low Frequency
LNA	Low-Noise Amplifier
LO	Local Oscillator
LPG	Long-Period Grating
MDM	Mode Division Multiplex
MIMO	Multiple Input Multiple Output
MMF	Multi-Mode Fiber
mPSK	m-ary Phase Shift Keying
mQAM	m-ary Quadrature Amplitude Modulation
MS	Mobile Station
MUX	Multiplexer
MZI	Mach-Zehnder Interferometer
MZM	Mach-Zehnder Modulator
NOC	Network on Chip
NRZ	Non-Return to Zero
O/E	opto-electrical
OAM	Optical Angular Momentum
ODSB-SC	Optical Double Side-Band modulation with Suppressed Carrier
OFDM	Orthogonal Frequency Division Multiplexing
OFDR	Optical Frequency Domain Reflectometry
OM3	Optical Multi-Mode Fiber, Class 3
OOK	On-Off Keying
OSA	Optical Spectrum Analyzer
OTA	Over-the-Air
PCB	Printed-Circuit Board
PE	Polyethylene
PIC	Photonic Integrated Circuit
PMD	Polarization Mode Dispersion
QPSK	Quadrature / Quaternary Phase Shift Keying
RAU	Remote Antenna Unit
RF	Radio Frequency
RIN	Relative Intensity Noise
RMS	Root Mean Square
RoF	Radio-over-Fiber
ROP	Received Optical Power
RRH	Remote Radio Head
Rx	Receiver
RZ	Return to Zero
SBS	Stimulated Brillouin Scattering
SDM	Spatial Division Multiplex
SMA	Sub-Miniature version A
SMF	Single-Mode Fiber
SMSR	Side-Mode Suppression Ratio

SNR	Signal-to-Noise Ratio
SOI	Silicon-on-Insulator
SPM	Self-Phase Modulation
SPR	Surface-Plasmon Resonance
SRS	Stimulated Raman Scattering
SSB	Single Side-Band
TE	Transverse Electric
TIA	Trans-Impedance Amplifier
TM	Transverse Magnetic
TSV	Through Silicon Via / Through Substrate Via
TTD	True Time Delay
Tx	Transmitter
UWB	Ultra Wide-Band
VCSEL	Vertical Cavity Surface-Emitting Laser
VOA	Variable Optical Attenuator
WDM	Wavelength Division Multiplex
XPM	Cross-Phase Modulation

1 Introduction

The invention of the semiconductor laser[1] was the nucleus for optical communication systems to replace their electrical counterparts. The use of light as carrier has some major advantages over traditional electrical systems. In optical domain, there is nearly unlimited bandwidth available. One major application is the transmission of enormous amounts of data over long distance with low loss. Additionally, the optical signal can be modified and transformed (e.g. generating electrical carriers, filtering and sensing). However, information processing and memory are still realized in electrical domain.

Wireless RF signals are advantageous in lots of applications. That means, efficient electro-optical and opto-electrical conversion is needed when used together with optical transmission. Achieving the best system performance requires a careful balance of electrical and optical parts. This is not possible without a proficient co-design of optical and RF building blocks, the field of microwave photonics. This work contributes to the growing interest in that kind of systems. From chip-level with distances in the micrometer range over board-level applications (centimeter) to access systems spanning over kilometers, microwave photonic solutions can be found benefitting from the heritage in data center and backbone communication systems.

Long-haul systems are operated in the second (at 1.3 $\mu\mathrm{m}$ wavelength) and third optical window at a wavelength of about 1.5 $\mu\mathrm{m}$. Single-mode silica fibers ensure maximum performance. Linear (chromatic dispersion, polarization mode dispersion and attenuation) as well as nonlinear effects impair the transmitted signal. In the second optical window, the chromatic dispersion has its minimum for standard single-mode fiber while the third optical window is located at the attenuation minimum. Not only is mode dispersion avoided by the single-mode operation but also devices based on mode coupling such as gratings can be conveniently used. Among other applications, this enables sharp filters for dense wavelength division multiplexing (DWDM).

Data centers set completely different demands: Transmission distances stay well below 10 km but connectivity is crucial. Requirements for signal distortions are relaxed so that multi-mode fibers can be used. Connector technology can be more cost-effective and simpler due to lower needs for mechanical precision because of the bigger fiber diameters. Data center systems usually work in the first optical window at 850 nm wavelength. They are designed in an economical way with a lower accumulated data rate per fiber. That's because of working with lower line rates and less spectrally efficient modulation formats. Moreover, only a small number of WDM channels are used.

Expanding into smaller and smaller transmission distances, optical systems face multiple constraints when serving for chip-to-chip and on-chip applications. While

[1] an acronym for "light amplification by stimulated emission of radiation"

the board-to-board communication and on-board systems have been influenced by the data center based paradigm (multi-mode waveguides and low spectral efficiency), the chip-level feature sizes impose single-mode waveguides. Silicon as omnipresent material can be used as waveguide material for wavelengths larger than 1 $\mu\mathrm{m}$. However, in the silicon photonics scenario, the light source is one of the major challenges. Silicon is an indirect bandgap material. That makes it a big challenge to build an efficient silicon based laser. Hence, mostly external III-V lasers are used nowadays. In order to include lasing functionality to silicon based chip technology, multiple approaches are followed to integrate III-V technology to silicon substrates for wafer-level manufacturing. Thick buffers grown between Si and InGaAs help to adjust the lattice mismatch and decrease the number of crystalline defects. A costly alternative is the direct wafer bonding.

The use of optical waveguides such as fibers limits the optical systems to static or quasi-static applications. Linking them with wireless technology overcomes this drawback and allows reconfigurable and portable solutions. Mobile connectivity is the main cause for growth rates in terms of bandwidth and number of devices. However, only the last meters from the base station to the mobile unit are transmitted over the air. The rest of the network is realized largely in optical domain in order to meet the challenging performance demands. Microwave photonic technologies such as carrier generation, electro-optical conversion and signal processing using photonics can be used to simplify the network design. Moreover, for shorter distances (e.g. for board-to-board communication), wireless approaches like beam steering / beam switching can be applied to adaptively distribute a data stream to many different locations. This kind of large-scale integration between optical and radio techniques is only possible with microwave photonics.

In this work, important aspects of microwave photonic systems are studied in showcase scenarios. First, the required building blocks are briefly introduced in chapter 2. The implications of applying the well-known parts liker lasers, modulation, typical transmission media and opto-electrical conversion in the context of microwave photonics are discussed. Following, the broad field where microwave photonic systems can be deployed is illustrated with the help of examples for chip-level, board level and system level operation in chapter 3. These examples cover ultra-short transmission distances from a few hundred micrometers (through silicon vias) to tens of kilometers (Radio-over-Fiber systems). At the same time, the different options of using the optical medium just for transmission (chip-level intraconnects), to connect photonics seamlessly with wireless technology (fiber-to-the-antenna), to introduce photonic RF generation (with Talbot effect and in the Radio-over-Fiber system) or to attach an electrical read-out to optical sensors in order to enhance the fields of application are presented. Finally, the outlook in chapter 4 describes how to push microwave photonics to higher frequencies in the THz region and to smaller scales in nanophotonics.

2 Basics of microwave photonic systems

All microwave photonic systems have one basic structure in common. Input and output to microwave photonic systems are electrical signals – all data sources, computing units, memories and most of the routers as well as many sensors are realized in electronics. However, the electrical signal has to be converted to optical domain (i.e. electro-optically modulated) in order to use photonics. So, first, a light source serving as carrier for the payload signal is needed. The core part of the microwave photonic system is the transmission or modification of this optical signal before it gets transformed back to electrical domain. In the following sections, the physical basics of these parts and their influence on the system behavior are discussed.

2.1 Light source

Microwave photonics systems require reliable light sources that can be efficiently coupled into optical waveguides. Fiber lasers are one option but are only employed in some niche functions, e.g. comb generation, due to their comparably complex setup and susceptibility to environmental conditions like temperature drifts and vibrations. They are not targeted in the subsequent elaboration. Semiconductor based devices are more stable, cheaper and mass-market compatible. Most of the microwave photonic applications imply high frequencies supporting large data rates. That's why light emitting diodes (LEDs) will not be focused here as well. Generally, they can be used just the same way as laser diodes tolerating their worse performance due to their broader spectral width.

Consequently, the dominating light source for optical communication is the semiconductor laser. Lasers consist of an active medium which provides gain and a resonator that enables the coherent light amplification. Especially for short active regions, the gain is comparably small and the optical cavity provides feedback that boosts the amplification. The gain medium receives its power electrically or optically. The lasers can be classified based on their cavity type, material and geometry.

Figure 2.1 shows the general setup of typical semiconductor lasers. On the left side, an edge-emitting laser with a Fabry-Perot resonator formed by two mirrors is shown. Its output mirror is partially reflecting. On the right side, a surface-emitting laser with distributed Bragg reflectors (DBR) is depicted. It is commonly refered to as vertical-cavity surface-emitting laser (VCSEL). The distributed reflection leads to an effective length of the cavity that is smaller than the geometrical length of the structure.

The general principle of both lasers is the same: The light travels within the cavity (characterized by its length L, attenuation α and propagation constant β) between

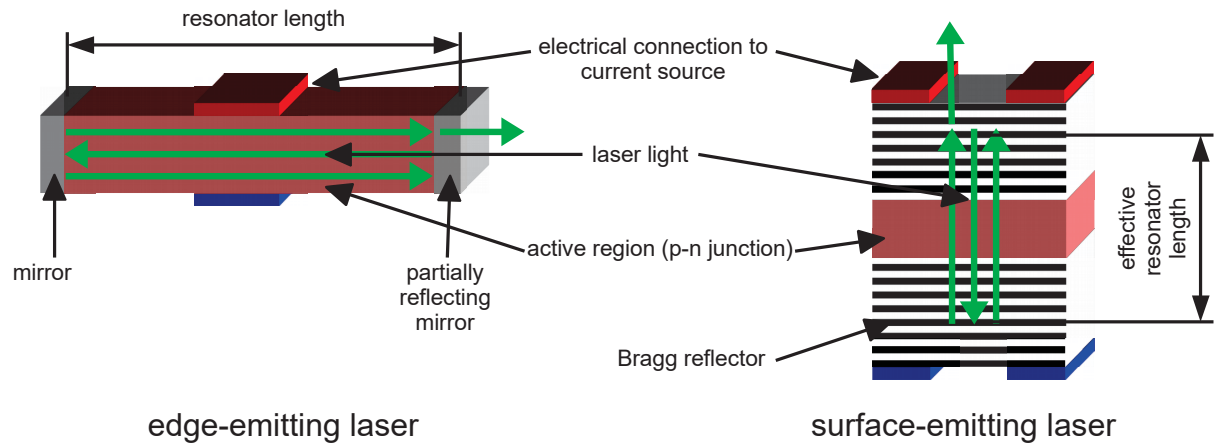

Figure 2.1: General setup of semiconductor lasers: Edge-emitting (left) and surface-emitting (right).

the mirror elements (with reflectivities r_1 and r_2) and is amplified (by gain factor g) due to the externally provided driving current. Considering the electrical field of the light (described by the amplitude A and the laser emission frequency $\omega = 2\pi f$) within the cavity at one end at a given time t

$$E(0,t) = A\mathrm{e}^{\mathrm{j}\omega t} \tag{2.1}$$

and taking into account the electrical field after one round-trip in the cavity

$$E(2L,t) = Ar_1r_2\mathrm{e}^{2L(g-\alpha)}\mathrm{e}^{\mathrm{j}(\omega t-2\beta L)} \tag{2.2}$$

leads to the two lasing conditions: First, the gain of the cavity has to be higher than the loss of the light within the cavity

$$r_1r_2\mathrm{e}^{2L(g-\alpha)} \geq 1\,. \tag{2.3}$$

This means, a threshold gain

$$g_{\mathrm{th}} = \alpha + \frac{1}{2L}\ln\frac{1}{r_1r_2} \tag{2.4}$$

has to be realized. Additionally, an integer number of cycles must fit into the cavity forming the modes

$$\mathrm{e}^{-\mathrm{j}2\beta L} = 1\,, \tag{2.5}$$

which can be rewritten using the emitting wavelength λ

$$\beta = \frac{2\pi n}{\lambda} \tag{2.6}$$

as

$$\mathrm{e}^{-\mathrm{j}\frac{4\pi nL}{\lambda}} = 1\,. \tag{2.7}$$

The frequency-dependency of the gain $g(\lambda)$ superimposes with the modes created by the aforementioned phase condition and leads a dominant mode and weaker side-modes.

One key property of lasers is the side-mode suppression ratio (SMSR) which is defined as the quotient between the dominating mode and the strongest side-mode. The wavelength of the dominant mode may change with time when environmental conditions vary e.g. due to the temperature dependency of the material and of the cavity. This behavior is known as mode-hopping. Side-modes and mode-hopping are unwanted especially for WDM systems. Introducing a Bragg reflector into the cavity efficiently suppresses the side-modes (SMSR$>$20 dB).

This kind of lasers is known as distributed feedback lasers (DFB) and is quite popular for optical communication because of comparably narrow linewidth ($< 10\ \mathrm{MHz}$), high power (up to hundreds of mW), single-mode operation and low cost. Its structure is quite similar to the DBR laser shown in Figure 2.1 on the right side where the reflector is outside the cavity. Lasers with external cavity (ECL) are more expensive but provide kilohertz linewidths and wide tunability. These sources can be interesting in WDM scenarios and for optical heterodyning because of the superior phase noise behavior.

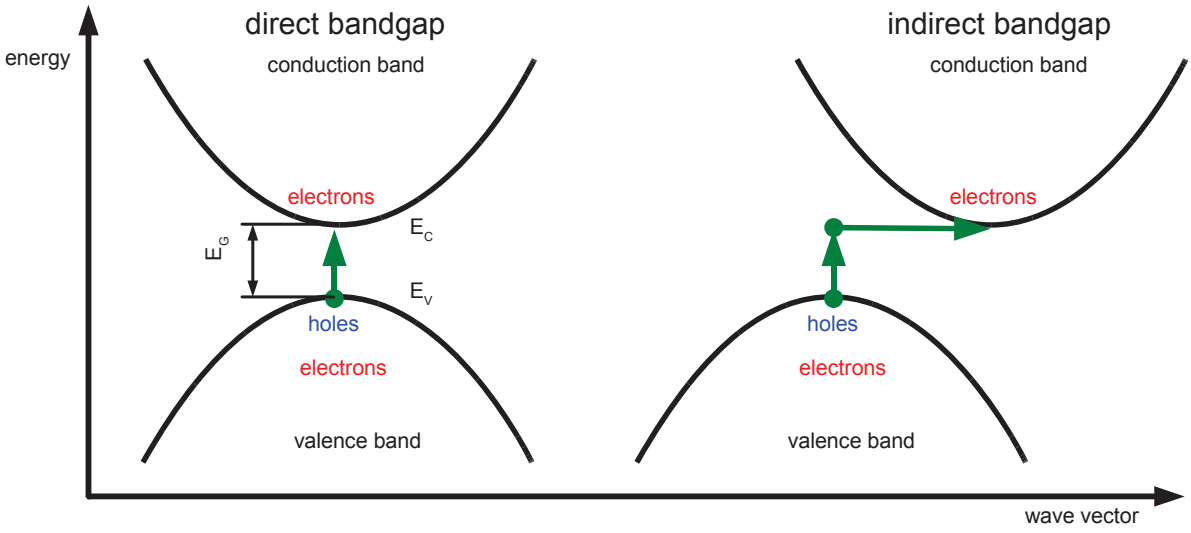

Figure 2.2: Direct (left) vs. indirect bandgap (right).

Often, III-V materials (e.g. GaAs – gallium arsenide, InP – indium phosphide and others such as InGaAs, GaP, AlGaAs, ...) are used to realize the lasers. The main advantage of these semiconductors is their direct bandgap. That means, no additional phonon (wave vector) is needed to excite the electrons from valence band to conduction band (and vice versa) (see Figure 2.2, left side). Hence, an efficient light generation and absorption is ensured. However, integrating lasers and drivers (which are often realized in silicon processes) is very compelling. Therefore, silicon lasers have been in focus of research for many years. Being an indirect bandgap material

(Figure 2.2, right side) makes it extremely hard to use silicon, though. Approaches are growing germanium on silicon (Ge-on-Si laser) to take advantage of the mismatch of the lattice constants of both materials to create a pseudo-direct bandgap [81, 83].

Another option is to integrate III-V semiconductors with silicon wafers, e.g. growing III-V semiconductors on top of a silicon waveguide on a silicon-on-insulator (SOI) wafer [78]. This integration is still not state-of-the-art. Direct wafer bonding at the wafer scale can be carried out with thick relaxed buffers [34]. It is also possible on die scale [144] but not suitable for large scale production. Alternatively, InGaAs can be grown into high aspect ratio trenches [92]. This confines the defects in the bottom of the trench. Additional actions have to be taken to prevent the defects to propagate along the trench. This cost-efficient approach is less flexible and adds some extra optical absorption.

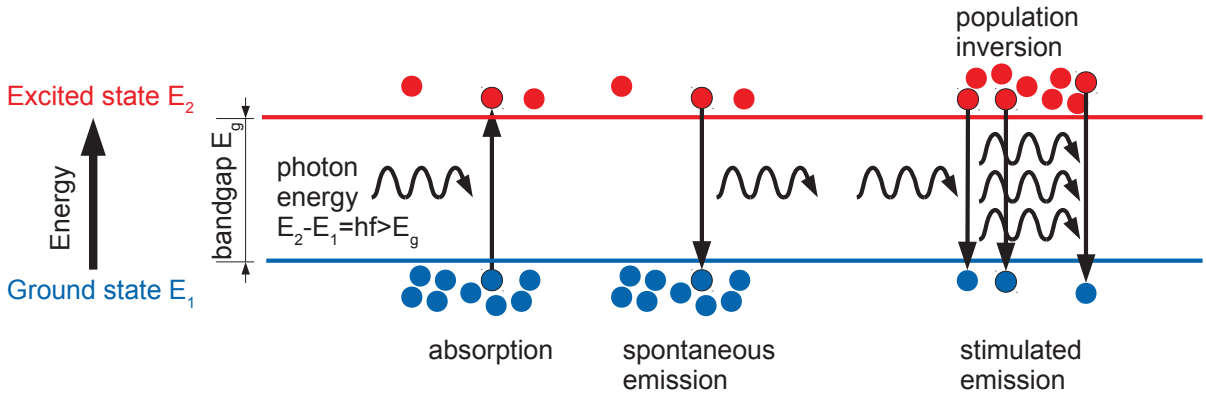

Figure 2.3: Energy diagram for absorption, spontaneous emission and stimulated emission.

The dynamic behavior of a laser can be explained with the optical transition processes taking place in the gain medium: absorption, spontaneous emission and stimulated emission (Figure 2.3). The energy of an absorbed photon excites an electron in the gain medium material from ground state with low energy E_1 to an excited state with higher energy E_2. The counterpart of this process is the spontaneous emission: When dropping back from an excited state to the ground state, an electron releases its energy in form of a photon. The energy difference and therefore the frequency f of the photon has to be bigger or equal than the bandgap E_g of the material

$$E_2 - E_1 = hf \geq E_g \,, \tag{2.8}$$

where h is the Planck constant. When electrical pumping creates a situation where much more electrons are in the excited state than in the ground state (population inversion), the third process – stimulated emission – occurs. An incoming photon triggers excited electrons to fall back to ground state and at the same time release photons that are identical in frequency and phase with the incoming photon. This process leads to coherent light which is characteristic for a laser.

Every laser has a lasing threshold – the laser current where sufficient electrons in the gain medium are in the excited state so that stimulated emission dominates. This current and the laser diode voltage determine the minimum power consumed by the laser. Therefore, low threshold currents and voltages are appreciated for the sake of energy efficiency (see section 3.1.3).

The rate equation model describes the dynamic interaction between excited electrons and photons using differential equations. For the general understanding aimed at in this chapter, the detailed mathematical description available in literature [162] is not needed. However, two quantities are linked with each other: electron density and photon density. The electron desity is increased by the driving current that excites electrons and is lowered by the spontaneous decay and stimulated emission of electrons. Finally, the photons generated by these processes increase the photon density. The photons which are coupled out or absorbed decrease it.

Consequently, switching on the driving current builds up a carrier density. When a population inversion is created and lasing starts (i.e. stimulated emission dominates over spontaneous emission), the photon density increases. Often, an overshoot can be observed when the output light increases too much and the electron density drops. Quickly, a steady state with an equilibrium between carrier generation and light emission is reached. Manipulating the laser current affects the optical output power which can be used for (direct) data modulation discussed in the next section. However, variations of the output power also slightly change the laser frequency. This effect known as chirp is classified into adiabatic and transient chirp. While adiabatic chirp makes the center wavelength of the laser follow the envelope of the output signal, transient chirp happens during the fast transitions typical for digital signals. This phase change is seen to be more harmful to the signal integrity because it leads to a spectral broadening, i.e. the output amplitude of the laser $A(t)$ shows a parasitic phase modulation $\Phi(t)$

$$A(t) = A_m(t)\mathrm{e}^{\mathrm{j}\Phi(t)}\,, \tag{2.9}$$

where $A_m(t)$ is the amplitude modulated data. [38, 49, 79, 151]
Assuming Gaussian pulses with the pulse width T_0

$$A_m(t) = A_0\mathrm{e}^{-\frac{1}{2}\left(\frac{t}{T_0}\right)^2}\,, \tag{2.10}$$

a chirp factor c may be introduced describing the parasitic phase modulation caused either by a directly modulated laser or a Mach-Zehnder modulator (see section 2.2)

$$A(t) = A_0\mathrm{e}^{-\frac{1}{2}\left(\frac{t}{T_0}\right)^2}\mathrm{e}^{-\mathrm{j}c\left(\frac{t}{T_0}\right)^2}\,. \tag{2.11}$$

Moreover, carrier density changes lead to random fluctuations in optical power (ΔP). This noise is typically characterized in relation to the nominal optical output power P_0 as relative intensity noise

$$\mathrm{RIN} = \frac{\Delta P}{P_0}\,. \tag{2.12}$$

RIN has a frequency-dependent spectral density that changes with the bias of the laser diode. Increasing the bias current usually lowers the RIN and shifts its peak to higher frequencies. It is worth mentioning that for higher bias currents also the modulation bandwidth is increased.

In conclusion, lasers have to be operated respecting some physical limits. In order to provide population inversion required for stimulated emission, lasers cannot work in thermal equilibrium. An external power source has to be applied (so-called pumping). For semiconductor lasers, a forward-biased p-n junction is used. Theory shows that the required population inversion has to be realized with at least a three-level atomic system (with a two-level system, at maximum the same number of electrons in excited and ground state can be achieved). The band structure in semiconductors is described with a conduction band and a valence band with corresponding Fermi levels. Outside thermal equilibrium, these Fermi levels do not coincide and their separation must exceed the bandgap for population inversion.

2.2 Electro-optical conversion

To transport and process microwave signals in optical domain, they have to be modulated on an optical carrier (i.e. converted from electrical domain to optical domain). By altering the properties of the optical carrier (discussed in the previous chapter), the electrical signal is imprinted in optical domain. Generally, amplitude, phase and polarization of the carrier may be changed.

However, the state of polarization changes during transmission over standard single-mode fiber (see next chapter). A polarization beam splitter and two photodiodes are needed to detect the state of polarization by accessing two orthogonal states of polarization. Moreover, polarization crosstalk leads to changes in the power ratio between the orthogonal states of polarization. Hence, modulating the RF signal on the carrier using the polarization is impractical. That's why only few polarization modulators exist. Polarization is mainly used for multiplexing signals enhancing the available data rate.

Photodiodes can not restore the optical phase of a signal. As a consequence, sophisticated optical heterodyne receivers are needed for phase modulated signals. For digital signals modulated with special dual-parallel Mach-Zehnder modulators in optical baseband (i.e. without RF carrier), this scheme is used because advanced modulation formats (e.g. QPSK) are supported. Anyway, an optical hybrid and a local oscillator laser as well as at least two photodiodes and electronic post-processing are needed to restore the electrical signal at the receiver. For that reason this approach is way too complex for typical microwave photonic systems.

So, amplitude modulation is realized most conveniently for a broad variety of applications. At the modulation stage, different options are available and will be reviewed in the following paragraphs: direct modulation and external modulation.

One important performance parameter for an amplitude modulated signal is its extinction: the ratio between the optical power for maximum transmission $P_{\mathrm{opt,max}}$ and the optical power for minimum transmission $P_{\mathrm{opt,min}}$

$$r_e = \frac{P_{\mathrm{opt,max}}}{P_{\mathrm{opt,min}}} \,. \tag{2.13}$$

For external modulators, the insertion loss, i.e. the dissipated power in the case of maximum transmission inside the device is another relevant criterion

$$L = \frac{P_{\mathrm{in}} - P_{\mathrm{opt,max}}}{P_{\mathrm{in}}} \,. \tag{2.14}$$

It is desirable to drive external modulators and directly modulated lasers with as small as possible RF amplitudes. This relaxes the demands on the electronic driver amplifier and increases the overall energy efficiency of the system. Device dependent parameters such as slope efficiency (for direct modulation), swing voltage (optical ring modulators, electro-absorption modulators) or half-wave voltage V_π (Mach-Zehnder modulator) exist to characterize that feature. Moreover, parasitic phase modulation (chirp) may not only occur for direct modulation as mentioned in section 2.1 but also for external modulators.

At the receiver where the optical signal is converted back to electrical domain, a photodiode is sufficient for amplitude modulated signals. The opto-electrical conversion part of microwave photonic systems will be discussed in detail in chapter 2.4.

2.2.1 Direct modulation

Direct modulation is a simple and cost-effective concept that allows high integration and minimizes the number of elements in the system. Figure 2.4 shows the basic principle. The semiconductor laser is operated with a DC bias current I_0. The electrical RF signal i_{RF} is added. Adjusting the bias I_0 and amplitude of i_{RF} has a huge influence on the system performance: The resulting laser current $I_0 + i_{\mathrm{RF}}$ should stay above its threshold I_{th} in order to prevent the source to stop and restart lasing which leads to inacceptable signal impairments. On the other hand, a resulting laser current above the maximum current rating I_{max} of the laser diode will destroy the light source. Higher amplitudes of i_{RF} will increase the extinction ratio r_e which leads to a better SNR at the receiver. However, the nonlinear distortions of the RF signal increase as well due to the nonlinear characteristic of the laser diode.

The modulation bandwidth of directly modulated semiconductor lasers is fundamentally limited [111]. Electrical parasitics like oxide and diffusion capacitance can be tackled. However, the cavity damping rate increases linearily with the laser power while the resonant frequency is proportional to the square root of the power. Hence, there is a bias power where this relaxation resonance is critically damped, i.e. the modulation bandwidth is limited by that mechanism. Using sophisticated techniques such as injection locking, the bandwidth may be increased beyond this limit [59, 150]. The number of photons in the cavity is increased without increasing the bias power,

that's why the aforementioned correlation between bias power and resonance frequency is broken. Anyway, this requires a second laser and leads to a rather complex setup.

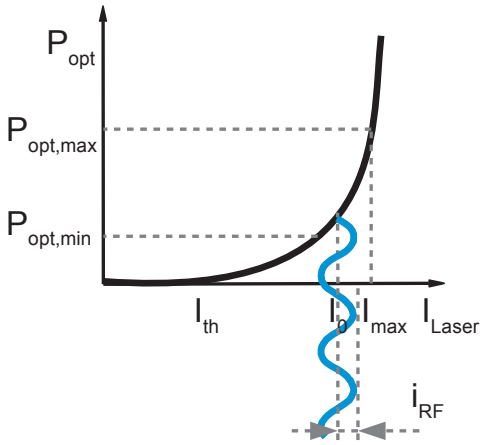

Figure 2.4: direct modulation of laser current

2.2.2 External modulation

External modulation is an option that has several advantages: One laser may be shared among different modulators. Serving as source for different parallel data streams may improve the energy efficiency especially for short distances where low optical powers are sufficient. One laser per data stream (as in direct modulation) may provide higher optical powers than needed due to the laser threshold and decrease the energy efficiency (see section 3.1.3).

Common modulator types are Mach-Zehner interferometer or ring interferometer based. In both models, the driving electrical signal changes the refractive index of the optical waveguide inside the modulator n_{eff} by Δn over the interaction length L. This causes a phase shift Φ that influences the transfer function of the modulator. The driving voltage V_π that causes a phase shift of $\Phi = \pi$ is one key feature. Designing modulators with a small V_π lowers the requirements for the electronic driving circuits and can improve the energy efficiency (see section 3.1.3). The insertion loss as ratio of input power P_{in} and output power P_{out}

$$\mathrm{IL} = 10 \log_{10} \left(\frac{P_{\mathrm{in}}}{P_{\mathrm{out}}} \right) \tag{2.15}$$

tells about the power dissipated in the modulator and should be as low as possible. The polarization dependency of the electro-optical effect, e.g. in $\mathrm{LiNbO_3}$ crystals and the optical waveguides inside the modulator render the insertion loss IL polarization dependent. Hence, a polarization adjustment is needed for efficient operation. The

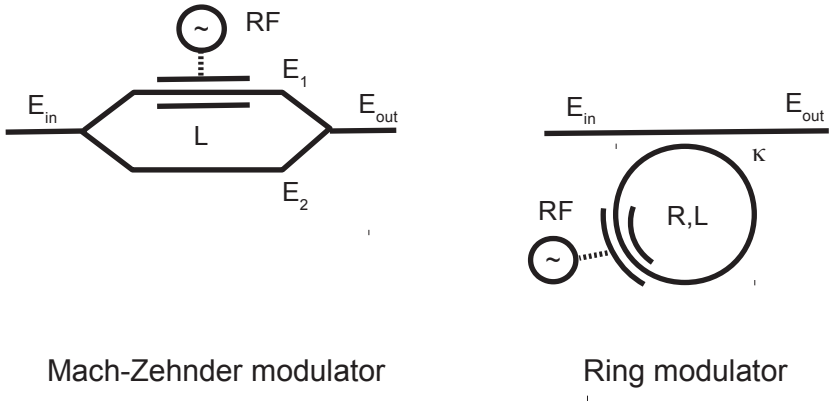

Figure 2.5: Structure of Mach-Zehnder modulator (left) and ring modulator (right).

output amplitude of the electrical field of a Mach-Zehnder modulator is composed of the two arms that can be seen in Figure 2.5 (left)

$$\frac{E_{\text{out}}}{E_{\text{in}}} = E_1 + E_2 = \mathrm{e}^{\mathrm{j}\Phi_0}\left(\mathrm{e}^{\mathrm{j}\Phi} + 1\right), \tag{2.16}$$

where Φ_0 is the common phase shift between input and output due to propagation and

$$\Phi = \frac{2\pi\Delta n L}{\lambda} \tag{2.17}$$

is the phase shift over the interaction length L of arm one because of the signal dependent refractive index modulation Δn at the operating wavelength λ. The resulting power transfer function of the Mach-Zehnder modulator is

$$\frac{P_{\text{out}}}{P_{\text{in}}} = \cos^2\left(\frac{\Phi}{2}\right). \tag{2.18}$$

The transfer function between the output and the input electrical fields of the ring modulator is (Figure 2.5, right)

$$\frac{E_{\text{out}}}{E_{\text{in}}} = \mathrm{e}^{\mathrm{j}(\Phi_0+\Phi+\pi)}\frac{\alpha - \kappa\mathrm{e}^{-\mathrm{j}(\Phi_0+\Phi)}}{1 - \alpha\kappa\mathrm{e}^{\mathrm{j}(\Phi_0+\Phi)}} \tag{2.19}$$

with the attenuation constant α, the complex coupling coefficient κ between ring and waveguide, the phase shift due to the propagation within the ring with radius R

$$\Phi_0 = 4\pi^2 n_{\text{eff}}\frac{R}{\lambda} \tag{2.20}$$

and the phase shift due to the modulation

$$\Phi = \frac{2\pi\Delta n L}{\lambda}. \tag{2.21}$$

The power transfer function is

$$\frac{P_{\text{out}}}{P_{\text{in}}} = \frac{\alpha^2 + |\kappa|^2 - 2\alpha|\kappa|\cos(\Phi_0 + \Phi)}{1 + \alpha^2|\kappa|^2 - 2\alpha|\kappa|\cos(\Phi_0 + \Phi)}\,. \tag{2.22}$$

Changing the attenuation α and the coupling coefficient κ, the slope and the extinction of the transfer function can be tuned.

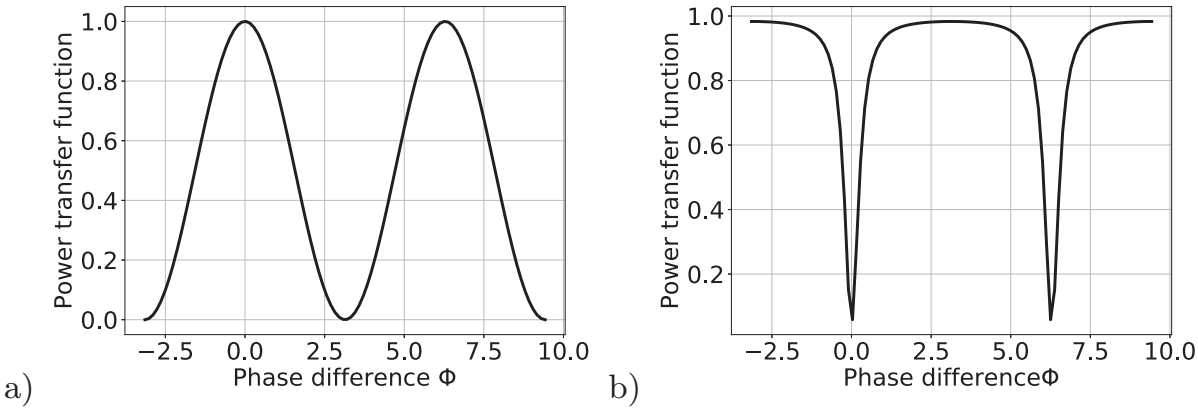

Figure 2.6: Power transfer functions of a) Mach-Zehnder modulator b) ring modulator ($\alpha = 0.85$, $|\kappa| = 0.9$) depending on the optical phase difference Φ caused by the modulating electrical signal.

Figure 2.6 shows transfer functions of an ideal Mach-Zehnder modulator and a ring modulator. The values $\alpha = 0.85$ and $|\kappa| = 0.9$ for the ring modulator are taken from the realization in [15]. It is worth mentioning that a hypothetical lossless ring-modulator would have a constant normalized power transfer function of "1" with discontinuities at phase differences Φ of multiples of 2π. It can be seen in Figure 2.6 that a smaller phase change Φ is sufficient for ring modulators for amplitude modulation. However, the nonlinear distortions introduced by the modulator are lower for the MZM, especially when operated with low modulation indices. This can be valuable especially for OFDM modulated RF signals and other modulation schemes that are vulnerable to nonlinearities.

Modulators integrate well in a silicon photonics scenario ([15] and many more). Advanced modulation formats with higher spectral efficiency are available with certain external modulators (e.g. dual parallel Mach-Zehnder modulator, DPMZM) [156]. However, the insertion loss and additional complexity of the system are a disadvantage. Not only polarization considerations but also additional required bias voltages, temperature drift issues, modulator driver needs (to name some) have to be considered. Thus, there are many applications where direct modulation is still the best choice.

An interesting compromise between external and direct modulation are electro-absorption modulators (EAM) that can be co-integrated with the laser [26, 80]. Electro-absorption modulators change the amount of light being absorbed with the

applied electric field (i.e. RF driving voltage). In conventional bulk semiconductors, the Franz-Keldysh effect is used. More advanced quantum well modulator structures take advantage of the Quantum-confined Stark effect. Advantages of EAMs include low driving voltage, zero-bias operation, low chirp and high available bandwidth. The EAM has a lower polarization dependency compared to Mach-Zehnder modulators. The co-integration with the laser further relaxes this issue.

2.3 Transmission medium

Optical transmission can be in free space or within a guiding medium. The propagation speed is defined by the refractive index $n = \frac{c_0}{c_{\mathrm{medium}}}$, where c_0 is the speed of light in vacuum and c_{medium} is the speed of light in the medium. Waveguides consist of a core and a cladding with different refractive indices. The refractive index of the cladding is smaller than the one of the core permitting total internal reflection. Therefore, an effective refractive index n_{eff} (with n_{eff} in the range between the refractive index of the core and the cladding material) can be introduced for signals propagating in the waveguides. The effective refractive index accounts for the fact that portions of the field are propagating not only in the core but also in the cladding. As this mode field distribution is wavelength dependent, also n_{eff} varies with wavelength.

The refractive index is a function of frequency ω and power P. The frequency dependency leads to (linear) dispersive effects while the power dependency causes nonlinearities. Being much smaller than the linear frequency dependent contributions, the nonlinear refractive index $n'(\omega)$ is modeled conveniently in a scalar approach

$$n'(\omega) = n(\omega) + n_2 P\,. \tag{2.23}$$

With the nonlinear index n_2, the nonlinear parameter γ can be calculated

$$\gamma = \frac{\omega n_2}{A_{\mathrm{eff}} c_0} \tag{2.24}$$

which besides the material also takes into account the effective area A_{eff} of the waveguide (i.e. the waveguide geometry). Thus, the nonlinear parameter is a good measure for the nonlinearity e.g. caused by fibers. The light can be seen as electromagnetic wave. As such, the propagation constant $\gamma = \alpha + \mathrm{j}\beta$ in the lossless case ($\alpha = 0$)

$$\gamma = \mathrm{j}n\frac{2\pi}{\lambda} \tag{2.25}$$

depends on the refractive index of the medium n (n_{eff} for waveguides) at the wavelength of operation λ. The envelope of the electromagnetic wave (i.e. the information) travels with the group velocity v_g. The group refractive index (in the linear case)

$$N = \frac{c_0}{v_g} = n(\omega) + \omega\frac{\mathrm{d}n(\omega)}{\mathrm{d}\omega} \tag{2.26}$$

can be determined from the frequency behavior of the refractive index $n(\omega)$.

For a lot of applications, taking into account only the linear effects described in the first part of this chapter is sufficient to represent the transmission behavior. However, with higher powers and more channels, nonlinear effects have to be modeled as well.

2.3.1 Linear effects

Different linear effects should be regarded for optical transmission. First, the signal is attenuated. In the linear case with no power dependency, this can be described simply by lowering the signal amplitude by the cumulative loss before reception. Second, the signal can be distorted due to different propagation velocities – the so-called dispersive effects. Modal dispersion, chromatic dispersion and polarization mode dispersion can be distinguished.

When the optical waveguide supports more than one mode, modal dispersion is the dominating linear effect. The different spatial field distributions of the different modes lead to specific effective indices n_{eff} for each mode. Different effective propagation velocities of the modes in the medium can be observed. The power of the incident signal is distributed over the different modes that transport the signal over the waveguide. Due to the different propagation velocities, at the output of the waveguide, the input signal is spread over time. That results in pulse broadening leading to inter-symbol interference which limits the maximum data rate for a given transmission length. One way to lower modal dispersion is a careful design of the waveguide (e.g. graded-index fibers) that adjusts the propagation constants as shown in Figure 2.7.

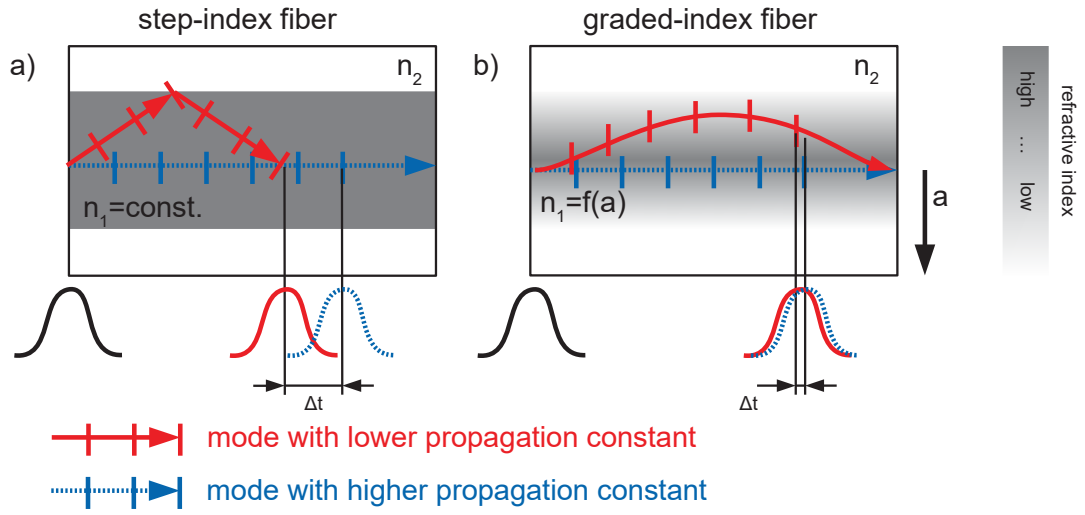

Figure 2.7: Modal dispersion for a) step-index fiber, b) graded-index fiber.

Often, the modal dispersion is avoided by using waveguides that support only one mode. In that case, other dispersive effects become prominent – chromatic dispersion and polarization mode dispersion. Chromatic dispersion, as illustrated in Figure 2.8,

incorporates two frequency-dependent effects: The refractive index of the waveguide (i.e. material dispersion) as well as the power distribution (waveguide dispersion) of the mode field distribution change with frequency. Near the cut-off frequency, the field reaches far into the cladding which has a lower refractive index than the core of the waveguide. With increasing frequency, the field is concentrated more and more in the core resulting in a higher effective refractive index and therefore a lower propagation velocity. While it is difficult to alter the material properties, the waveguide design can be used to engineer specific dispersive behavior. For fibers, this is used to provide dispersion compensating fibers with inverse dispersion compared to standard fibers in order to compensate the chromatic dispersion in a link.

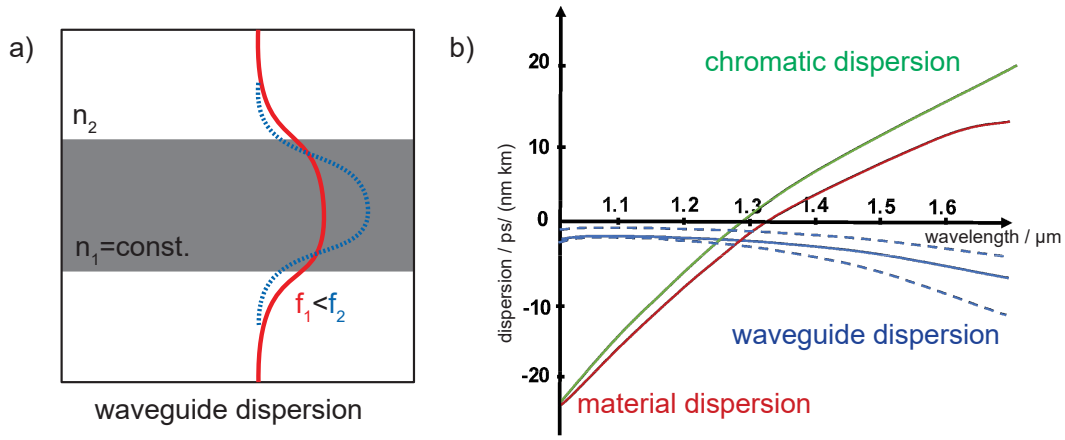

Figure 2.8: a) mechanism of waveguide dispersion: mode field distributions for high and low frequencies, b) chromatic dispersion with waveguide dispersion and material dispersion contributions.

The signal (carrier frequency ω_0) propagating on the optical waveguide (mode field $F(x,y)$ and propagation constant β_0) in z-direction is given with its electrical field

$$E(z,t) = A(z,t)F(x,y)\mathrm{e}^{-\mathrm{j}(\beta_0 z - \omega_0 t)} \tag{2.27}$$

being a solution of the Helmholtz equation

$$\Delta E = \left(\frac{n_{\mathrm{eff}}}{c_0}\right)^2 \frac{\mathrm{d}^2 E}{\mathrm{d}t^2}\,. \tag{2.28}$$

This equation can be solved by inserting the electrical field (2.27). However, when the bandwidth of the modulated signal $A(z,t)$ is much smaller than the carrier frequency, the following simplifications can be applied

$$\frac{\mathrm{d}^2 A(z,t)}{\mathrm{d}z^2} \ll -2\mathrm{j}\beta_0 \frac{\mathrm{d}A(z,t)}{\mathrm{d}z} + \beta_0^2 A(z,t) \tag{2.29}$$

$$\frac{\mathrm{d}A(z,t)}{\mathrm{d}t^2} + 2\mathrm{j}\omega_0 \frac{\mathrm{d}A(z,t)}{\mathrm{d}t} \ll \omega_0^2 A(z,t) \tag{2.30}$$

yielding

$$-2\mathrm{j}\beta_0 \frac{\mathrm{d}A(z,t)}{\mathrm{d}t} + \beta_0^2 A(z,t) = \left(\frac{n_{\mathrm{eff}}\omega_0}{c}\right)^2 A(z,t)\,. \tag{2.31}$$

This means, only the envelope of the field $A(z,t)$ is analyzed over distance in the differential equation. This lowers the computation effort dramatically. The frequency-dependent propagation constant

$$\beta(\omega) = \frac{n_{\mathrm{eff}}(\omega)\omega_0}{c} \tag{2.32}$$

is applied to the Fourier-transform of (2.31). A further simplified frequency-domain differential equation is the result

$$0 = \frac{\mathrm{d}A(z,\omega)}{\mathrm{d}z} + \left(\beta(\omega) - \beta_0\right) A(z,\omega)\,. \tag{2.33}$$

Developing the propagation constant $\beta(\omega)$ into a Taylor series ($\omega' = \omega - \omega_0$)

$$\beta(\omega') = \beta_0 + \frac{\mathrm{d}\beta(\omega')}{\mathrm{d}\omega'}\omega' + \frac{\mathrm{d}^2\beta(\omega')}{2\mathrm{d}\omega'^2}\omega'^2 + \cdots \tag{2.34}$$

helps separating the group delay $\beta_1 = \frac{\mathrm{d}\beta(\omega')}{\mathrm{d}\omega'}$ from dispersion $\beta_2 = \frac{\mathrm{d}^2\beta(\omega')}{2\mathrm{d}\omega'^2}$ and higher order dispersion ($\beta_3, \ldots$) impact. Neglecting higher order dispersion and working in a retarded time regime ($t' = t - \beta_1 z$) leads to the differential equation in time domain

$$0 = \frac{\mathrm{d}A(z,t')}{\mathrm{d}t'} - \mathrm{j}\frac{\beta_2}{2}\frac{\mathrm{d}A(z,t')}{\mathrm{d}t'^2}\,. \tag{2.35}$$

Gaussian pulses $A(t') = A_0 \mathrm{e}^{-\frac{1}{2}\left(\frac{t'}{T_0}\right)^2}$ are often used for theoretical derivations because in differential equations, they maintain their nature. This way, equation (2.35) can be solved analytically and a simple dependency of the pulse width from the transmission length can be determined

$$T(z) = T_0\sqrt{1 + \left(\frac{\beta_2 z}{T_0^2}\right)^2}\,. \tag{2.36}$$

It is worth mentioning that for other pulse shapes (e.g. the widely used raised cosine), equation (2.35) has to be solved numerically. The pulse broadening is critical because inter-symbol interference lowers the link perfomance. Accordingly, for a pulse broadening to $\sqrt{2}T_0$, the so-called dispersion length L_{D} is defined

$$L_{\mathrm{D}} = \frac{T_0^2}{|\beta_2|}\,. \tag{2.37}$$

The dispersion length may serve as simple rule-of-thumb to determine the approximate distance where chromatic dispersion becomes critical. As mentioned in

chapter 2.2, modulation can introduce chirp. A chirped Gaussian pulse $A(t') = A_0 \mathrm{e}^{-\frac{1}{2}\left(\frac{t'}{T_0}\right)^2} \mathrm{e}^{-\mathrm{j}c\left(\frac{t'}{T_0}\right)^2}$ with chirp factor c leads to a reduced dispersion distance.

$$L_{\mathrm{D,chirp}} = \frac{L_D}{\sqrt{(1+c^2)}} \,. \tag{2.38}$$

However, chirped signals can be used for pulse compression at short lengths when $c\beta_2 < 1$. The minimum pulse length can be observed at

$$L_{\min} = -\frac{cT_0^2}{\beta_2(1+c^2)} \,. \tag{2.39}$$

Single-mode waveguides may actually have two polarization modes. Ideally, due to the waveguide symmetry, these modes have the same propagation constants. Practically, small changes – e.g. a small ellipticity of a fiber core – lead to different propagation constants for different polarizations (polarization mode dispersion PMD). In order to include polarization dependent effects, the calculation of the pulse propagation has to be performed independently for orthogonal polarizations with different propagation constants. Between the polarization with the smallest velocity (slow axis) and the one with the highest propagation speed (fast axis), the differential group delay

$$\mathrm{DGD} = |\tau_{\mathrm{fast}} - \tau_{\mathrm{slow}}| \approx |n_{\mathrm{eff,fast}} - n_{\mathrm{eff,slow}}| \frac{L}{c_0} \tag{2.40}$$

is defined as the difference between the propagation times τ_{fast} and τ_{slow}. Normalizing the mean value of the DGD to the length L leads to the PMD coefficient

$$D_{\mathrm{PMD}} = \frac{\langle DGD \rangle}{\sqrt{L}} \,. \tag{2.41}$$

Higher order PMD [64] is the derivative of the differential group delay with frequency and will not be taken into account here.

2.3.2 Nonlinear effects

Nonlinearity in optical waveguides can be categorized in stimulated scattering effects and optical Kerr effect based phenomena. The stimulated scattering occurs only above a threshold power. Therefore, it can be easily avoided. Stimulated Raman scattering (SRS) and stimulated Brillouin scattering (SBS) may also be used for optical amplification. Although there ares some applications in microwave photonics for SRS [60, 141] and SBS [84, 124, 163], it will not be dealt with these effects here.

From the optical Kerr effects, self phase modulation (SPM) and cross phase modulation (XPM) are the most important ones for microwave photonics systems due to the strong carriers involved. Four wave mixing (FWM) produces additional tones that lower the efficiency but can be filtered out in typical scenarios.

To describe the nonlinear effects with the nonlinear parameter model introduced in equation (2.24), the differential equation (2.35) has to be extended by a nonlinear

term. Because of the power dependent refractive index, it is important to also include the attenuation α in the differential equation

$$0 = \mathrm{j}\frac{\mathrm{d}A(z,t')}{\mathrm{d}z} + \mathrm{j}\frac{\alpha}{2}A(z,t') - \frac{\beta_2}{2}\frac{\mathrm{d}^2A(z,t')}{\mathrm{d}t'^2} + \gamma|A(z,t')|^2A(z,t)\,. \tag{2.42}$$

Introducing an effective length L_{eff} that produces the same nonlinearity as the original length L, but without attenuation α,

$$P_0L_{\mathrm{eff}} = \int_0^L P_0\mathrm{e}^{-\alpha z}\mathrm{d}z \;\rightarrow\; L_{\mathrm{eff}} = \frac{1-\mathrm{e}^{-\alpha L}}{\alpha} \tag{2.43}$$

helps to simplify the calculations. For Gaussian pulses, a nonlinear length can be determined using (2.42) in analogy to the dispersion length

$$L_{\mathrm{NL}} = \frac{1}{\gamma P_0} \tag{2.44}$$

where the pulse width is broadened by the factor of $\sqrt{2}$ due to its peak power P_0.

Using the nonlinear length and the dispersion length, the appropriate model for the waveguide with length L can be chosen:

- $L \ll L_{\mathrm{D}}$ and $L \ll L_{\mathrm{NL}}$: neglect both effects (transparent waveguide),
- $L_{\mathrm{NL}} \gg L_{\mathrm{D}}$: neglect nonlinearities (linear dispersive waveguide),
- $L_{\mathrm{D}} \gg L_{\mathrm{NL}}$: neglect dispersion (nonlinear waveguide),
- $L_{\mathrm{D}} \approx L_{\mathrm{NL}}$: analyze interaction between nonlinearities and dispersion.

Depending on the case, equation (2.42) can be simplified by neglecting linear or nonlinear terms. An example where all terms are needed to describe the interaction between nonlinearities and chromatic dispersion is soliton propagation. However, this effect is usually not applied to microwave photonic applications.

Nonlinear effects essential for microwave photonics are self-phase modulation and cross-phase modulation. The power-induced change of the refractive index of the fiber (see equation (2.23)) leads to a nonlinear phase shift $\Phi_{\mathrm{NL}} = -\gamma L_{\mathrm{eff}}P_0$ that modulates the phase of the signal's envelope

$$A(L_{\mathrm{eff}},t') = A(0,t')\mathrm{e}^{\mathrm{j}\Phi_{\mathrm{NL}}}\,. \tag{2.45}$$

It is worth mentioning that this phase shift can also be interpreted as chirp. XPM extends the concept in a way that all available WDM channels $(1\ldots k\ldots M)$ contribute to the phase shift of channel k

$$\Phi_{\mathrm{NL,k}} = -\gamma L_{\mathrm{eff}}\left(P_k + 2\sum_{m=1,\,m\neq k}^{M} P_m\right)\,, \tag{2.46}$$

where the SPM contribution $\Phi_{\mathrm{NL,k}} = -\gamma L_{\mathrm{eff}}P_k$ is already included.

2.4 Opto-electrical conversion

Photodiodes are used to convert optical signals to electrical domain. The inner photoelectric effect within a p-n junction of a diode is used to generate an electron (more specifically, an electron-hole pair) from incident photons with higher energy than the bandgap between the ground level and the excited level of the material's electrons. The material of the semiconductor determines the wavelength range where the photodiode may operate (as for the laser sources in chapter 2.1). Silicon, for example, can be used up to wavelengths of around 1 $\mu\mathrm{m}$ while Germanium diodes can be used to detect light with a wavelength up to 1.7 $\mu\mathrm{m}$. The quantum efficiency

$$\eta = \frac{n_{\mathrm{electrons}}}{n_{\mathrm{photons}}} \tag{2.47}$$

expresses the probability that one incident photon generates an electron. It can be calculated by measuring the photocurrent

$$I_p = \frac{q n_{\mathrm{electrons}}}{\Delta t} \tag{2.48}$$

(number of electrons with charge q per time) and the optical power

$$P_{\mathrm{opt}} = \frac{h f n_{\mathrm{photons}}}{\Delta t} \tag{2.49}$$

(number of photons with power hf per time). Summarizing, optical power (photon energy per time) causes an electrical current (electrons per time). Accordingly, the photodiode is a square-law device where the photocurrent is proportional to the incident optical power ($I_p \sim P_{\mathrm{opt}}$). In optical systems, the responsivity

$$R_0 = \frac{I_p}{P_{\mathrm{opt}}} = \frac{q\eta}{hf} \tag{2.50}$$

is more common to compare photodiodes. It directly yields the photocurrent I_p produced per unit of the incident optical power P_{opt}. The responsivity depends on the device design and can be modeled by taking into account facet reflection r, contact absorption $\mathrm{e}^{-\alpha_c D}$, intrinsic absorption $\mathrm{e}^{-\alpha d}$ and the different energy of one photon at different wavelengths

$$R_0 = (1-r)\mathrm{e}^{-\alpha_c D}\left(1-\mathrm{e}^{-\alpha d}\right)\frac{q\lambda}{hc}\,. \tag{2.51}$$

This means, the responsivity increases with wavelength (because the same optical power is transported by more photons).

The responsivity can be increased by changing the diode design to "pin", i.e. adding an "intrinsic" region between p and n in order to increase the depletion region width which improves the absorption of the incident light and therefore the quantum efficiency, see Figure 2.10 a). Figure 2.9 shows the ideal (i.e. 100% quantum efficiency

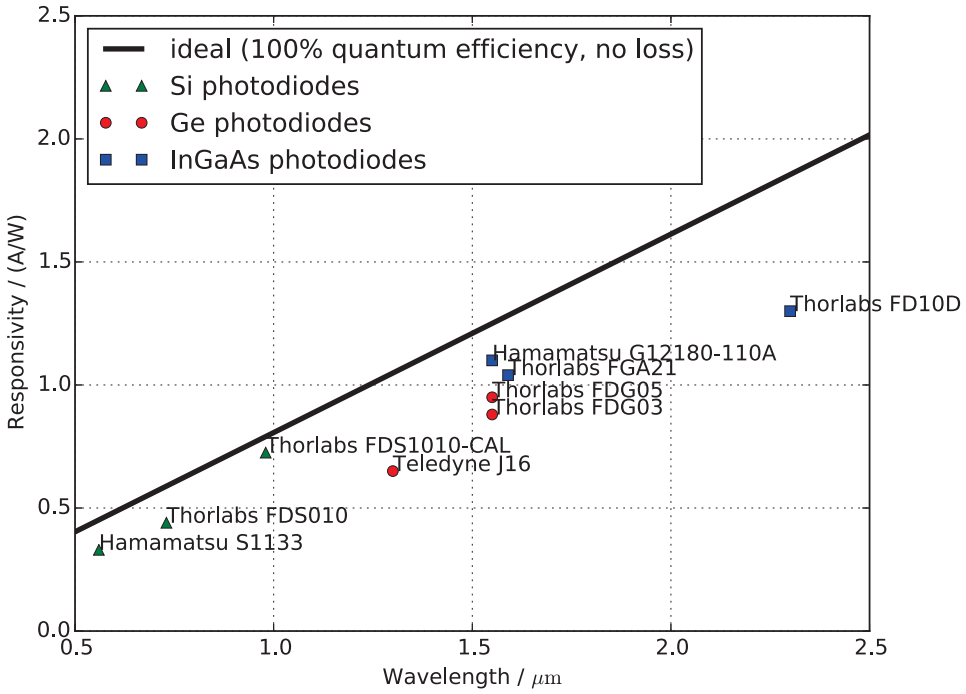

Figure 2.9: Ideal responsivity (black line) and exemplary photodiodes in different semiconductor material systems.

and no loss) wavelength-dependent responsivity and the peak responsivity of exemplary photodiodes realized in silicon, germanium and indium-gallium arsenide (which are the typical materials for photodiodes used in optical communication).

For RoF applications, a fast response (high RF bandwidth) is important. Reverse biasing increases the electric field in the depletion region. This improves the sensitivity as well as the frequency response by lowering the diode capacity: The electric field moves the electrons and holes to the "p" and "n" side before they recombine. However, with increasing reverse bias voltage, also the so-called "dark current" I_d (a.k.a. reverse bias leakage current) increases. This photocurrent is created by randomly generated electrons and holes in the depletion region that are swept by the electrical field. It is one of the noise sources in the photodiode.

Avalance photodiodes (APDs) are more sensitive than pin diodes. Between the "n" and the "i" region of a pin diode, an additional "p" zone is introduced. Consequently, a higher internal electrical field exists in this avalanche region as shown in Figure 2.10 b). The generated carriers are strongly accelerated. Bound electrons are freed after collisions with the accelerated electrons because of their high kinetic energy. These freed electrons are also accelerated unbinding more electrons. So, just a few photons cause an electron avalanche giving the name for this photodiode. APDs require high bias voltages (tens to more than hundred volts). Bias voltage or temperature fluctuations change the gain of the avalanche photodiode transfering noise from the high voltage supply to the APD output signal. The APD gain also amplifies the shot noise typical for all photodiodes as discussed in the next paragraph. That's

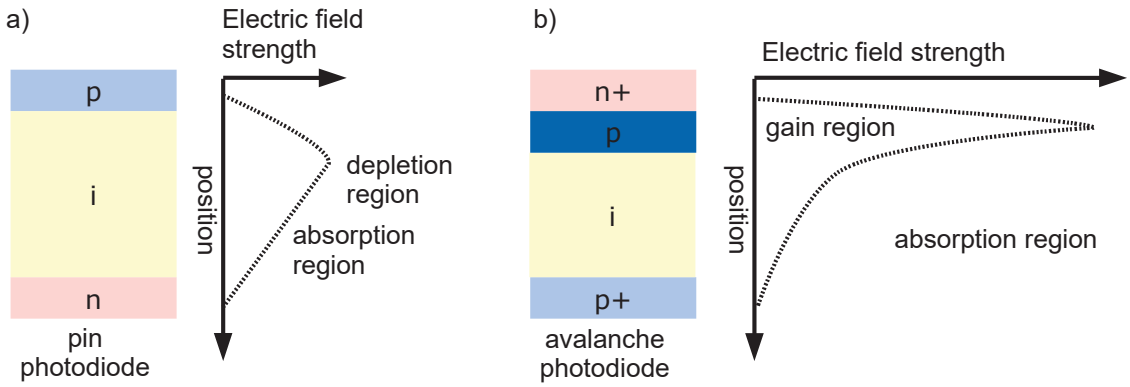

Figure 2.10: a) pin photodiode and b) avalanche photodiode structure and internal electrical field.

why APDs are noisier than other photodiodes. Moreover, the required stabilization of the high voltage supply and the more complicated structure make the avalanche photodiodes more expensive than usual pin diodes. Hence, APDs are only used for extremely weak signals where a high gain is needed.

For all photodiode types, electronic shot noise is caused by the photocurrent I_p flowing through a potential barrier. It depends on the bandwidth B and the electron charge q

$$\left\langle i_{\text{shot}}^2 \right\rangle = 2qI_pB\,. \tag{2.52}$$

Thermal noise induced by random fluctuations of the charge carriers in a resistance occurs even when no voltage is applied to this resistance. It depends on the Boltzmann constant k, the temperature T, the resistance R and the bandwidth B

$$\left\langle i_{\text{thermal}}^2 \right\rangle = \frac{4kTB}{R}\,. \tag{2.53}$$

In APDs, the avalanche multiplication is a random process. McIntyre [89] developed a model to describe the excess noise μ of APDs, today often expressed in the form of

$$\mu = kM + \left(2 - \frac{1}{M}\right)(1-k) \approx 2 + kM\,, \tag{2.54}$$

where M is the multiplication factor (avalanche gain) and $k \leq 1$ is the ratio of the propabilities of hole and electron ionization. Although k can be derived from the carrier ionization coefficients and the distribution of the electrical field in the APD structure, it often has to be measured by fitting the measured excess noise factor and gain to McIntyre's formula. That's why many manufacturers prefer to provide an empirical equation with the characteristic of the photodiode $0.1 < x < 1$

$$\mu = M^{2+x}\,. \tag{2.55}$$

The dark current in the avalanche photodiode I_d has contributions from the unmultiplied surface component $I_{d,s}$ and the multiplied bulk component $I_{d,m}$

$$I_d = I_{d,s} + \mu I_{d,m} \tag{2.56}$$

adding shot noise

$$\left\langle i_{\text{dark}}^2 \right\rangle = 2qI_dB\,. \tag{2.57}$$

Shot noise (and dark current as well as APD excess noise which are modifications of shot noise) has a Poisson distribution that can be approximated (for large numbers) as a Gaussian distribution. Thermal noise is also white and Gaussian.

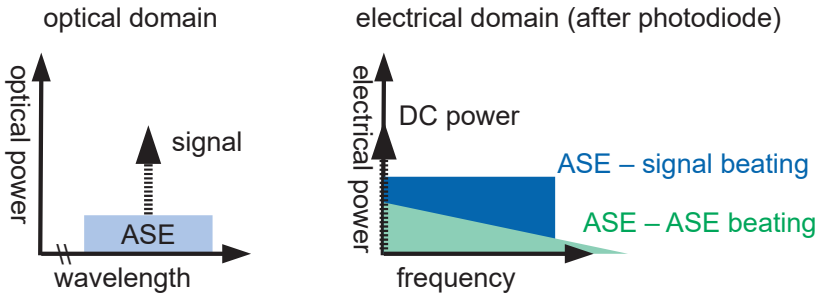

Figure 2.11: Change of noise statistics due to electro-optical conversion by the photodiode.

However, for noise originating in optical domain, the noise statistics change due to the square-law detection. For example, band-limited white noise originating from amplified spontaneous emission (e.g. in lasers or optical amplifiers) does not remain white. Beating between noise as well as signal-noise beating occurs, as shown in Figure 2.11. Moreover, noise in optical domain contributes also to the shot noise because it generates a photocurrent. Hence, optical noise should be avoided before the detector in order to ensure high SNR, e.g. by optical filtering.

3 Applications of microwave photonic systems

In order to underline the broad range of applications for microwave photonics, examples from different fields are given in this part. Starting from a few micrometers transmission range on chip level, where chapter 3.1 deals with the modeling and measurement of optical through-silicon vias (TSV) as well as energy-efficiency considerations, the scale is increased to centimeters in the board level chapter 3.2. Here, integrated photonic antennas as well as RF generation by optical means are demonstrated. Finally, on the system level (being the classical domain for microwave photonics), Radio-over-Fiber and Fiber-to-the-Antenna systems along with a scheme for efficiently enhancing optical sensors with a wireless readout are described in chapter 3.3. Figure 3.1 categorizes the applications that will be discussed in this part regarding transmission distance and system complexity.

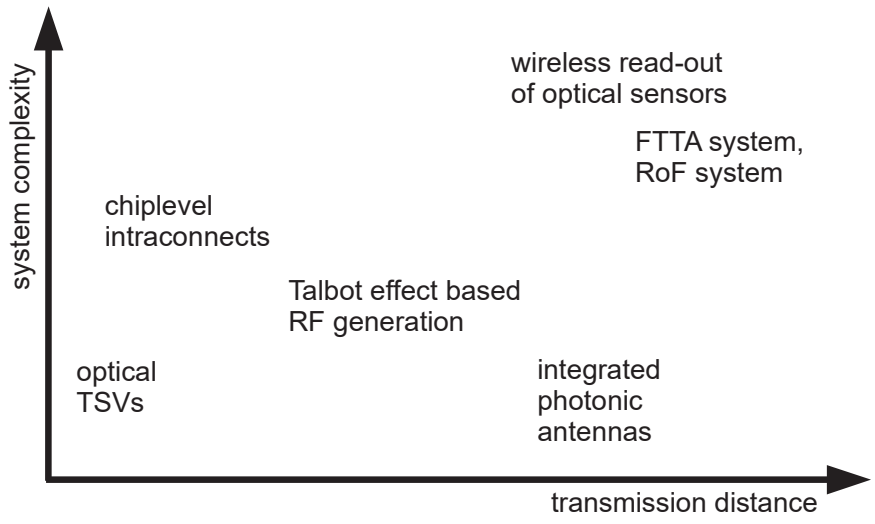

Figure 3.1: Categorization of exemplary applications regarding transmission distance and system complexity

3.1 Chip level applications

Due to the superior properties of optical waveguides for higher bandwidths, microwave photonic systems are reaching out to chip level applications. A typical 3D-integrated system providing a chip-to-chip intraconnect is depicted in Figure 3.2. The electro-optical conversion unit, the transmission medium (optical TSV [18] and waveguide)

and the conversion from optical domain back to electrical domain form an optical link.

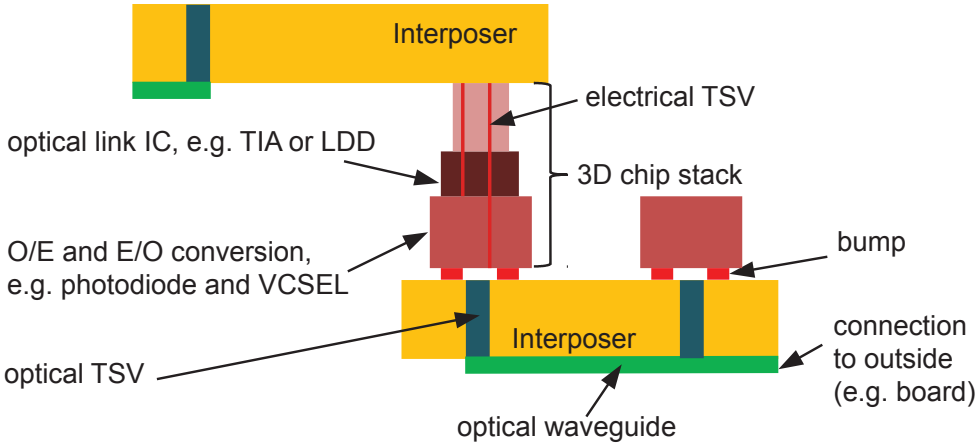

Figure 3.2: Optical 3D-integrated chip-to-chip intraconnect system

It can be seen that electronic RF ICs such as multiplexers (MUX), laser diode drivers (LDD), trans-impedance amplifiers (TIAs) and many more are needed in the transceivers. The ICs may be stacked in a 3D structure and vertically connected by electrical TSVs. Additionally, optical components (e.g. lasers or photodiodes, coupling elements and waveguides) are used in the chip-to-chip link. The central part is the interposer where optical through-silicon vias (TSVs) are used together with optical waveguides to connect different chips.

Section 3.1.1 focuses on the modeling of different types of optical TSVs – the core component for chip-to-chip connectivity. Realized TSVs have been characterized in terms of their system performance (section 3.1.2). For chip-level intraconnects, energy efficiency is one major point which is discussed in chapter 3.1.3.

3.1.1 Optical TSV model

The light transmission through an optical TSV can be classified by the nature of the wave propagation. A waveguide is formed when the cladding has a lower refractive index than the core. In that situation, total internal reflection may occur at the interface between core and cladding. Otherwise, a free-space like behavior can be noticed. In the most simple case – a hole etched in the interposer made of silicon [40] – no waveguiding occurs. However, (partial) reflection still takes place at the interface between air and the bulk silicon from the interposer. Interposers made of other materials will exhibit a similar behavior.

Non-waveguiding TSV

The exciting optical ray may be modeled as Gaussian beam. This beam shape is typical for many possible sources including lasers and fibers. Surface-emitting lasers

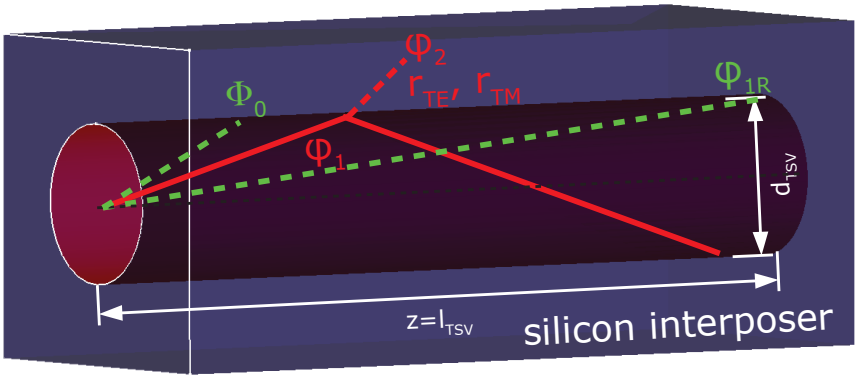

Figure 3.3: Propagation model for non-waveguiding TSV

are a likely choice as light source at the end of a TSV because no additional coupling effort (e.g. grating couplers or mirrors into horizontal waveguides) is needed. These VCSELs mentioned in chapter 2.1 are usually directly modulated. Their initial beam width w_0 is in the micrometer range. Typically, the first optical window ($\lambda_0 = 850\,\mathrm{nm}$) is used. Propagating in air ($n = 1$), the beam widens with transmission distance z

$$w(z) = w_0 \sqrt{1 + \left(\frac{\lambda_0 z}{n \pi w_0^2} \right)^2} \,. \tag{3.1}$$

For typical TSV geometries (the transmission length is tens to hundreds of micrometers, the TSV diameter d_{TSV} is tens of microns), the far-field approximation

$$w(z) = \frac{\lambda_0 z}{n \pi w_0} = \Phi_0 z \tag{3.2}$$

can be applied. Usual VCSEL sources emit with a beam angle in the range of $\Phi_0 = 12°$ [86]. When the beam width $w(z)$ exceeds the TSV diameter, parts of the beam with the incident angle φ_1 are reflected back to the core. The rest is transmitted into the lossy substrate under the angle φ_2 following Snellius' Law

$$\varphi_2 = \arccos \left(\frac{n_{\mathrm{air}}}{n_{\mathrm{sub}}} \cos \varphi_1 \right) \,. \tag{3.3}$$

Due to the high contrast between the refractive indices of air and the silicon substrate ($n_{\mathrm{sub}} = n_{\mathrm{Si}} = 3.66$ at 850 nm), most of the optical power is reflected back to the air core as shown in Figure 3.3. This mechanism should not be mistaken for waveguiding. However, it lowers the losses drastically and enables an efficient transmission over short distances. For TSV lengths l_{TSV} of around a few hundred micrometers, only a few reflections take place. The exact number of reflections can be calculated by finding the largest angle of a possible reflection that is smaller than the exciting beam angle

$$\varphi_{k\mathrm{R}} \leq \Phi_0 \,, \tag{3.4}$$

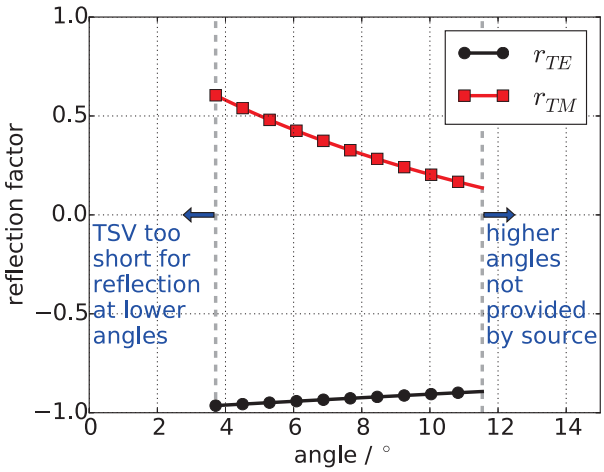

Figure 3.4: TE and TM reflection factors for silicon-air interface in a TSV with $l_{\mathrm{TSV}} = 370\,\mu\mathrm{m}$, $d_{\mathrm{TSV}} = 48\,\mu\mathrm{m}$ excited by a multimode fiber ($A_N = 0.2$) at $\lambda = 850\,\mathrm{nm}$ depending on the incident angle φ_1

where $k \in \mathbf{N}$ and the angle of the respective reflection is determined by the geometry (diameter d_{TSV} and length l_{TSV}) of the TSV

$$\varphi_{k\mathrm{R}} = \arctan\left(\frac{\frac{d_{\mathrm{TSV}}}{2}}{\frac{l_{\mathrm{TSV}}}{2k-1}}\right). \tag{3.5}$$

The TE and TM polarized parts of the optical field have different reflection factors

$$r_{\mathrm{TE}} = \frac{n_{\mathrm{air}}\sin\varphi_1 - n_{\mathrm{sub}}\sin\varphi_2}{n_{\mathrm{air}}\sin\varphi_1 + n_{\mathrm{sub}}\sin\varphi_2} \tag{3.6}$$

$$r_{\mathrm{TM}} = \frac{n_{\mathrm{air}}\sin\varphi_2 - n_{\mathrm{sub}}\sin\varphi_1}{n_{\mathrm{air}}\sin\varphi_2 + n_{\mathrm{sub}}\sin\varphi_1}. \tag{3.7}$$

A smaller incident angle φ_1 increases the reflection factor as depicted in Figure 3.4 and, consequently, reduces the losses. For an angle smaller than the minimum angle

$$\varphi_{\mathrm{min}} = \arctan\frac{\frac{d_{\mathrm{TSV}}}{2}}{l_{\mathrm{TSV}}} \tag{3.8}$$

no reflection at the TSV walls takes place. The numerical aperture A_N of the source defines the maximum angle

$$\varphi_{\mathrm{max}} = \arcsin A_N\,. \tag{3.9}$$

For a worst-case loss calculation, mode equilibrium (i.e. a power distribution among the modes that does not change anymore with length) is assumed. Over the short distances in TSVs, it is more likely that the power is concentrated at lower angles and therefore even lower loss can be achieved. However, an integration over the angular

spectrum of all possible numbers of reflection k provides the total loss in TE and TM polarization of the transmission

$$P_{\mathrm{loss,TE|TM}} = \sum_{k} \int_{\varphi_{k\mathrm{R}}}^{\min(\varphi_{(k+1)\mathrm{R}},\Phi_0)} |r_{\mathrm{TE|TM}}|^{2(k-1)}(1-|r_{\mathrm{TE|TM}}|^2)\mathrm{d}\varphi \qquad (3.10)$$

resulting from the dissipation in the substrate. The cylindrical geometry of the TSV results in an equal contribution of the TE and TM polarized components

$$P_{\mathrm{loss}} = \frac{P_{\mathrm{loss,TE}} + P_{\mathrm{loss,TM}}}{2} \,. \qquad (3.11)$$

Performing the calculation with values for a typical TSV: length $l_{\mathrm{TSV}} = 370\,\mu\mathrm{m}$, diameter $d_{\mathrm{TSV}} = 48\,\mu\mathrm{m}$ and silicon substrate $n_{\mathrm{sub}} = n_{\mathrm{Si}} = 3.66$ at 850 nm yields $P_{\mathrm{loss}} = 2.3\,\mathrm{dB}$ loss. It is worth mentioning that this loss is independent from data rate.

Waveguiding TSV

Wavguiding is based on the principle of total internal reflection. That implies the use of a core material with higher refractive index than the surrounding cladding. Silicon has a comparably high refractive index ($n_{\mathrm{Si}} \approx 3.66$ at 850 nm). That's why it is difficult to find a proper core material. However, the bulk silicon can be shielded using a material with lower refractive index – silicon dioxide ($n_{\mathrm{SiO_2}} \approx 1.45$ at 850 nm) is a good choice here because no extra chemical has to be used during manufacturing. Now, SU-8 ($n_{\mathrm{SU-8}} \approx 1.56$) can be used as core material to form a waveguide. In waveguiding TSVs, only the loss in the material has to be considered. Realizations [69] of low-loss (0.36 $\mathrm{dB/cm}$) rib waveguides have been demonstrated with this material, i.e. loss becomes negligible for short TSVs.

Using numerical simulations, the necessary thickness of the shielding layer preventing the field from being dragged into the silicon could be determined. Already half of the wavelength is sufficient to keep the losses low, i.e. no problems in manufacturing due to the required isolation layer thickness are expected. Figure 3.5 shows such a waveguiding TSV.

With SU-8 as core material ($n_c = 1.56$) and silicon dioxide as cladding ($n_{cl} = 1.45$), the numerical aperture is

$$A_N = \sqrt{n_c^2 - n_{cl}^2} = 0.575 \qquad (3.12)$$

which allows beam angles of up to 35°. Typical VCSELs and other lasers have lower beam angles. Therefore, no additional loss will occur.

The numerical aperture also has an effect on the mode dispersion as described in section 2.3.1, i.e. the time delay between the power (information) transfered using the slowest and the fastest mode $t_{\mathrm{g,max}} - t_{\mathrm{g,min}}$. Mode equilibrium as worst-case scenario is assumed (and will most likely never occur within short-distance TSVs).

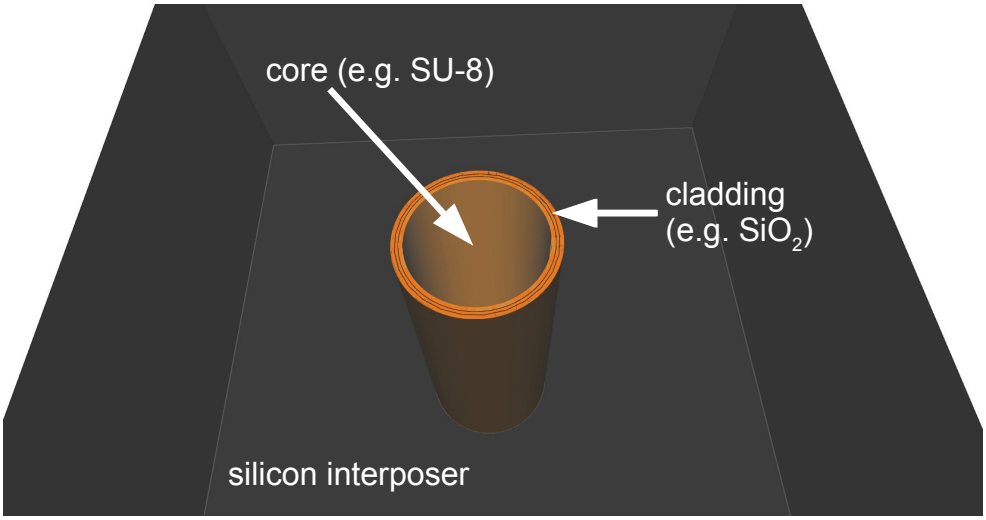

Figure 3.5: Model for waveguiding TSV

The modal dispersion leads to pulse broadening (see chapter 2) and can be quantified for a given length L

$$t_{\mathrm{g,max}} - t_{\mathrm{g,min}} = t_{\mathrm{g,min}} \left(\frac{n_c}{n_{cl}} - 1 \right) . \tag{3.13}$$

where the time for the fastest mode is given by

$$t_{\mathrm{g,min}} \approx \frac{L}{c_0} n_c . \tag{3.14}$$

For a known pulse shape, i.e. rectangular as worst-case (due to the high number of harmonics in the spectrum), the pulse broadening can be found

$$\sigma_{\mathrm{rectangular}} = \frac{t_{\mathrm{g,max}} - t_{\mathrm{g,min}}}{\sqrt{12}} . \tag{3.15}$$

The induced inter-symbol interference limits the available bandwidth

$$f_B = \frac{0.2}{\sigma_{\mathrm{rectangular}}} = \frac{\sqrt{0.48}}{t_{\mathrm{g,max}} - t_{\mathrm{g,min}}} . \tag{3.16}$$

Computing the worst-case channel bandwidth (mode equilibrium and rectangular pulses) for the discussed waveguide with SU-8 core and silicon dioxide cladding, 1.8 THz are found for 1 mm transmission length. In practical realizations, at least one magnitude more bandwidth is expected due to less interference because of other pulse shapes and a more relaxed mode distribution (the sources have a smaller numerical aperture which is not expected to create the full modal spectrum over the short transmission distance). WDM schemes will further increase the total bandwidth of the TSV.

3.1.2 Optical TSV characterization

TSVs with the geometry described before have been produced [67, 99] using an optimized deep reactive ion etching process (DRIE). Non-waveguiding TSVs with air in the center as well as waveguiding TSVs with SU-8 as core have been realized.

The TSVs were characterized in a system setup representing a realistic scenario: VCSELs and photodiodes working at 850 nm wavelength [86] are connected with the TSV. Having a slightly lower bandwidth than the photodiode, the VCSEL transmitter is assumed to be the bandwidth bottleneck (20 GHz). In the test scenario, the optical transmitter and receiver are not directly connected with the TSV. Instead, glass fibers are used to probe the TSVs using micropositioners which causes some coupling loss. For the multi-mode OM3 50/125 $\mu\mathrm{m}$ fiber used with a numerical aperture $A_N = 0.2$, modeling (see equations (3.12), (3.13) and (3.16)) predicts a bandwidth of around 30 GHz for a transmission distance of 0.5 m. That means, the influence of the short fiber pigtails in terms of modal dispersion is much stronger than the one of the TSVs. However, it is expected that the MMF fiber pigtails will not degrade the transmission for the bandwidth used in the experiment. Figure 3.6 depicts the setup. Details of the coupling between the fibers (which can be aligned with x-y-z stages) and the TSV inside the silicon interposer are shown in Figure 3.7.

When comparing different link configurations driven by the same transmitter / receiver pair, the analysis of bit error rate (BER) vs. received optical power (ROP) is a good measure. The transmitter / receiver performance itself (e.g. modulation grade etc.) as well as static insertion loss are not taken into account with this method. Consequently, only the link influence is characterized using this approach which is the aim here. In future systems that are higher integrated, other transmitters and receivers would be used. The different optical powers are set by the optical attenuator in the setup.

The reference is determined by a back-to-back measurement connecting the photodiode directly to the laser (without TSV). With the available transmitter and receiver, a data rate of 18 $\mathrm{Gbit/s}$ could be chosen (error floor 10^{-11}). Adding different types

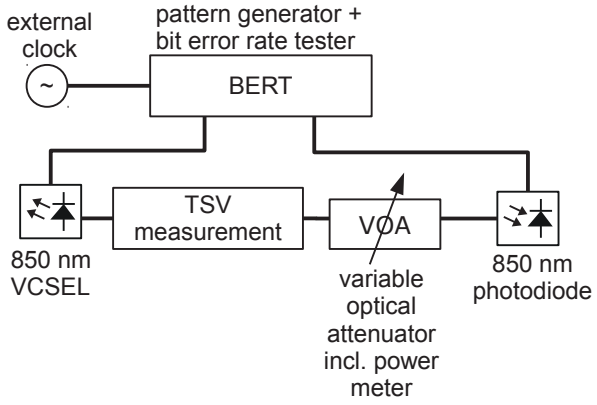

Figure 3.6: Setup for TSV system characterization

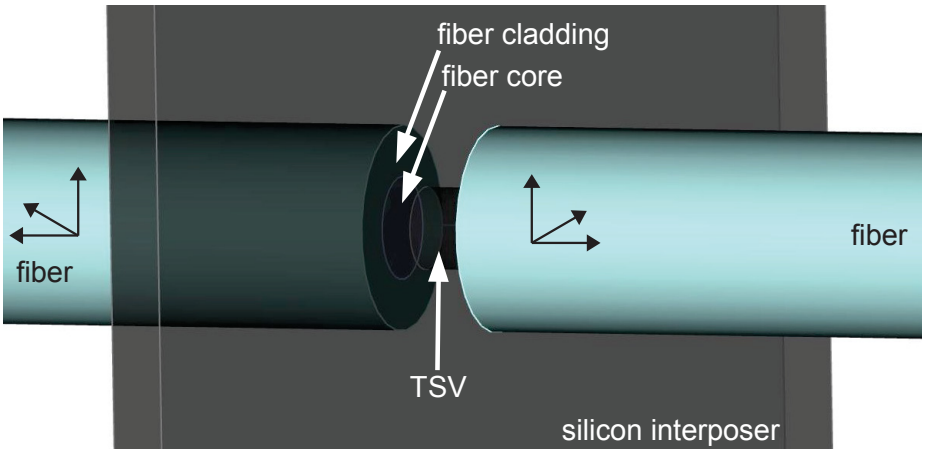

Figure 3.7: Details of the coupling between fibers and TSV

of TSVs, no penalty due to the air-filled or the polymer-filled TSVs can be observed in Figure 3.8. This indicates that the bandwidth provided by the TSVs is much bigger than needed for the transmission, as predicted.

Effects from the TSVs which are too small to influence the bit error rate could still be visible in the eye diagram. However, the waveforms shown in Figure 3.9 do not exhibit any signs of lowpass or dispersive characteristics.

Apart from the system demonstration, the measurement setup (see Figure 3.6) can also be used to estimate the loss introduced by the TSVs. Two contributions have to be distinguished: the loss in the TSV itself and the coupling loss at the interface to the input and output fibers. For waveguide TSVs, the loss inside the TSV is caused by the waveguiding material. In the non-waveguiding (air-filled) TSV case, the power dissipated in the substrate is the main source of the loss. The coupling loss strongly depends on the ratio between TSV diameter and fiber diameter as well as offset and angle of the fiber-TSV alignment. Figure 3.10 shows microscopic images of a non-waveguiding air-filled TSV (left), a waveguiding TSV with SU-8 core and silicon dioxide cladding (middle) and a waveguiding air-filled TSV with copper cladding (right) under back illumination which will be discussed in the following paragraphs.

For the measured non-waveguiding TSVs, a comparably small portion of the incident power is expected to be lost in the substrate because of the high refractive index of silicon. As discussed in the modeling section, higher contrast leads to higher reflection factors and therefore more power remaining in the TSVs. The loss has been measured at 650 nm for air-filled TSVs with diameters between 20 and 50 $\mu\mathrm{m}$. Before estimating the loss (including attenuation due to the fiber coupling), the setup has been calibrated by connecting the fiber ends face to face without any TSV in between. Loss down to 1.3 dB for a TSV link including coupling could be measured. This is less than the estimated worst case of 2.3 dB implying that the laser power is concentrated at smaller beam angles which leads to higher reflection factors and lower overall loss. For other wavelengths (e.g. 850 nm), the situation is similar.

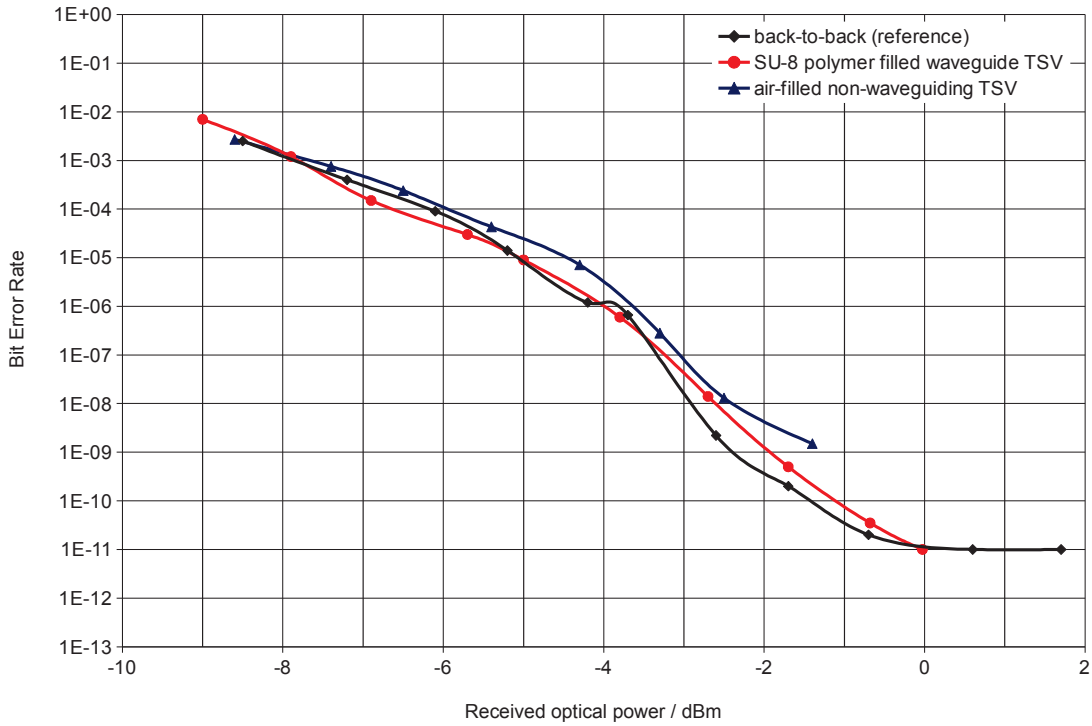

Figure 3.8: Bit error rate vs. received optical power (18 Gbit/s NRZ) for back-to-back measurement, with waveguide TSV (SU-8 polymer core and silicon dioxide cladding) and with non-waveguiding TSV (air-filled)

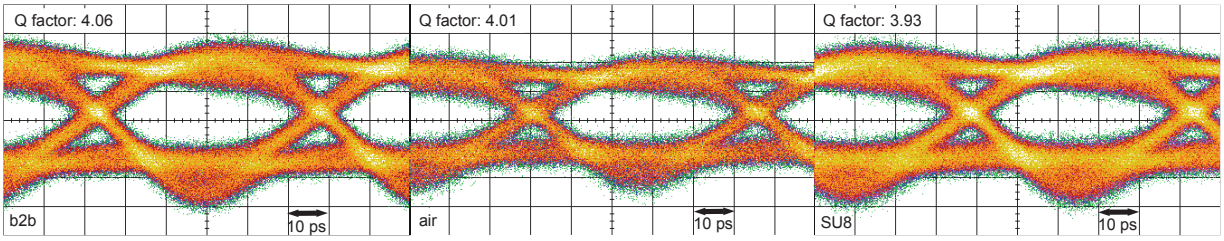

Figure 3.9: Eye diagrams for the TSV measurements at 18 Gbit/s: back-to-back (left), non-waveguiding air-filled TSV (middle), waveguiding TSV with polymer (SU-8) core and silicon dioxide cladding (right)

Figure 3.10: Microscope images of back-illuminated non-waveguiding air-filled TSV (left), waveguiding TSV with SU-8 polymer core and silicon dioxide cladding (middle) and waveguiding air-filled TSV with copper cladding (right)

The waveguiding TSVs with a SU-8 core and a silicon dioxide cladding cause attenuations of around 3 dB. The silicon dioxide cladding has been manufactured with nanometer-scale surface roughness which is one key factor for good waveguiding behavior. However, analyzing the manufactured TSVs shows that air gaps and bubbles (see microscopic image in Figure 3.11) within the TSVs may strongly increase the loss up to 10 dB. The interface between core and cladding is crucial. It is believed that an improved manufacturing process will reduce the TSV attenuation below the level of non-waveguiding TSVs.

Table 3.1: TSV overview

TSV type	**Materials**	**Measured loss**	**Comments**
waveguiding	SU-8 (core), SiO_2 (cladding)	3 dB	improved manufacturing process is expected to dramatically lower loss
waveguiding	air (core), copper (cladding)	3.5 dB	not optimized for optical transmission (small diameters, difficult coupling), simultaneous electrical and optical transmission possible
non-waveguiding	air (core), Si (cladding)	1.3 dB	most simple TSV realization

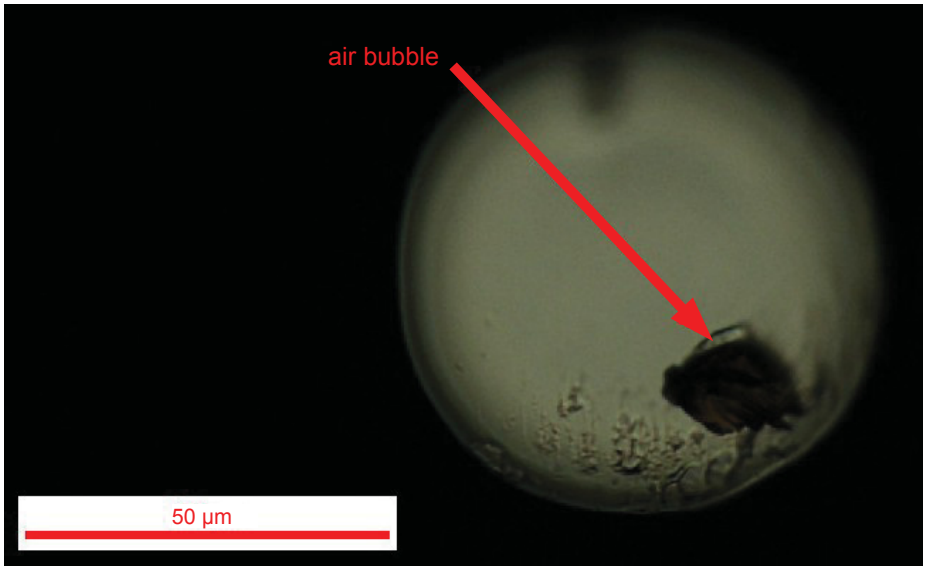

Figure 3.11: Microscope image of back-illuminated waveguide TSV with defect due to bubble inside SU-8 polymer core

A second option for waveguiding TSVs is using air-filled structures with metal (e.g. copper) walls. Metals have refractive indices smaller than 1 (air) in optical domain. Therefore, a waveguiding mechanism can be observed. Available electrical TSVs with 15 μm diameter served as samples to demonstrate the mechanism. It is worth mentioning that these TSVs have not been optimized for use as optical TSVs (e.g. regarding the copper surface roughness). Single-mode fiber had to be used to couple the light into the small waveguiding structure. This makes the fiber alignment difficult due to the resolution of the mechanical positioners available in the lab. Still, for the short distances of a typical TSV (around 370 μm), relatively low attenuations of around 3.5 dB could be reached. This is an encouraging result which may be improved by adapting the manufacturing process to the needs of optical waveguides (e.g. larger diameters for multi-mode excitation, good surface roughness and quality for low loss etc.). Even without any optimization, there could be a dual use of the TSVs for electrical and optical transmission with acceptable performance. All investigated TSVs are compared in Table 3.1.

3.1.3 Energy efficiency in chip-level intraconnects

One of the most important benchmarks influencing technology choices is energy efficiency. Microwave photonic systems traditionally have the reputation of providing high performance at the cost of being power hungry. The background of this verdict is the need for opto-electrical and electro-optical conversion that adds complexity. However, with transmission loss being independent from data rate and increasing only moderately with distance, at a certain length, optical systems will outperform their electrical counterparts.

As mentioned before, long-haul and metro networks as well as data centers already switched to optical communication. In an emerging field – chip-to-chip connectivity – this picture is not as clear yet. Computation power expands exponentially [145] because nowadays, billions of transistors can be integrated on a single chip [158]. In the resulting multi-core CPU era [12], the linear bandwidth growth lags behind the exponential processing capacity increase.

Nano-photonic solutions [145] can be used to form a photonic cross-bar. Multi-layer photonic networks-on-chip (NOC) have been realized [164]. Other systems go for hierarchical approaches [158], hybrid (optical and electrical) concepts [94], on-chip DWDM [33] or even free-space optical links [29, 30].

All the numerous developments have advantages to pure electrical connectivity: Significant increase in bandwidth due to DWDM [145], better latency properties (70% faster than electrical in [164]) and mainly the independence of the achievable data rate from distance [94]. Further improvement comes from introducing 3D packaging and chip stacking. Novel designs [10, 77, 115] allowing shorter transmission length with TSV (see chapters 3.1.1 and 3.1.2) reduce the power consumption, weight, form factor and cost. At the same time, bandwidth and bandwidth density are increased [74, 75].

Yet, for the ultra-short distances it is still unclear at what distance optical transmission becomes more energy efficient. A general comparison is very difficult because of the different use cases and technologies. For a transmission, a transmitter and a receiver is needed. Apart from the physical link between the data source and the data sink, also routing elements may exist. These routers receive, buffer and re-transmit the incoming signal [14]. For one so-called "hop", the signal travels across the electrical cross-bar, the buffer within the router as well as the waveguide between the routers, as shown in Figure 3.12.

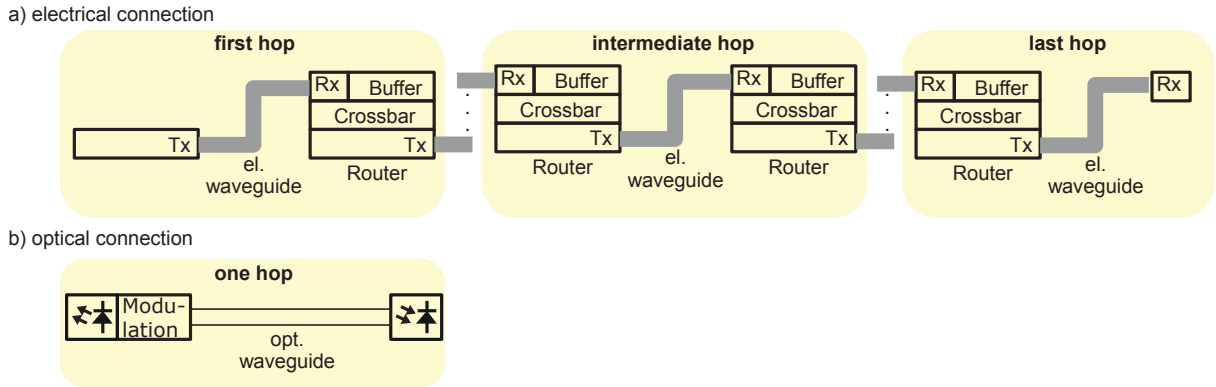

Figure 3.12: block diagram of electrical and optical chip-to-chip link

Consequently, a synthetic chip-to-chip link is defined and analyzed. Performance parameters from known systems will be used to study the consumed energy for a given data rate. Comparing with an electrical system, a link length where optical systems outperform electrical systems in terms of energy efficiency can be determined [142].

A variation of the parameters will be used to point out improvement potential of the components in order to enable optical systems for ultra-short distances.

Electrical vs. optical interconnects

Typically, electrical interconnects transmit data in baseband. Due to the frequency-dependent attenuation of electrical waveguides, increasing bandwidth (i.e. data rate) results in higher attenuation. For transmission in optical domain, the payload data is modulated on an optical carrier. This carrier frequency is 100s of THz – 350 THz for the first, 230 THz for the second and 190 THz for the third optical window – and therefore much higher than the channel bandwidth ($< 1\,\mathrm{THz}$). Hence, optical interconnects are narrowband systems. The attenuation of these systems is bandwidth-independent. Moreover, losses in optical domain are much lower than in electrical domain.

Waveguide losses are characterized with the attenuation constant α_{wg} and increase with distance d. The power lost in the waveguide P_{wg} is the difference between the transmit power P_{Tx} and the received power P_{Rx}

$$P_{\mathrm{wg}} = P_{\mathrm{Tx}} - P_{\mathrm{Rx}} = P_{\mathrm{Tx}}(1 - \mathrm{e}^{-\alpha_{\mathrm{wg}} d}) = P_{\mathrm{Rx}}(\mathrm{e}^{\alpha_{\mathrm{wg}} d} - 1)\,. \tag{3.17}$$

For optical systems, $\alpha_{\mathrm{wg,opt}}$ is independent from bandwidth, as explained above. In contrast, $\alpha_{\mathrm{wg,el}}(R_{\mathrm{data}})$ for electrical systems increases with bandwidth. Typically, the link budget is determined by the receiver sensitivity. That's why the power dissipated in the link P_{link} is given with respect to the power at the receiver

$$P_{\mathrm{link}} = P_{\mathrm{wg}} + P_{\mathrm{Rx}} = P_{\mathrm{Rx}} \mathrm{e}^{\alpha_{\mathrm{wg}} d}\,. \tag{3.18}$$

Changing to logarithmic units, with the waveguide loss in dB

$$L_{\mathrm{wg,dB}} = 10 \alpha_{\mathrm{wg}} d \log_{10} \mathrm{e}\ \mathrm{dB} \tag{3.19}$$

the power consumed in the link can be expressed as

$$P_{\mathrm{link,dBm}} = L_{\mathrm{wg,dB}} + P_{\mathrm{Rx,dBm}}\,. \tag{3.20}$$

If the attenuation of the link is high or the distance is long, the exponential increase in loss leads to high power dissipation in the waveguide. In these cases, it becomes more energy efficient to use multiple hops, as realized in electrical systems [130]. For short hops (or low attenuations), a linear approximation of the loss can be used.

Optical interconnects are typically constructed as single hop [164]. A laser, the modulation unit, the optical waveguide and the photodetector are its elements. This means, the loss in the optical waveguide $L_{\mathrm{wg,opt,dB}}$ can be directly used to calculate the required laser power when the receiver sensitivity $P_{\mathrm{Rx,opt,dBm}}$ is known. Additionally, some static (length-independent) loss, e.g. due to coupling or vias is taken into account.

$$P_{\mathrm{Tx,opt,dBm}} = L_{\mathrm{static,dB}} + L_{\mathrm{wg,opt,dB}} + P_{\mathrm{Rx,opt,dBm}}\,. \tag{3.21}$$

The energy efficiency is determined by the electrical power the laser consumes P_{laser}. It can be calculated for the required optical transmit power $P_{\mathrm{Tx,opt,dBm}}$ from the laser characteristics optical output power vs. laser current and laser current vs. voltage. If the receiver sensitivity is sufficiently low, the power consumed by the laser is independent from the transmitted data rate. Therefore, the energy of the laser consumed per bit decreases with data rate

$$E_{\mathrm{laser}} = P_{\mathrm{laser}}/R_{\mathrm{data}}\,. \tag{3.22}$$

Typically, this representation of the power consumption normalized with the data rate uses the unit $\mathrm{pJ/bit}$. Equivalent and more intuitive is the description directly with power and data rate $\mathrm{mW/(Gbit/s)}$. In the energy-per-bit scale, the power consumption of the driver circuit for the electro-optical modulation increasing with data rate results in a constant E_{mod}.

Contributions to power consumption

The power consumption of the electrical link that depends on data rate but not on length is summarized in E_{static}. In each hop, the buffer (E_{buffer}), the crossbar (E_{crossbar}) as well as the electrical waveguide (E_{hop}) consume power proportional to the data rate. As discussed before, the loss in the waveguide additionally scales with the hop length.

As expressed in equation (3.21), the required laser power is determined by the waveguide loss. It is independent from data rate but increases with link length and its attenuation. Furthermore, the power consumed by the modulation unit is data rate dependent.

Any further processing of the received data (e.g. clock recovery, amplification, digital processing) is not part of the investigated link. Table 3.2 summarizes the contributions to the power consumption in electrical and optical interconnects.

System analysis

In order to analyze the power consumption, values have to be assigned to the different contributions. This is a difficult task because technologies are very heterogeneous and under constant development. For the electrical interconnect, the values are taken from [130]. To account for increasing energy efficiency with improved technologies, the advanced 32 nm technology is chosen: $E_{\mathrm{static}} = 0.35\ \mathrm{mW/(Gbit/s)}$, $E_{\mathrm{crossbar}} = 0.36\ \mathrm{mW/(Gbit/s)}$, $E_{\mathrm{buffer}} = 0.12\ \mathrm{mW/(Gbit/s)}$ and $E_{\mathrm{hop}} = 0.34\ \mathrm{mW/(Gbit/s \cdot mm)}$. The linear length dependency is due to an approximation for short distances of a single hop. The link with length d consists of $n_{\mathrm{hop}} = \lceil \frac{d}{l_{hop}} \rceil$ hops.

$$E_{\mathrm{link}} = \frac{P_{\mathrm{link}}}{R_{\mathrm{data}}} \approx n_{\mathrm{hop}} E_{\mathrm{hop}} \tag{3.23}$$

Table 3.2: Contributions to power consumption of electrical and optical chip-to-chip links

Contribution	**Unit**	**Comment**
E_{static}	mW/(Gbit/s)	data rate dependent, per link
E_{crossbar}	mW/(Gbit/s)	data rate dependent, per hop
E_{buffer}	mW/(Gbit/s)	data rate dependent, per hop
E_{hop}	mW/(Gbit/s · mm)	data rate dependent, length-dependent (linear approximation for short distances), per hop
E_{laser}	mW/(Gbit/s)	decreases with data rate due to static laser power P_{laser}, per link
E_{mod}	mW/(Gbit/s)	data rate dependent, per link

Here, a hop length of $l_{\text{hop}} = 1.6$ mm is used to calculate the power for the electrical system normalized to its data rate R_{data}

$$E_{\text{el}} = E_{\text{static}} + n_{\text{hop}}(E_{\text{crossbar}} + E_{\text{buffer}}) + E_{\text{link}} \,. \tag{3.24}$$

For the optical interconnects, the laser and the modulation stage contribute to the power consumption

$$E_{\text{opt}} = E_{\text{laser}} + E_{\text{mod}} \,. \tag{3.25}$$

Equation (3.21) can be used to calculate the optimal optical transmit power of the laser $P_{\text{Tx,opt,dBm}}$. Not all laser drivers support this power-saving adaptive behavior yet. The characteristics of the optical output power vs. laser current and laser current vs. voltage needed to compute the electrical power consumption of the laser P_{laser} are taken from state-of-the art devices [95, 159].

In equation (3.21), also a static loss is included, mainly because of coupling loss (e.g. in optical TSVs, between laser and waveguide, waveguide and photodiode etc.). $L_{\text{static}} = 2$ dB is chosen as a realistic value – for example, a single TSV adds around 0.6 dB [115]. Depending on the waveguide type and technology, 0.1–2 dB/cm [16] are typical values for attenuation. Here, $L_{\text{wg,opt,dB}} = 1$ dB is chosen.

Also, the receiver sensitivity $P_{\text{Rx,opt,dBm}}$ has an impact on the required optical laser power at the transmitter and, consequently, on its electrical power consumption. In general, optimal optical receivers are shot-noise limited. However, for short-range unamplified direct-detection systems, using the thermal noise limit is a more realistic choice [24]. The photocurrent

$$I_p = \frac{\eta q}{h\nu} P_{\text{in}} \,, \tag{3.26}$$

generated by the incident optical power P_{in} with the optical frequency ν can be calculated with the quantum efficiency η, the charge of the electron q and Planck's constant h. The thermal noise with the Boltzmann constant k_B, the bandwidth B (increases with data rate), the temperature T and the load resistance R_L is

$$\sigma_T^2 = \frac{4k_BBT}{R_L} \ . \tag{3.27}$$

Thermal noise is white and Gaussian, therefore a simple equation can be used to calculate the receiver sensitivity from the signal-to-noise ratio required for a specific bit error rate

$$P_{\mathrm{Rx,opt}} = \frac{1}{R_0}\sqrt{\frac{\mathrm{SNR}\sigma_T^2}{R_L}} \ , \tag{3.28}$$

where

$$R_0 = \frac{\eta q}{h\frac{c_0}{\lambda_0}} \tag{3.29}$$

is the responsivity. For error-free (bit error rate $\mathrm{BER} = 10^{-12}$) OOK transmission with equally distributed ones and zeros, a Q factor $Q = \sqrt{\mathrm{SNR}} \approx 7$ can be found with

$$\mathrm{BER} = \frac{1}{2}\mathrm{erfc}\left(\frac{Q}{\sqrt{2}}\right) \ . \tag{3.30}$$

Larger data rates demand for higher bandwidths leading to more noise. Therefore, a high data rate of 100 $\mathrm{Gbit/s}$ is used for the numerical study. For operation in the third optical window ($\lambda_0 = 1550\ \mathrm{nm}$) at room temperature (290 K) and leaving some margin for practical implementation (e.g. non-ideal quantum efficiency leading to lower responsivity, additional noise, ...), $P_{\mathrm{Rx,opt,dBm}} = -10\ \mathrm{dBm}$ is chosen as receiver sensitivity for the numerical study.

Decreasing the voltage swings for the modulator drivers significantly decreased their power consumption in the past years. A modulation stage with a differential voltage swing of 6 V dissipates 34 $\mathrm{mW/(Gbit/s)}$ [72]. Being able to modulate with only 4 V lowered the power consumption to $E_{\mathrm{mod}} = 11\ \mathrm{mW/(Gbit/s)}$ [68] which is the value taken for the numerical analysis.

Numerical study

Although the introduced scheme allows a general evaluation, being able to present absolute power values helps to give a more practical impression. That's why in this section an exemplary system with a data rate of 10 $\mathrm{Gbit/s}$ is investigated. Figure 3.13 shows the consumed power with respect to transmission length. For the electrical multi-hop system, the contributions of E_{crossbar} and E_{buffer} at each hop can be observed in addition to the waveguide loss which is much higher for electrical interconnects than for optical interconnects. The electrical single-hop system is given as additional optimistic scenario, knowing that its power consumption is most likely underestimated by the linear approximation of the waveguide loss.

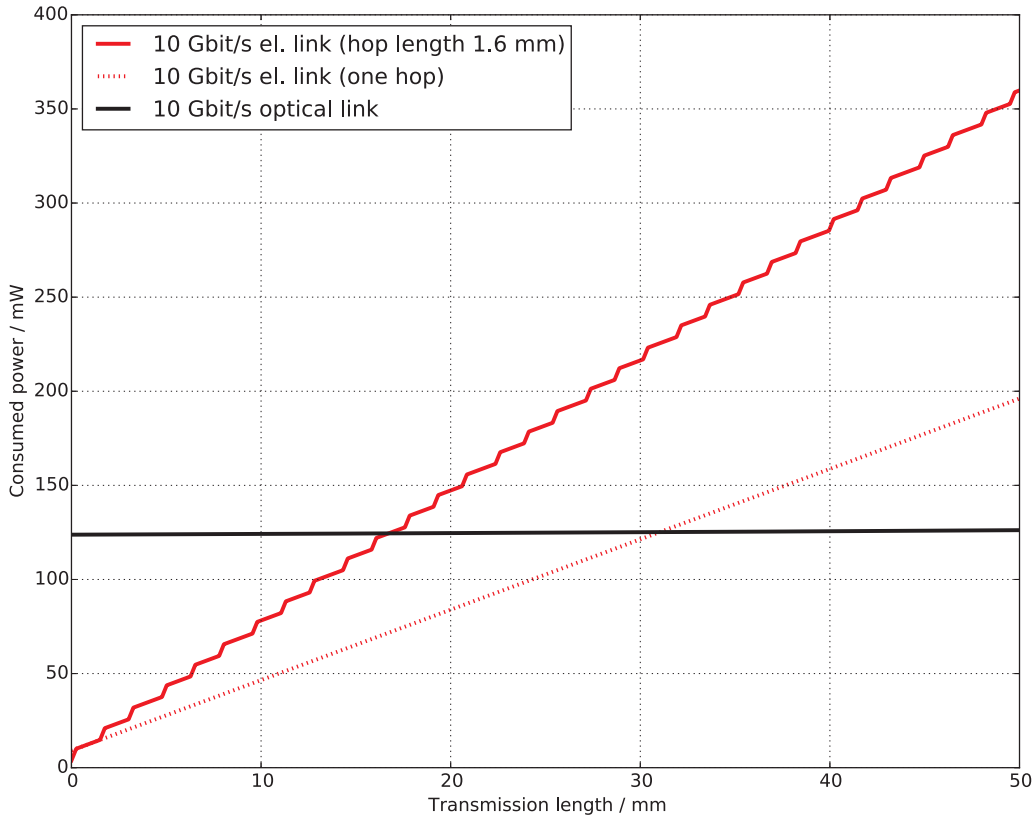

Figure 3.13: Power consumption for electrical (single hop and multi-hop with hop length 1.6 mm) and optical transmission at 10 Gbit/s depending on transmission length

Looking at longer distances, e.g. 100 mm, the optical interconnects are more energy-efficient (134 mW) than their electrical counterparts (650 mW / 350 mW). The power consumption of the optical interconnect is dominated by the laser and modulation stage (127 mW), the low-loss optical waveguide adds just 7 mW over 100 mm. In contrast, only 8 mW of the electrical interconnect power dissipation do not depend on transmission length. That's why it is more energy efficient than the optical interconnect for short distances below 17 mm (below 31 mm in the optimistic scenario).

Due to the low loss in optical domain, the laser only contributes around $1 \ldots 3$ mW to the 127 mW mentioned above. That's why receiver sensitivity or optical waveguide attenuation variations as well as changes in laser efficiency only have a small impact on the distance where optical and electrical interconnects consume the same amount of power.

In Figure 3.14, the influence of the transmitted data rate on the distance where optical interconnects become more energy efficient than electrical interconnects can

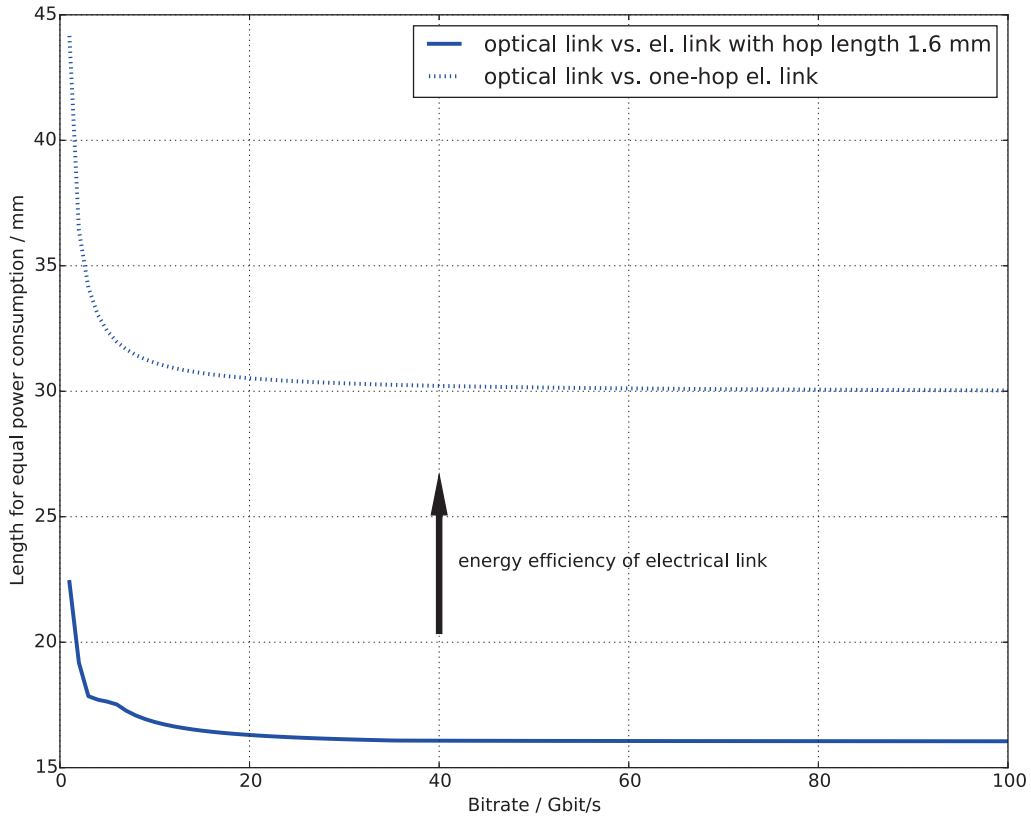

Figure 3.14: Data rate dependent length where optical systems start to consume less power than electrical systems (single hop, dashed line, and multi-hop with hop length 1.6 mm, solid line)

be seen. The electrical system as well as the modulation stage of the optical system are data rate dependent. The laser power is data rate independent. That means, for lower data rates, the electrical interconnects remain more energy efficient over longer distances. This distance goes down to a few centimeters with increasing data rate. Beyond 25 $\mathrm{Gbit/s}$, this distance does not decrease further, because the data rate dependent power consumption of the modulation stage in optical interconnects becomes dominant.

That means, for very small distance, electrical interconnects still remain more energy efficient in the moment. Increasing the energy efficiency of the modulation stage will enable optical systems that operate more energy efficient even for millimeter distances.

Approaches for improvement

As already discussed, the electro-optical modulation part has to be improved in terms of energy efficiency in order to provide competetive optical systems for short distances. In order to account for further improving electrical systems, the one-hop electrical system is used as benchmark. Current modulation stages based on directly modulated VCSELs dissipate 2 $\mathrm{mW/(Gbit/s)}$ [71]. An energy efficiency of 0.5 $\mathrm{mW/(Gbit/s)}$ has been reported for a free-space system at a data rate of 10 $\mathrm{Gbit/s}$ [28].

In Figure 3.15, the energy efficiency of the modulation stage is used as a parameter ($E_{\mathrm{mod}} = \{0.5, 1, 2\}$ $\mathrm{mW/(Gbit/s)}$, red lines) for the calculation of the distance where optical and electrical interconnects consume the same power. The system discussed before ($E_{\mathrm{mod}} = 11$ $\mathrm{mW/(Gbit/s)}$) is shown as reference in black. It can be seen that the improvement of the modulation stage allows to cover also small distances below 1 mm for data rates above 10 $\mathrm{Gbit/s}$.

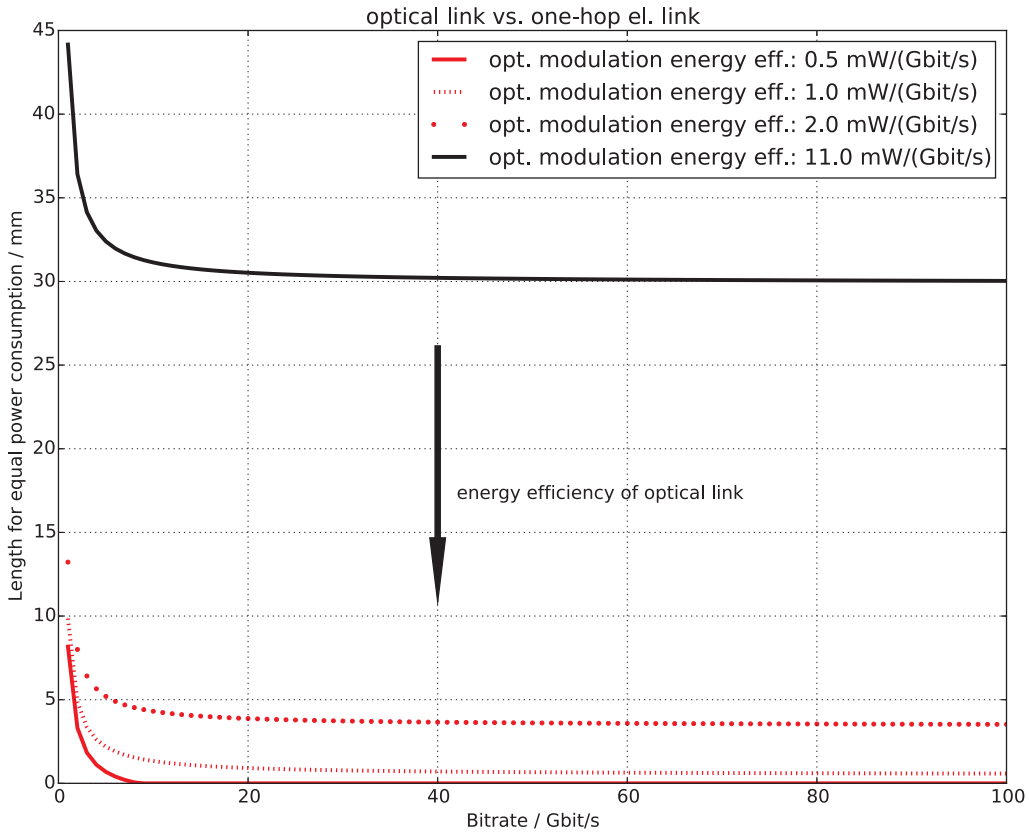

Figure 3.15: Bitrate-dependent length where optical systems with different energy efficiency of the electro-optical modulation stage consume less power than a single hop electrical system

However, data rates are supposed to increase in the future. Therefore, 50 $\mathrm{Gbit/s}$ are taken for some detailed analysis. For a distance of $d = 0.5\ \mathrm{mm}$, a laser power of $P_{\mathrm{laser}} = 3\ \mathrm{mW}$ is calculated with the assumed values which can be even lower with optimized lasers. This implies a required energy efficiency for the modulation stage of $E_{\mathrm{mod}} = 0.94\ \mathrm{mW/(Gbit/s)}$ in order to be as energy efficient as the electrical interconnect.

Although an energy efficiency of $E_{\mathrm{mod}} < 1\ \mathrm{mW/(Gbit/s)}$ means to use energy over 10 times more efficiently than today, this seems a realistic goal, according to Bergman's [14] technology forecast. It is clear that it can be only achieved when power consumption is tackled from different sides at the same time. In such a way, a self-enhancing effect can be used: For example, lower modulation voltages help to design low-power driver circuits. The realization of a modulator where voltage swings below 100 mV are sufficient [39, 131] is a big step towards this goal.

The co-integration of optics and electronics on one chip – silicon photonics – removes power-hungry interfaces [56, 90]. Also directly modulator lasers such as VCSELs are an interesting option. Apart from the component improvement, a paradigm change on the system side should be considered as well. Presently, performance still plays the major role in optical links. However, for ultra-short distances, the requirements can be lowered to achieve higher energy efficiency. For example, lowering the modulation indices and accepting nonlinear distortions (e.g. due to a bias point near the laser threshold) can drastically reduce the modulation voltages and therefore the power dissipation. In that case, the deterioration of the modulation extinction can be partly compensated by photodetectors with increased sensitivity. The nonlinear effects can be somewhat canceled by TIAs and laser or modulator drivers with pre-emphasis. This way, an error-free transmission at high data rates will still be possible.

As a conclusion, it can be expected that with enhanced technology and increasing data rates, optical systems are expected to be the energy efficient choice also for ultra-short distances on chip scale below one millimeter.

3.2 Board level applications

Becoming more efficient for increasing transmission distances, optical schemes on the board level have existed for a longer time. This use case seamlessly connects to the chip level considerations from the previous chapter. Thus, typical distances range from a few centimeters to some meters in HPC and datacenter applications. When connecting a larger area, a higher level of functionality and more options of linking wireless, electronic and optical technologies are possible.

Antennas can be integrated on board level, e.g. in printed circuit board (PCB) technology. This enables low-cost mass production. With increasing frequency, the level of integration can be boosted due to smaller antenna sizes. Beyond 60 GHz, on-chip integration becomes an interesting option. However, the loss of electrical waveguides increases with frequency, too. Thus, switching to optical domain becomes

an interesting option. The superior features of optical waveguides paved the way for concepts like Radio-over-Fiber or Fiber-to-the-Antenna (FTTA). The RF hardware is concentrated in remote central stations and permits building cost-effective remote antenna sites [48, 138]. Single antennas with an optoelectronic conversion directly at the feeding point of the radiating structure have been proposed [160] less than 10 years ago.

The increasing frequency also implies higher bandwidths. For phased arrays, true time delay (TTD) techniques are advantegeous for broadband systems because they can ensure a main lobe angle that is independent from frequency. Photonic beam forming networks have been used to implement such TTDs [31, 109]. In contrast to single element antennas, the arrays remained hybrid systems where electrical waveguides connected the optoelectronic conversion stage with the antenna elements [96]. The best way to overcome the imperfections of electrical waveguides (loss, weight, electromagnetic interference) is to perform the optoelectronic conversion directly at the feeding point of the antenna (as for single element antennas). Especially transmitting antenna arrays can be realized with that approach and will be discussed in section 3.2.1 [106, 108].

Also receiving antennas are needed to build a full-duplex FTTA system as described in chapter 3.3.2. In this situation, a weak radio signal received by the antenna structure has to be modulated on an optical carrier. Electro-absorption modulators can be used [139, 154]. The need for an external laser source attached to the modulator and the integration with advanced antenna structures (supporting higher bandwidths, more gain etc.) are huge challenges in this approach. Directly modulated VCSELs combine the laser source and the data modulation in one unit and have been integrated e.g. with a patch antenna [133]. However, VCSELs are uncommon for the transmission in the third optical window around 1550 nm over standard singlemode fiber. In section 3.2.2, the design and the properties of a realized fiber-coupled Rx antenna that comes with its own DFB laser source at 1550 nm and, consequently, can be seamlessly integrated into existing SMF networks are presented [100]. This paves the way for advanced broadband antenna structures combined with active electronic circuits on one board.

Realizing optical functions on board-level, i.e. their integration into PCBs [21] is an important step towards more sophisticated microwave photonic systems. Not only waveguides [73] but also more complex components such as couplers or interferometers can be realized. For the coupler [85] it could be shown that for data rates of up to 2.5 $\mathrm{Gbit/s}$ no performance deterioration could be seen (bit error rate of $1 \cdot 10^{-7}$). This implies that the transmission of a wireless signal in the 2.4 GHz ISM band will be possible without problems. The upper frequency of the transmission involving the investigated on-board waveguides and coupler is currently limited by the available components for opto-electrical and electro-optical conversion.

Another important task is the RF generation which can be performed in optical domain. In chapter 3.2.3, Talbot effect based RF generation is addressed. Using this technique, the high frequencies that can be generated [102] are only limited by the opto-electrical conversion. Moreover, phase noise can be mitigated by using narrow

pulses. However, the broad combs of such sources require an arbitrary dispersive element for efficiency optimization [103].

3.2.1 Photonic Tx antenna array

A photonic transmit antenna array consists of radiating elements where the opto-electrical conversion takes place directly at the feeding points of these elements in order to minimize electrical connections. As a first step, the design of the radiating elements is explained. For an array, a beam forming network is needed. In this approach, the network is realized all-optical and will be introduced afterwards. Finally, the antenna array is characterized. The results are discussed at the end of this chapter.

Antenna design

For broadband antennas that can be manufactured in a PCB process, Vivaldi structures are a good candidate. In order to keep the demonstrator cost-efficient, the electronic circuits and optoelectronic components limiting the upper frequency of the antenna system were chosen to support up to 2.5 GHz. The antenna element should be as broadband as possible. One measure for this is the relative antenna bandwidth

$$B_{\mathrm{rel,antenna}} = \frac{B_{\mathrm{antenna}}}{f_{\mathrm{center}}} \tag{3.31}$$

which is the relation between the bandwidth of the antenna B_{antenna} and its center frequency f_{center}. Vivaldi antennas are known to be able to cover a wide bandwidth range. However, to limit the antenna size, the lower frequency was restricted to around 500 MHz. That means, a relative antenna bandwidth of 133% (2 GHz, antenna center frequency is 1.5 GHz) was realized. A broadband Vivaldi antenna [50] operating between 500 MHz and 3 GHz was chosen as basis that will be extended to an array and matched to the optoelectronic converter. This photoreceiver (PD-LD PTIN2.5) is equipped with an integrated transimpedance amplifier (TIA) and an automatic gain control (AGC). The measured transfer function of the photoreceiver is shown in Figure 3.16. The 3 dB bandwidth is around 1.6 GHz, i.e. below 2.5 GHz. However, the antenna gain typically increases with frequency so that these effects can partly compensate and lead to a flat system frequency response when properly designed (Figure 3.17). It is also worth mentioning that for lower optical input powers, the roll-off is steeper because of the AGC.

To operate the photoreceiver, a supply voltage of 3.3 V is required. Here, it is provided by an external power supply connected with an SMA connector to the rear end of the antenna. When power autonomy is needed, a battery may be used. For applications with galvanic isolation, power-over-fiber is an interesting option [134].

Feeding the antenna is carried out by placing the output pins of the photoreceiver at both sides of the antenna. The optimal feeding point was found by simulating a 2x1 subarray (shown in Figure 3.18 a)) considering the electrical properties of the photoreceiver. The best matching for the required frequency range has been

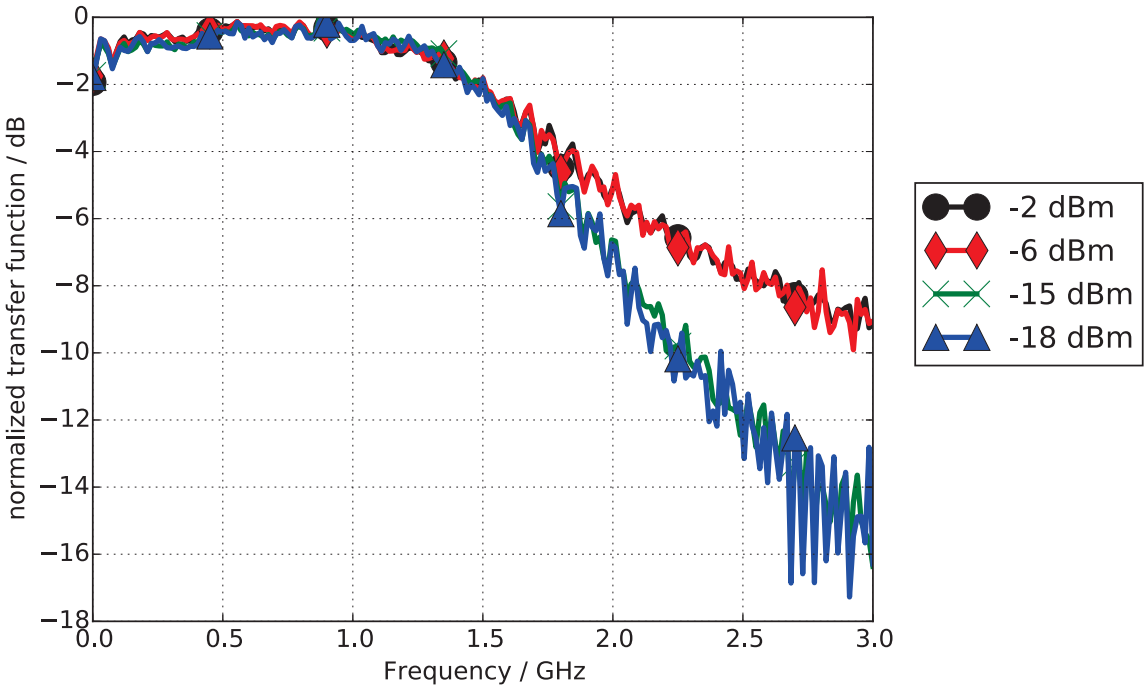

Figure 3.16: Measured transfer function of the photoreceiver PD-LD PTIN2.5 with TIA and AGC for different optical input powers

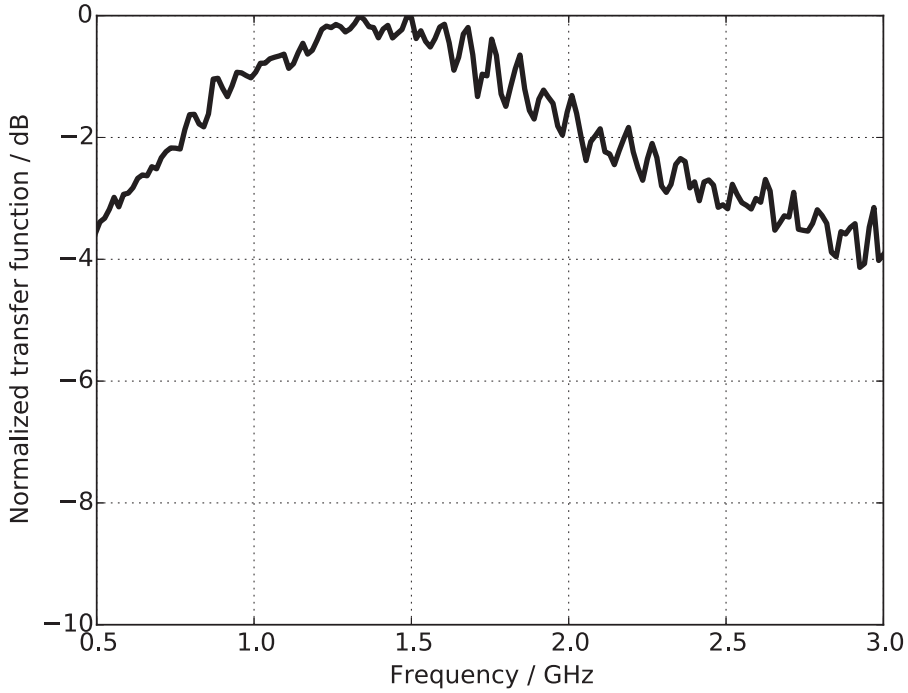

Figure 3.17: Measured transfer function of a fiber-coupled transmit antenna

achieved when feeding the antenna near its resonator (see Figure 3.19). Due to the mechanical dimensions of the photoreceiver, 3 mm was the optimum distance from the feeding point to the resonator. Combining two 2x1 subarrays leads to the 2x2 array configuration (Figure 3.18 b)) used in the experiments.

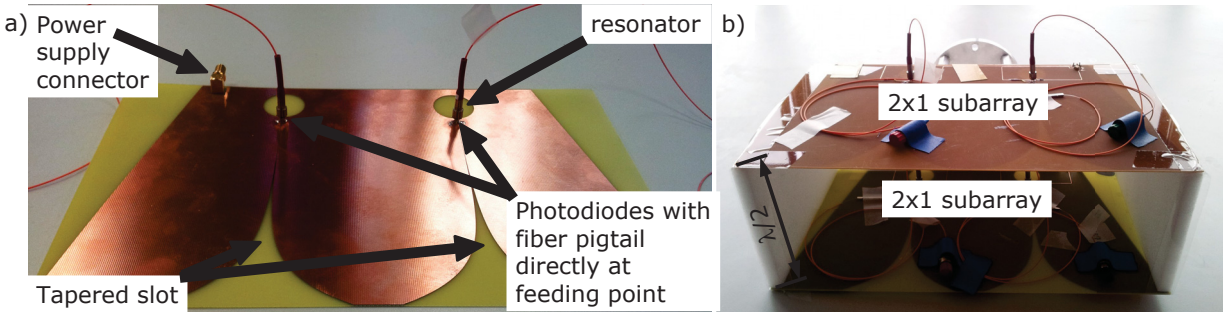

Figure 3.18: a) 2x1 antenna subarray fed by photodiodes connected by optical fiber, b) 2x2 antenna array configuration consisting of two stacked 2x1 subarrays

Optical feeding network

Antenna arrays require a feeding network that distribute the signals to the antenna elements. The amplitude and phase distribution determines the shape of the pattern of the phased array antenna [11]. Converting from optical domain to electrical domain at the feeding point of the antenna elements implies an optical feeding network. Here, a uniform amplitude distribution is chosen. That means, a good amplitude balance is one of the requirements of the optical feeding network. The choice of photodiodes with TIA and AGC helps to fulfill that demand. The TTD for the antenna elements is implemented by the length difference between the paths from the input to the antenna.

A realization in fiber technology ensures low loss. That's why fiber couplers are used. Typically, 2x2 and 3x3 couplers can be produced. Due to symmetry reasons, 3x3 couplers have a coupling ratio of the outputs in the form of $a : b : a$ with $2a + b = 1$ for power conservation. 2x2 couplers are available with arbitrary coupling ratios $a : b$ with $a + b = 1$. Cascading both types, any number of antenna elements can be supported.

As stated in the previous section, a 2x2 antenna array will be realized. Figure 3.20 shows the structure of the optical feeding network for this four-element array. Its first part splits the signal using three cascaded 2x2 couplers produced in-house. For equal amplitude distribution, the coupling ratios have to be $a = b = 0.5$ (3 dB couplers). The required length differences are produced by fiber patch cable sets spliced to the respective lengths. The steering angle Φ of the antenna array is connected with the length difference ΔL resulting in the TTD as follows

$$\Phi = \arcsin\left(\frac{N\Delta L}{d}\right) . \tag{3.32}$$

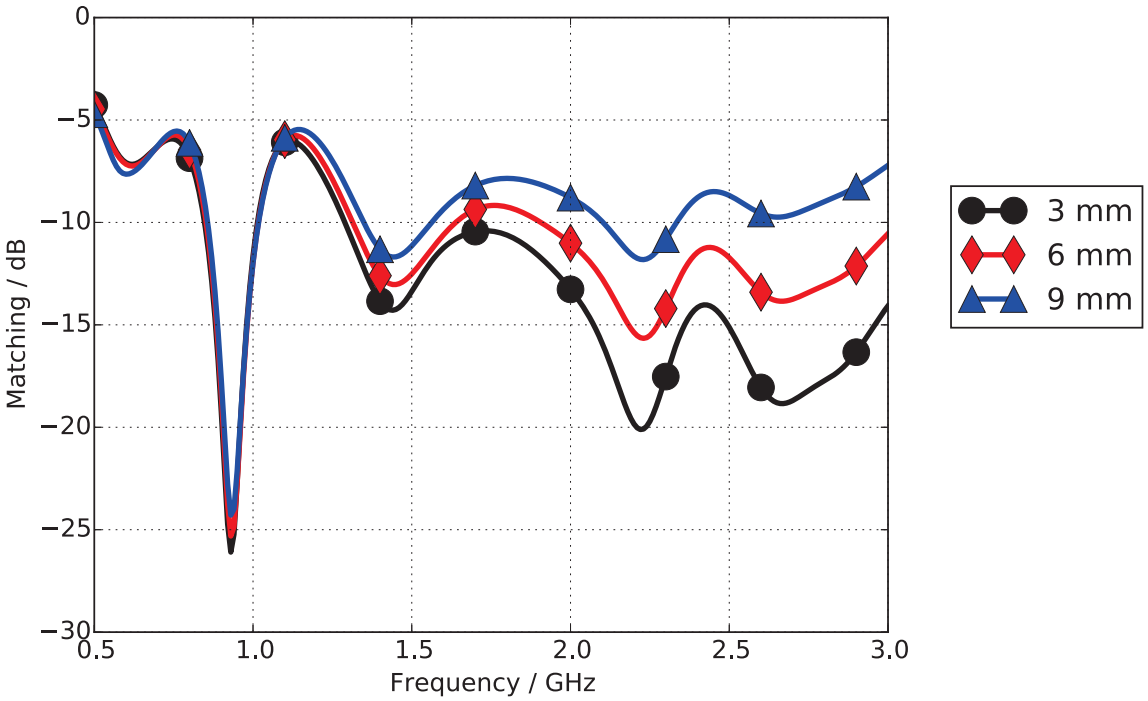

Figure 3.19: Matching of the Vivaldi 2x1 subarray depending on the feeding point distance to the resonator

The antenna element spacing d is 100 mm ($\frac{\lambda}{2}$ for the center frequency of 1.5 GHz) in the realized array. The geometrical length of the fiber ΔL is scaled by its group refractive index $N \approx 1.5$.

In theory, the insertion loss (IL) on each output port of the feeding structure is 6 dB. However, the input and output connectors, the couplers and the splices add more attenuation as summarized in Table 3.3.

Table 3.3: Attenuation of elements of the feeding structure

Element	**typ. loss / dB**	**number of elements in path**	**total loss / dB**
splitting	6	1	6
connector	0.3	2	0.6
2x2 coupler	0.25	2	0.5
splice	0.2	3	0.6
total			7.7

The splitting section of the optical feeding structure has been characterized concerning loss using an optical loss test set and concerning path length difference using an optical vector analyzer in the OFDR mode. As shown in Table 3.4, the IL varied between 8.0–8.7 dB which is in the expected range. The imbalance of the outputs is

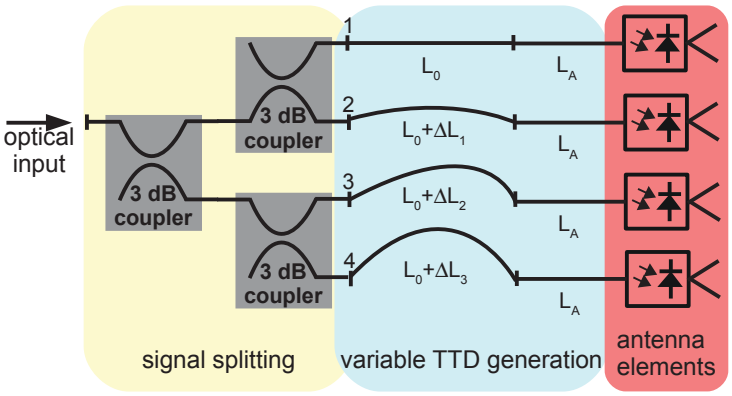

Figure 3.20: Optical feeding network consisting of signal splitting section, TTD generation section connected with the antenna array elements

below 1 dB and the splitting part produced a total loss of 2.3 dB. The loss caused by the fiber length (typ. 0.2 dB/km for standard single-mode fiber) can be neglected. Although this is already a small value compared to electrical beam forming networks, with increasing frequency as well as with increasing length, optical systems become more advantegeous. This is a general behavior of optical systems also discussed in chapter 3.1.3 for chip level intraconnects. The relative length difference between the outputs was below 1 mm. Using equation (3.32), the worst-case angular deviation of the main lobe of the array caused by the optical feeding network can be calculated. As summarized in Table 3.4, it stays below 1°. Please note that the length deviations of the splitting sections can be corrected by adjusting the lengths of the fiber patch cables that provide the TTD.

Table 3.4: Attributes of the splitting section of the optical feeding structure

output	**IL** / dB	**length diff.** / mm	**max. angular deviation** / °
1	8.7	0.107	0.09
2	8.2	0.721	0.62
3	8.0	ref. (shortest)	0
4	8.3	0.779	0.67

To drive the 2x2 antenna array, its two 2x1 subarrays were fed with the same delay between the antenna elements. The array could be steered to different angles by switching between three pairs of fiber patch cables. Their length difference was 11.2 mm, 21.1 mm and 38.3 mm corresponding to 52 ps, 133.7 ps and 186 ps TTD. The length difference between the pairs adds less than 0.3° angular deviation of the main lobe. The properties of the fiber patch cables can be found in Table 3.5.

Table 3.5: Fiber patch cable sets generating TTD

Cable	**abs. length** / mm	**length diff. to ref.** / mm	**length diff. in pair** / mm
1.1	424.82	ref.	-
1.2	424.88	0.06	0.06
2.1	436.11	11.23	-
2.2	436.23	11.25	0.02
3.1	463.11	38.29	-
3.2	463.31	38.49	0.2

By properly combining the patch cables and the splitter outputs, the length deviations partly compensate which lowers the already low deviation of the main lobe from its intended value. Table 3.6 shows the TTD that will be used in the following antenna array measurements to steer the main lobe. For TTD0 pointing at 0°, only the splitter is used. TTD52 is achieved using the cable pairs 1 and 2, TTD134 using pairs 2 and 3. Finally TTD186 is formed by connecting the sets 1 and 3.

max. angular deviation / °

Table 3.6: TTD configurations (splitter + patch cables)

TTD setup	**rel. length** / mm	**generated TTD** / ps	**array angle** / °
TTD0	only splitter	0	0
TTD52	10.6	52.3	9
TTD134	27.1	133.7	24
TTD186	37.7	186.0	34

Measurements

Connecting each 1x2 subarray with one of the manufactured cable pairs, the 2x2 antenna array was steered in its horizontal axis using the different available configurations TTD0, TTD52, TTD134 and TTD186. The sign of the angle could be synthesized by switching the cable pairs and therefore inverting the time delay. In an anechoic chamber, the patterns of the antenna generated by different configurations of the optical feeding network have been measured.

Without delay (TTD0), the antenna points to 0° direction (Figure 3.21 a)). The TTD52 (52 ps true time delay) configuration steers the beam to 9° (Figure 3.21 b)). Measurements pointing to 19° and -34° using 154 ps and -186 ps TTD are shown in Figure 3.21 c) and d). Data for the low, center and upper frequencies is

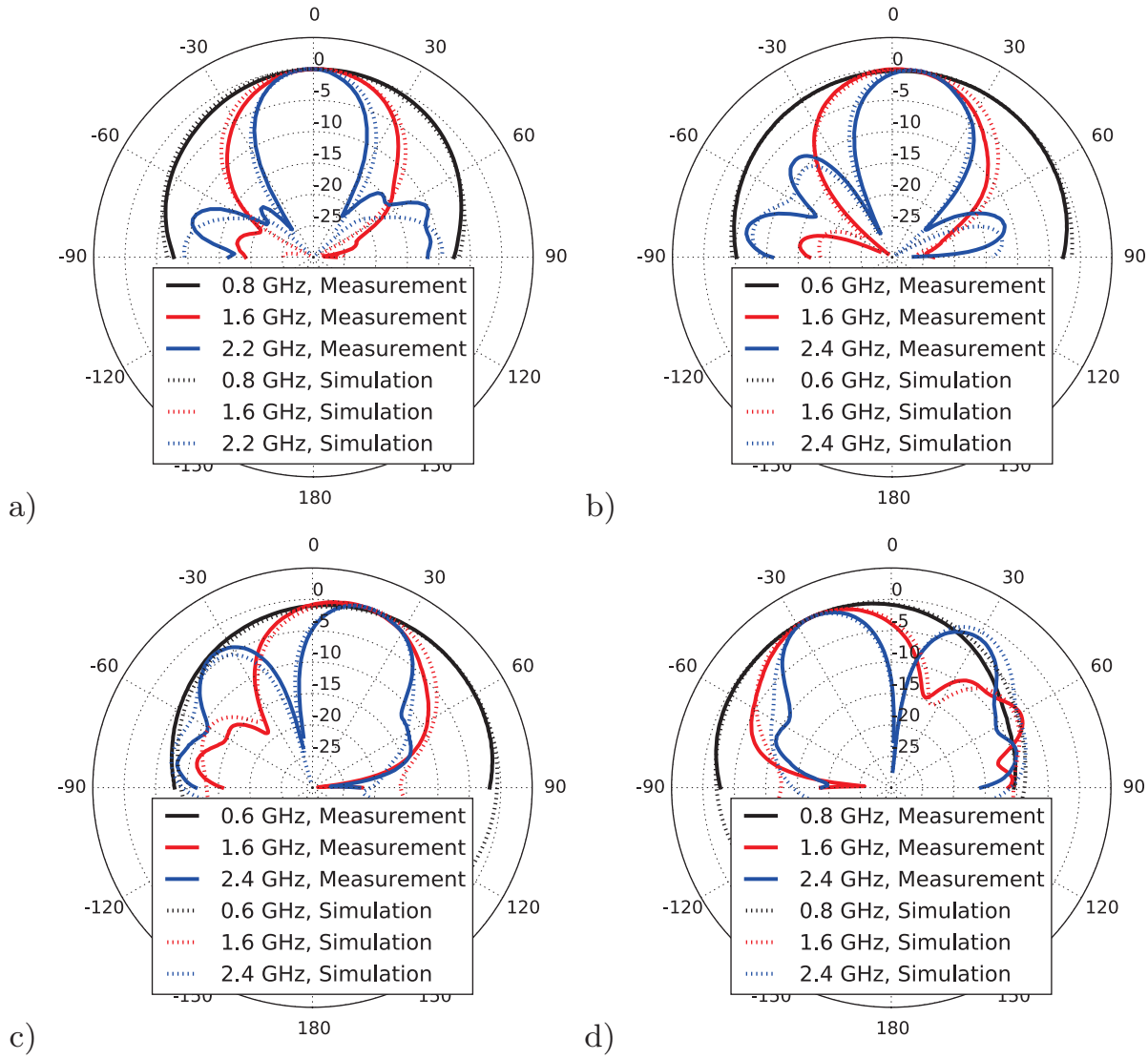

Figure 3.21: Antenna pattern: a) TTD0 without delay, b) TTD52 in pos. direction, c) TTD134 in pos. direction, and d) TTD186 in neg. direction

depicted. The measured values are plotted as solid lines and the simulation results from numerical field simulations are drawn as dashed lines.

The measurement results match very well the simulated values. As expected for TTD steering, the main lobe points at the same direction regardless of the frequency. Its maximum is at slightly lower angles than expected from theory (summarized in Table 3.6). This deviation is caused by the cross-coupling of the antenna elements which was not considered in the theoretical calculations. In the numerical field simulations, this effect is included. It can be reduced e.g. by increasing the number of antennas in the array.

Figure 3.22 depicts the dependency of the main lobe angle on the frequency. As stated before, TTD steering minimizes this effect which can be observed in the plot. Working with a small array, the main lobe is comparably wide. This leads to an

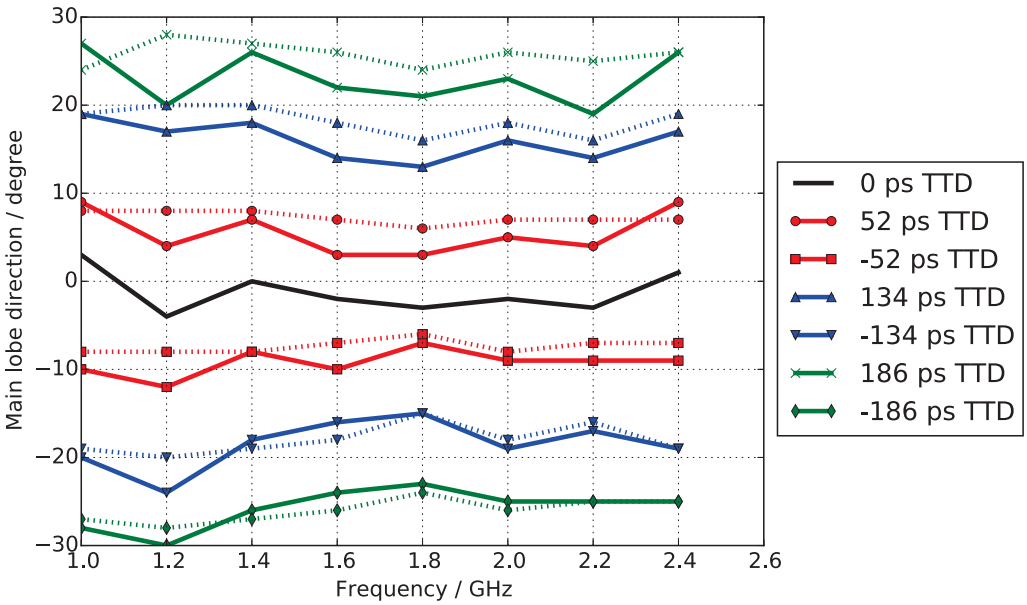

Figure 3.22: Main lobe direction depending on TTD, measurement (solid line) and simulation (dotted line) as function of frequency

uncertainty of the estimation of its maximum of 2–3°. Other deviations may be caused from electrical dispersion. Dispersive effects in optical domain (experimentally verified with up to 1284 $\mathrm{ps/nm}$ in the link between optical source and feeding network) did not have any measurable influence on the antenna pattern.

It is worth mentioning that the feeding network can be used as well for other antenna arrays working at completely different frequencies due to the broadband nature of the fiber and the TTD properties.

Conclusion

Fiber-coupled antenna arrays are one important example for microwave photonics on board level. The signal is transported in optical domain to the antenna and radiated. For an array, also the beamforming takes place in optics, i.e. the feeding network is realized using optical waveguides rather than electrical ones. That may be beneficial in terms of size, weight, routing (optical waveguides may cross) and electromagnetic compatibility – to name some advantages. The presented concept is scalable in frequency. As a matter of fact, for higher frequencies optical transmission becomes even more appealing. With silicon photonics, the optical part, photodiode, optional electronics (e.g. amplifiers) as well as the antenna can be co-integrated on a chip.

The design process covered aspects like antenna design and optimization (merely in electrical domain), selection of the opto-electrical converter as well as design and manufacturing of optical components like the feeding network. Hence, it is a good blueprint how to perform a microwave photonic development. The next chapter deals with the complement device – a fiber-coupled receiving antenna.

3.2.2 Photonic Rx antenna

To match the transmit antenna array in the previous section, the same frequency range (500 $\mathrm{MHz}\ldots$ 2.5 GHz) was chosen. The lower frequency limit is determined by the antenna. The cutoff frequencies of the electronic circuits and the laser diode fix the upper frequency limit. For compatibility with standard DWDM transmission in the third optical window, a DFB laser diode emitting at 1550 nm connected to standard singlemode fiber is used. The optical output power of 2 mW enables distances in the range of tens of kilometers.

First, the antenna design will be discussed where the matching between antenna and low noise amplifier (LNA) is crucial. Then, the design of the electronic circuits shaping the received signal for direct modulation of the DFB laser diode is focused.

Antenna design

The well-proven Vivaldi antenna design from the transmitting antenna is used as starting point for the design process. The planar antenna element realized on a common FR4 substrate was optimized regarding different demands. The matching (S_{11}) to the single-ended 50 Ω LNA could be improved by tuning the resonator.

The field distribution over the slot provides a differential signal. Hence, a radial stub on the back side of the antenna is needed to form the interface to the microstrip line connected with the single-ended LNA. The radius of the stub and its opening angle have been optimized using numerical simulations. Also, the position of the microstrip line has been fine-tuned to achieve optimal matching.

The electronics for amplification and modulation accomodated on the antenna is located on the backside of the antenna. The resulting reduction of the ground plane, the lines on the front side as well as the vias may change the antenna geometry and therefore its properties. However, simulations showed that the effect can be neglected when the area with the circuits is properly placed. In that case also the type of ground connection (none, one narrow contact, full connection) of the circuitry is uncritical.

Table 3.7: Antenna properties

Parameter	**Value**
Dimensions	250 mm$\times$ 200 mm
Substrate	8 mm FR4
Slot width	0.19 mm
Slot cavity radius	17 mm
Microstrip feed width	1.2 mm
Radial stub radius	19 mm
Radial stub angle	99°

It is obvious that all the aforementioned parameters have cross-dependencies. Therefore, a global optimization has been performed using the optima from the inde-

pendent simulations as starting values. The final antenna properties are summarized in Table 3.7.

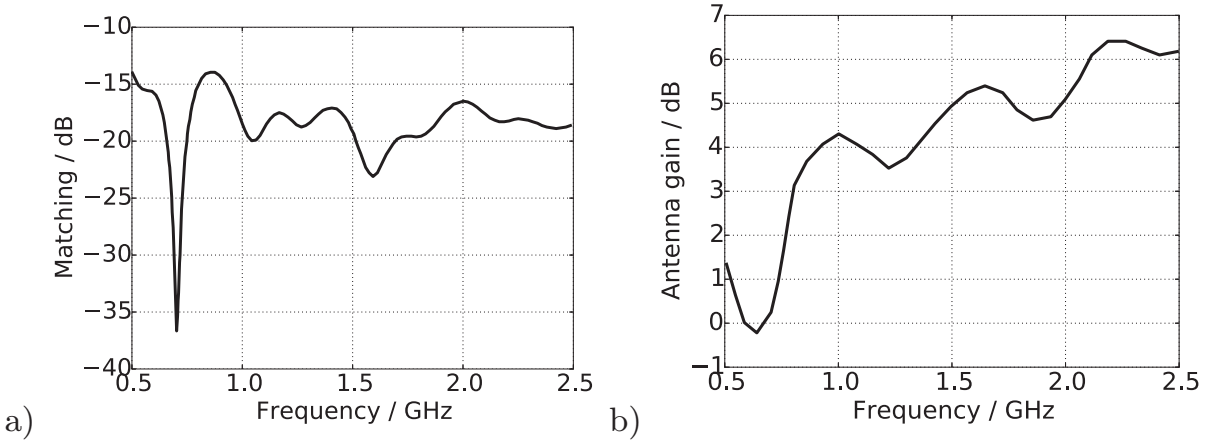

Figure 3.23: Simulated frequency-dependent antenna properties: a) matching (S_{11}), b) antenna gain

The simulated characteristics of the Rx antenna are shown in Figure 3.23. A very good matching (below -10 dB) was achieved over the whole frequency range. The increasing gain with growing frequency is a typical feature of broadband antennas. This feature helps to flatten the frequency response of the active Rx antenna system because it works against the decreasing gain of the electronic amplifiers and the increasing loss in the electronic part.

In order to characterize just the antenna parameters, first the antenna characteristic without laser diode driver electronics and optical transmission has been evaluated. A SMA connector has been soldered to the feeding point of the antenna. Figure 3.24 shows the measured antenna patterns in the xz-plane as well as in the yz-plane. The electrical circuit only has a very small influence on the pattern.

In Figure 3.25, a photograph of the realized antenna is depicted. On the backside of the antenna, the electronics part including the laser diode as well as the radial stub can be seen.

If an antenna array (like the Tx antenna system in section 3.2.1) shall be produced, two options are available. The first way is a standard antenna array including all electronic circuits, phase shifters, LNAs etc. with an electrical beam forming network. The combined receive signal of this array is converted to optical domain and transmitted over fiber just like for a single-element antenna. However, a huge effort in electronics including a control plane to set the phase shifter etc. would be needed. From an economic point of view, in most cases that will not be feasible. The second option is to convert the incoming signal of each antenna element to optical domain and transmit them over fiber. In order to enable remote beam forming, the relative amplitude as well as relative phase information has to be maintained. This is a critical endeavor because of the high numbers of electro-optical conversions. Additionally, preserving the exact length relations between the numerous optical paths to

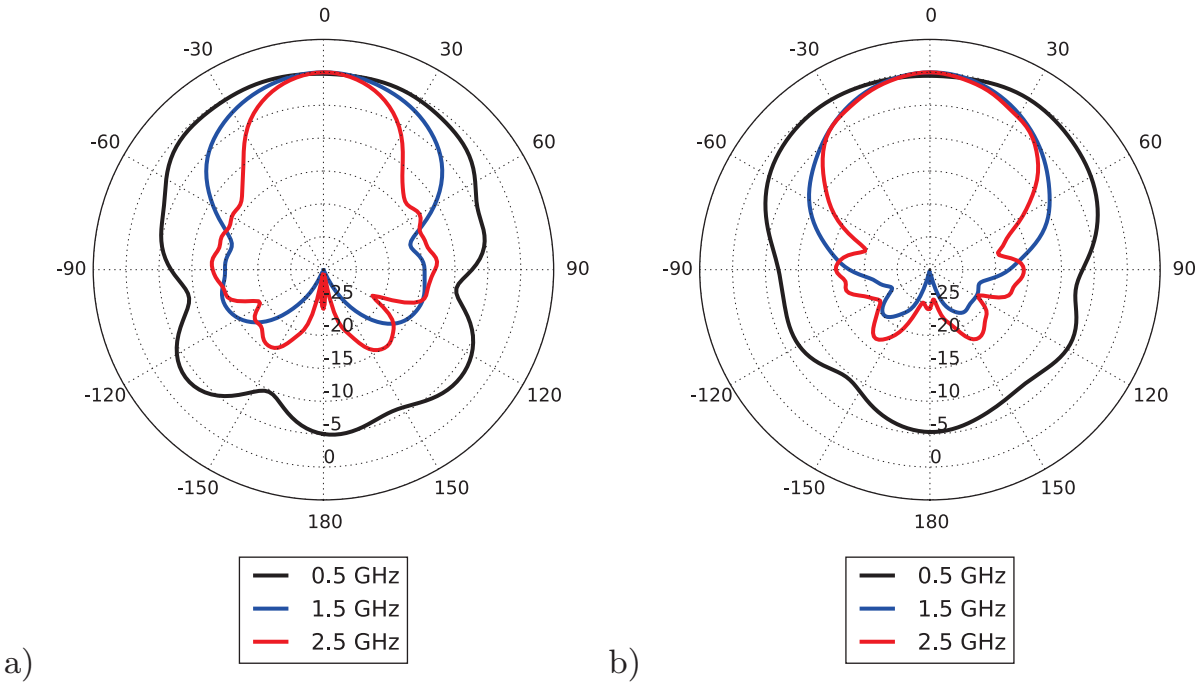

Figure 3.24: Measured frequency-dependent radiation patterns of the antenna with bypassed electronics: a) xz-plane, b) yz-plane

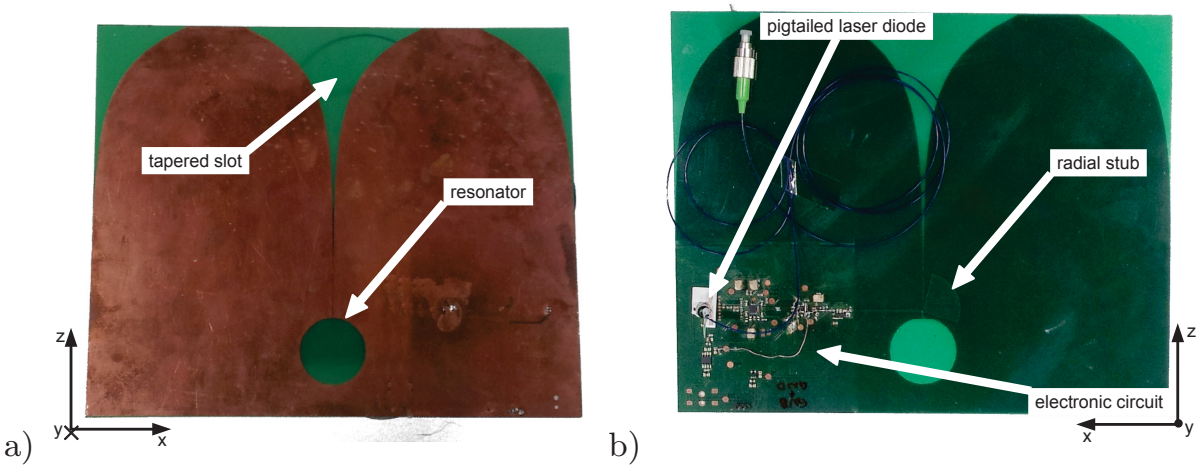

Figure 3.25: Photographs of the Rx antenna: a) front side, b) back side of antenna with electronic circuit and radial stub

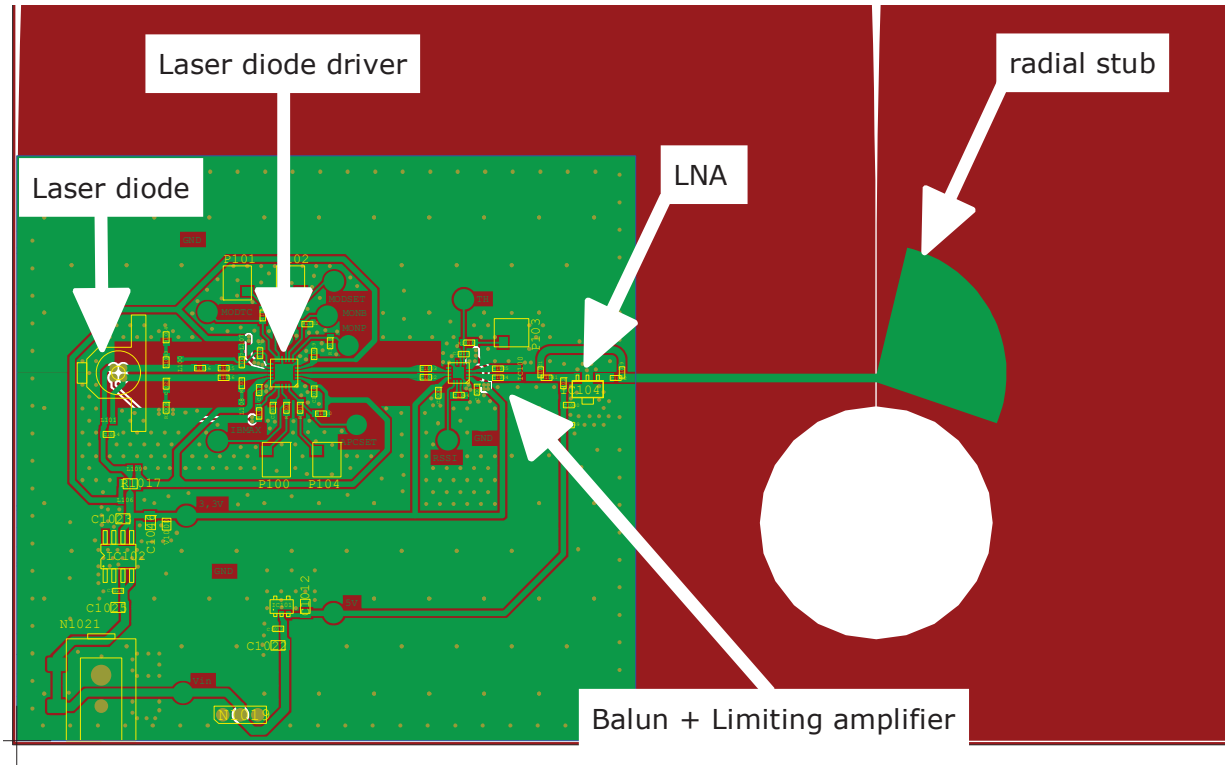

Figure 3.26: PCB part at the backside of the antenna

avoid undesired phase changes is challenging, too. The only imaginable technology is integrated optics which may be interesting especially for higher frequencies.

Electronics design

The feeding point of the Rx antenna is connected with a microstrip line (50 Ω, 1.5 mm width) to the single-ended LNA (HMC639ST89E, 10 dB gain). The rest of the circuit uses differential signals. That's why a balun (RFXF9504, 3 GHz bandwidth and 2 dB loss) is needed. The balanced lines (100 Ω, 0.63 mm width and 0.3 mm distance) connect the balun with a matched pair of limiting amplifier (ONET4201PA, min. 5 mV_{pp} input voltage, 760 mV_{pp} output voltage and max. 50 dB gain) and laser diode driver (ONET4201LD). Short lines ($< \lambda/16$) do not require impedance matching. Finally, the electro-optical conversion takes place at the directly modulated DFB laser diode (DFB-1550-C5-2-A4-FA-A-A). The electronics support input powers from the antenna of less than -30 dBm.

In Figure 3.26, the PCB part of the antenna is shown. The RF electronics as well as the corresponding power and bias networks can be seen. An external power supply or battery providing $6 \ldots 10\,\mathrm{V}$ has to be attached. Battery power enables maximum freedom of operation and full galvanic isolation. This can be of interest for outdoor applications with lightning hazard as well as measurement applications (e.g. over-the-air (OTA) scenarios with no defined ground level). Anyway, battery lifetime limits this

scenario. A battery-buffered power-over-fiber approach is an interesting option. Using a second fiber or the same fiber as for the signal at a different wavelength, multi-cell power converters may be used to provide up to a few hundreds of milliwatts [134].

Antenna system performance

The most important feature of the antenna system is its frequency characteristic. It can be measured by connecting the output port a network analyzer to a test antenna. The electromagnetic waves radiated by a known test antenna are received by the fiber-coupled antenna system and transmitted over single-mode fiber. A high-bandwidth photodiode (XPDV3120R, 70 GHz bandwidth) is used to convert the optical signal back to electrical domain. The measured values at the input port of the network analyzer are hardly affected by the photodiode because its bandwidth is much higher than the bandwidth of the measured antenna. The frequency characteristic (S_{21}) depicted in Figure 3.27 is flat in the antenna's range of operation. As designed, the increasing gain of the antenna (Figure 3.23 b)) compensates the decreasing frequency response of the electronics. Above its threshold, the limiting amplifier keeps its output level constant and, therefore, also partly compensates loss and frequency response of the LNA and the microstrip lines.

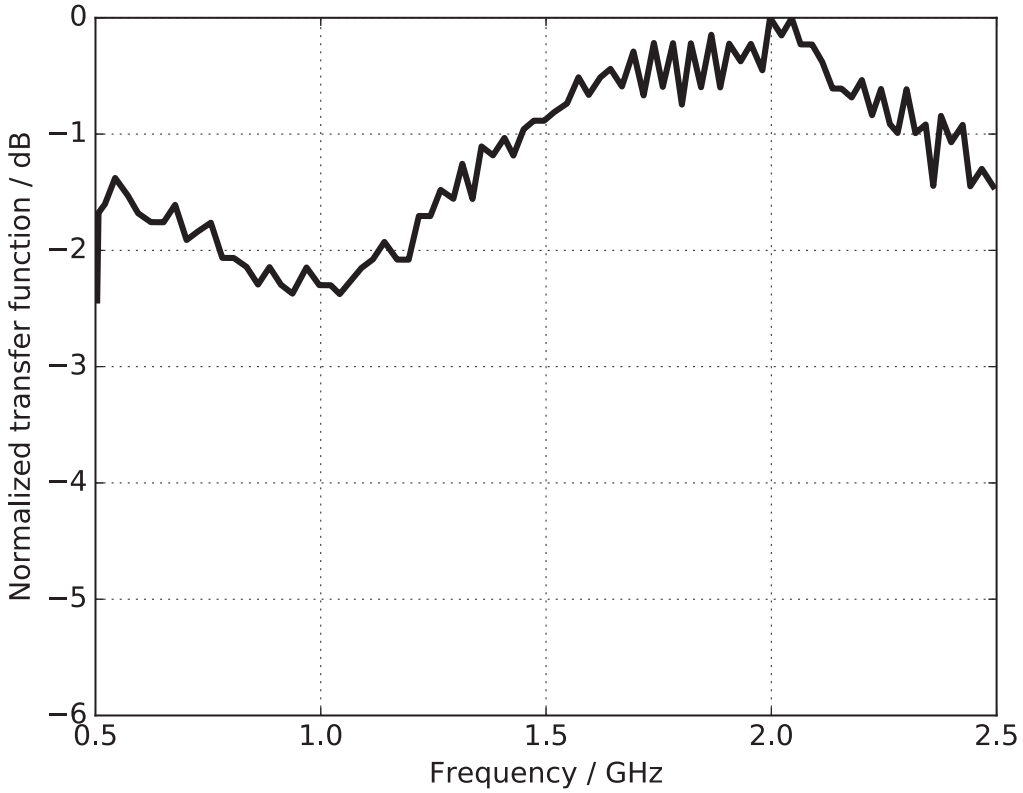

Figure 3.27: Measured frequency characteristic of the fiber-coupled active Rx antenna system

Conclusion

The fiber-coupled receiving antenna presented in this chapter is complementary to the transmitting antenna array proposed in the previous section. In the design process, topics from the optical field like laser modulation meet antenna design and issues like the influence of circuits realized on the antenna blade on its radiation characteristic. A broadband receiving antenna including an electro-optical conversion stage could be realized on a PCB. The fiber output can be directly connected to any single-mode fiber based access network enabling fiber-to-the-antenna (FTTA) concepts. Together with the transmitting setup, a full-duplex FTTA system can be realized and is demonstrated in chapter 3.3.2.

Another important aspect for microwave photonic systems is the carrier generation. While the transmit and receive antennas rely on existing carriers, a full Radio-over-Fiber system has to provide the wireless carrier. Besides a purely electrical solution, also optical generation has some interesting features. In the next section, a particular solution based on the temporal Talbot effect and its properties is introduced.

3.2.3 Photonic RF generation using temporal Talbot effect

High frequency sources are needed in a wide field of applications such as Radio-over-Fiber links, RF communications and radar systems. The complexity and cost of the electronic generation increases with frequency. Today, commercial components for the generation up to 20 GHz are widely available. However, there is a growing demand for the generation of frequencies of 60 GHz and higher which is still challenging. Integrated semiconductor solutions are constantly improving in performance and cost effectivity but new hybrid (RF and photonics) approaches may lead to compelling advantages. This applies especially for systems where optical components are already present. While later in chapter 3.3 the focus is on systems, here the RF generation process itself will be concentrated on.

Using optics for millimeter wave generation opens a wide range of possibilities such as realizing sources with lower noise and the possibility of low-loss transmission. Special dual-wavelength fiber ring lasers can be designed [25, 82]. External modulators can be used for frequency upconversion [120, 123], too. The temporal self-imaging (Talbot) effect is also a promising approach for an energy efficient RF upconversion with noise suppression. Pulsed lasers with and without external modulators have been used in conjunction with chromatic dispersion to generate RF tones [7, 8, 9, 65]. In the following subsections, a simple and straight-forward setup using a pulsed laser source and standard single-mode fiber is presented. The fiber provides the chromatic dispersion needed for Talbot effect based RF signal generation.

Being the most important parameter in the design and application of microwave CW sources, phase noise and jitter, its time-domain representation, directly affect the system margin of digital communication systems [37]. Hence, the noise sources and their interaction have to be understood thoroughly. Generating the RF tone by means of optics, the special noise properties caused by the Talbot effect [45, 46, 119]

as well as the noise contribution of the laser source [116, 117, 147] have to be taken into account for a system assessment. Consequently, the principle of the temporal self-imaging (Talbot) effect is introduced first. Then, the different contributions to the phase noise are investigated and the corresponding measurements are discussed. Finally, the conclusion points out guidelines for the design of a photonic low phase-noise RF generation by means of the Talbot effect.

Principle of operation

RF upconversion with the Talbot effect needs a source with a comb spectrum, i.e. a pulsed source. The spectral width of the frequency comb is determined by the pulse width, the line spacing is determined by the repetition frequency of the pulses. This spectrum will be discussed in more detail later.

At a photo diode, the spectral lines heterodyne with each other. A frequency-dependent delay in the optical domain between the different contributions to one frequency leads to a phase difference of these contributions in the electrical domain. Any dispersive element may provide this properties. An optical amplifier compensating loss may be added.

If the mixing between the different frequency lines of the comb results in an electrical phase of zero the resulting frequency and all of its harmonics superimpose constructively. An electrical phase of zero can be achieved for a spacing between the spectral lines that equals the repetition frequency by an accumulated dispersion of [62]

$$DL = \frac{c_0 T_r^2}{\lambda^2} \ , \tag{3.33}$$

where D is the dispersion parameter and L is the length of the fiber, c_0 is the speed of light, T_r is the repetition rate of the pulsed source and λ is the laser wavelength. For spectrally broad combs, higher order dispersion may become an issue.

Integer fractions of that characteristic dispersion DL lead to the restoration only of higher frequency components of the pulses. The integer fraction equals the multiplication factor m. The frequency at m times the repetition frequency and all its harmonics are reconstructed by constructive superposition. The highest possible multiplication factor is determined by the spectral width of the frequency comb. In other words that means the pulse width of the original signal (more general, its duty cycle) limits the multiplication factor.

Experimental setup

A hybrid electrically locked pulse laser [87] with a repetition rate of 9.953 GHz (the OC-192 clock frequency) and a pulse width of about 1 ps is used as source. Due to its duty cycle, this laser would provide a multiplication factor of up to 100. That would enable frequencies up to THz provided there is an opto-electrical conversion available. Standard single mode fiber (SMF 28) was used as dispersive element. Simulations and experiments show that the fiber dispersion slope has no significant

influence in the setup. The optical amplifier (EDFA) compensates for optical loss. The maximum frequency that can be generated is determined by the cutoff frequency of the photo diode. Figure 3.28 summarizes the setup.

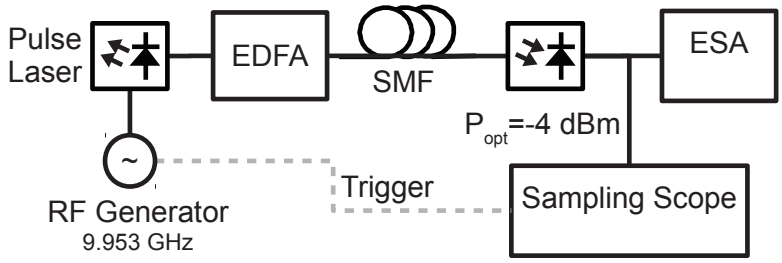

Figure 3.28: Experimental setup for RF generation using the temporal Talbot effect

The generated RF signal was analyzed by ESAs (R&S FSEK-30 up to 40 GHz, HP 8563E from 60 GHz to 90 GHz with external mixer) concerning phase noise and spectrum. For frequencies up to 50 GHz, the pulse shape could be measured with a sampling scope.

First, the time domain signals have been captured with a high-speed photodiode and the 50 GHz sampling scope. The original pulse sequence as well as the 30 GHz and 50 GHz signals are show in Figure 3.29. Filtering out the higher harmonics of the generated RF carrier by applying an electrical lowpass filter can improve the spectral purity. Due to the bandwidth limit of the sampling scope, that effect is visible in the 50 GHz signal. For the same reason, the pulse shape of the 10 GHz signal shows the pulse response of the measurement system. The 1 ps laser pulses itself can not be resolved with the scope and the photodiode. Figure 3.30 shows high-resolution spectra of the generated 60 GHz, 70 GHz, 80 GHz and 90 GHz tones.

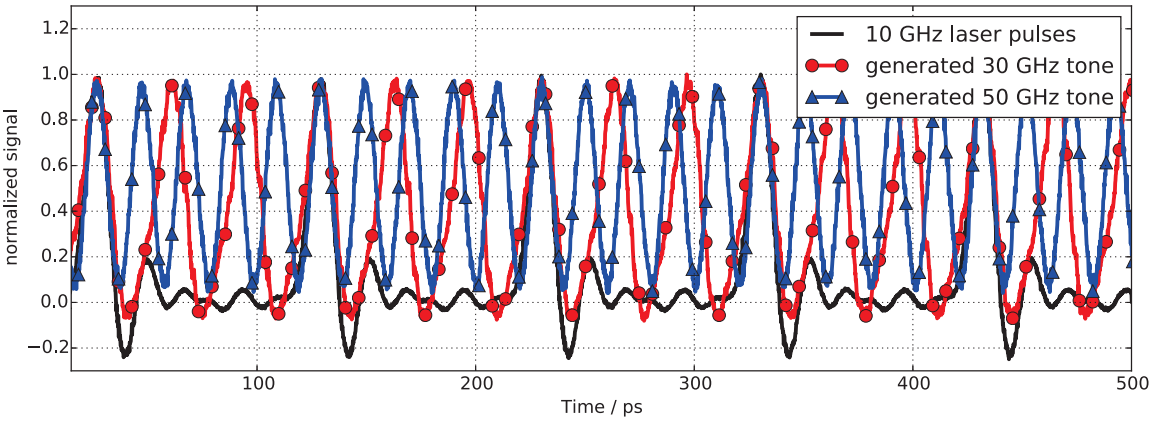

Figure 3.29: Normalized measured time domain signals for 10 GHz pulses, generated 30 GHz and 50 GHz tones (taken with a 50 GHz sampling scope)

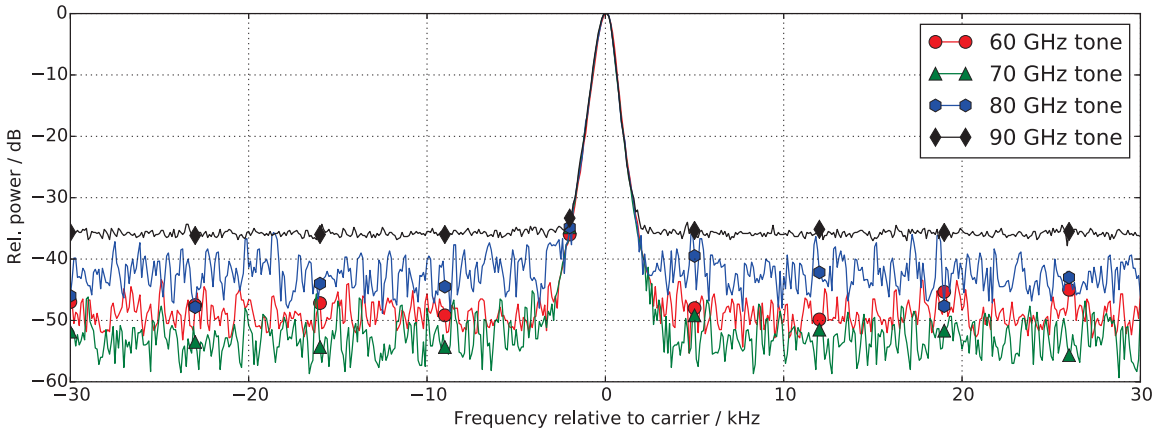

Figure 3.30: Measured spectra of generated 60 – 90 GHz tones

Table 3.8: Experimental results for 20 GHz – 90 GHz RF generation

generated frequency / GHz	**multiplication factor**	**laser wavelength / nm**	**fiber dispersion / ps/nm**	**calculated dispersion / ps/nm**
19.906	2	1525.48	646	651
28.859	3	1525.48	433	434
39.812	4	1525.48	329	325
49.765	5	1528	259	259
59.718	6	1520.44	215	218
69.671	7	1520.32	185	187
79.624	8	1511.68	166	166
89.577	9	1522.88	144	145

It was taken advantage of the dispersion slope of standard single-mode fiber to fine-tune the value for the accumulated dispersion that leads to constructive superposition for the respective frequency by adjusting the laser wavelength. The frequency-dependent dispersion behavior of the fibers has been characterized using the standardized phase shift method [58]. Table 3.8 shows the experimentally found dispersion values generating different RF carriers as well as the calculated dispersion values using equation (3.33). A good match can be observed. Especially at higher multiplication factors, the efficiency of the RF generation is very sensitive to the dispersion value.

Phase noise analysis

The phase noise has been measured for the 10 GHz RF source as well as the generated optical 10 GHz signal and the upconverted tones from 20 GHz up to 90 GHz. The

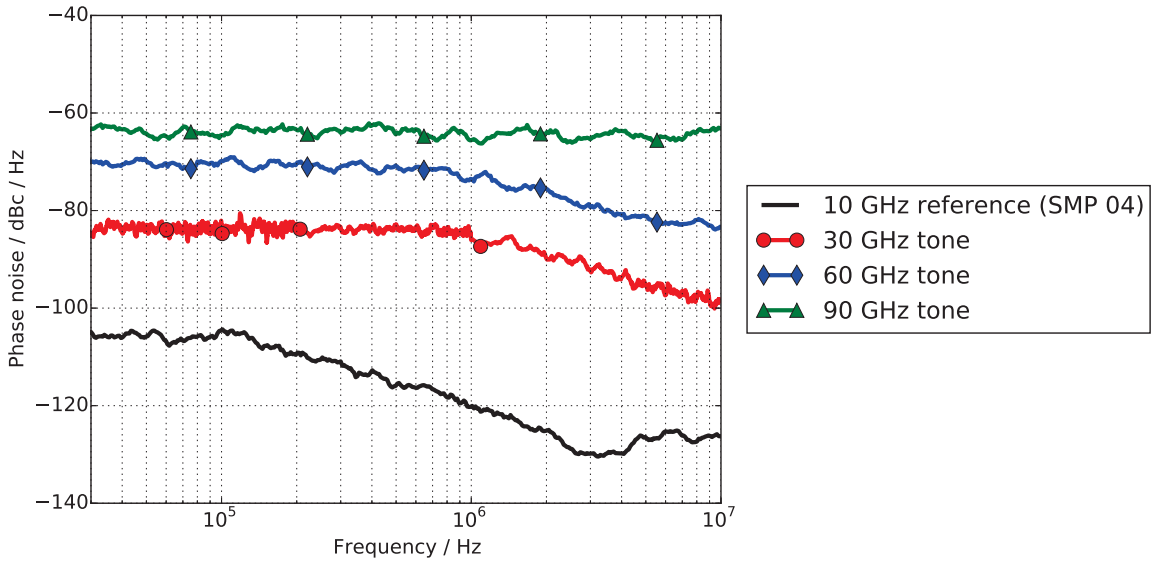

Figure 3.31: Measured phase noise for the electrical 10 GHz SMP 04 reference and the generated 30 GHz, 60 GHz and 90 GHz tones

results are shown in Figure 3.31 for the 30 GHz, 60 GHz and 90 GHz generated with a Rohde & Schwarz SMP 04 reference. Following, the phase noise contributions are analyzed in more detail. The total phase noise of the generated RF signal is influenced by three major factors:

- the phase noise of the electrical reference signal,
- the phase noise due to the laser hybrid mode locking and
- the phase noise influence of the Talbot effect.

It is clear that even perfect mode locking will never result in a better phase noise of the mode-locked laser than the one of its reference clock. The upconversion increases the phase noise and the employed Talbot effect also changes the phase noise conditions. Following, these effects will be discussed in detail.

RF source: The phase noise at the output of the transmitter is strongly influenced by the reference used. Figure 3.32 shows that dependency for the used reference source with worst phase noise properties (OC-192 clock reference of an Anritsu SDH test set, red) and the reference source with the best properties (R&S SMP 04, black) available in the lab. The solid lines indicate the phase noise of the reference source and the lines with markers show the phase noise of a 30 GHz tone (multiplication factor $m = 3$) generated with the respective source. It can be seen that the frequency behavior of the phase noise follows the one of the reference source for small carrier frequency offsets. The additional phase noise is caused by the laser source and the upconversion by means of the Talbot effect.

Mode locked laser: Mode locked lasers produce extra noise due to a variety of physical effects (e. g. quantum noise, mirror vibrations, ...) that are thoroughly

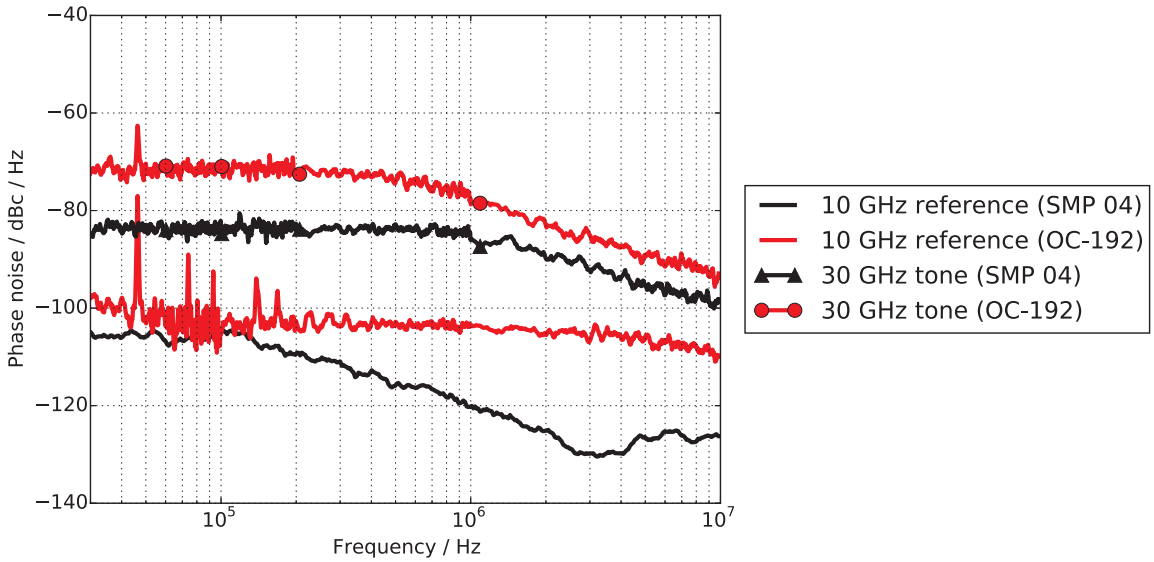

Figure 3.32: Measured phase noise for different reference sources (SMP 04, Anritsu SDH test set OC-192 clock)

discussed in [116, 117]. Here, the focus will be on the system influence. In time domain, an ideal mode locked laser produces a perfect pulse train

$$x(t) = \sum_{i=-N}^{N} x_p(t + iT_r) \tag{3.34}$$

with the repetition rate T_r, the pulse shape $x_p(t)$ and $N \to \infty$. Fourier-transforming leads to the power spectrum [147]

$$P_x(\omega) = \frac{2\pi}{T_r^2} |X_p(\omega)|^2 \sum_{i=-\infty}^{\infty} \delta(\omega - \frac{2i\pi}{T_r}) \,, \tag{3.35}$$

where $X_p(\omega)$ is the Fourier transform of the pulse shape. In [147], a detailed derivation for the mode locked laser's properties can be found. Here, the results are used and given for the reader's convenience. The noise analysis starts from the imperfect pulse train

$$x_n(t) = x(t) + \Delta x(t) \tag{3.36}$$

where $\Delta x(t)$ includes the amplitude and timing jitter fluctuations that are small compared to the ideal pulse train $x(t)$. Applying a first order Taylor series approximation for the jitter leads to the representation [147]

$$x_n(t) = x(t) + x(t)a(t) + \frac{\mathrm{d}x(t)}{\mathrm{d}t} T_r j(t) \tag{3.37}$$

where the amplitude deviations $a(t)$ and the jitter deviations $j(t)$ are separated. The jitter $j(t)$ is caused by the electrical reference and by the pulse laser itself. Autocorrelating in time-domain and taking advantage of Parseval's theorem yields the power spectrum of the noisy mode locked laser signal [147]

$$P_{xn}(\omega) = \frac{2\pi}{T_r^2}|X_p(\omega)|^2 \sum_{i=-\infty}^{\infty} \Big[\delta(\omega - \tfrac{2i\pi}{T_r}) + P_a(\omega - \tfrac{2i\pi}{T_r}) + (2i\pi)^2 P_j(\omega - \tfrac{2i\pi}{T_r})\Big] \ . \tag{3.38}$$

In this equation, different bands for the different harmonics i can be seen with the amplitude noise contribution P_a and the noise contribution due to timing jitter P_j. Introducing $\omega_i = \omega - \frac{2i\pi}{T_r}$ for the i$^{\text{th}}$ harmonic, the spectrum for the band can be written as

$$P_{xi}(\omega_i) = \frac{2\pi}{T_r^2}|X_p(\omega)|^2 \left[\delta(\omega_i) + P_a(\omega_i) + (2i\pi)^2 P_j(\omega_i)\right] \ . \tag{3.39}$$

The phase noise of this band centered at the harmonic $\omega_{i,0}$ is defined as

$$L_i(\omega_i) = \frac{P_{xi}(\omega_i)}{P_{xi}(\omega_{i,0})} \ . \tag{3.40}$$

The amplitude noise spectrum $P_a(\omega_i)$ and the jitter spectrum $P_j(\omega_i)$ do not depend on the harmonic i. Following the definition, the noise contributions are zero at the carrier frequency $\omega_{i,0}$ and the delta function equals one. Therefore, the phase noise at a fixed frequency $\omega_i = \omega_{i,0} + \Delta\omega_i$ is

$$L_i(\omega_i = \omega_{i,0} + \Delta\omega_i) = P_a(\omega_i) + (2i\pi)^2 P_j(\omega_i) \ . \tag{3.41}$$

This phase noise can be rewritten in a more general way using the constants C_a (amplitude contribution) and C_j (jitter contribution)

$$L_i = C_a + i^2 C_j \ . \tag{3.42}$$

For RF upconversion, the higher harmonics ($i > 1$) in the spectrum of the mode-locked laser are used. The phase noise degradation at higher harmonics with respect to the fundamental ($i = 1$) is

$$\Delta L_i/\mathrm{dB} = 10\log_{10}\left(\frac{1 + i^2\frac{C_j}{C_a}}{1 + \frac{C_j}{C_a}}\right) \ . \tag{3.43}$$

For dominating amplitude jitter $\frac{C_j}{C_a} \to 0$, no phase noise degradation will be seen ($\Delta L_i = 0\ \mathrm{dB}$). Hence, the critical case is dominating phase jitter $\frac{C_j}{C_a} \to \infty$. There, the linear phase noise degradation is

$$\lim_{\frac{C_j}{C_a}\to\infty} \frac{1 + i^2\frac{C_j}{C_a}}{1 + \frac{C_j}{C_a}} = i^2 \tag{3.44}$$

and in dB

$$\Delta L_i/\mathrm{dB} = 20\log_{10}(i)\ . \tag{3.45}$$

It is worth mentioning that this result is identical to the case of conventional electrical upconversion.

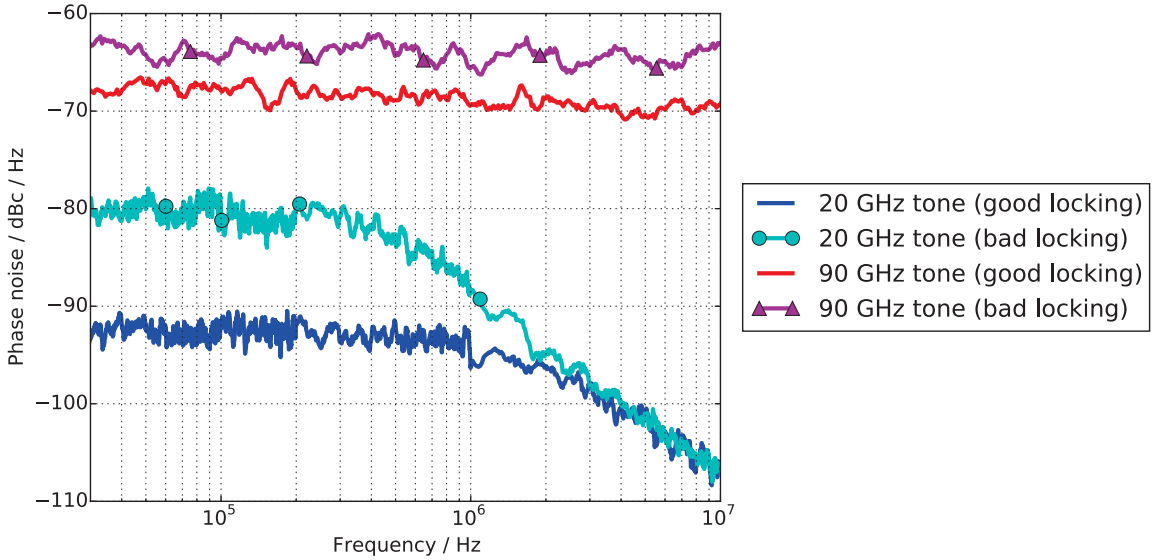

Figure 3.33: Influence of good and bad locking on phase noise

One of the major contributions to the pulse laser's extra phase noise in the investigated setup was the imperfect mode-locking of the pulse laser. Furthermore, a necessary fine-tuning of the mode-locked laser leads to different size of this extra phase noise. The laser wavelength was tuned to exactly match the corresponding Talbot dispersion (equation (3.33)) taking advantage of the dispersion slope of the fiber. The repetition rate of the laser was tuned to ensure proper locking on the reference source. During adjustment of the laser, the quality of the generated RF tone was monitored by evaluating the spectrum on the ESA. Being more sensitive to imperfect settings (dispersion and repetition rate) it was easier to achieve a constant good locking for higher generated frequencies. Figure 3.33 shows measurements under good and bad locking conditions for the minimal frequency generated (20 GHz, multiplication factor $m = 2$) and the maximum achieved frequency of 90 GHz (multiplication factor $m = 9$). It can be seen that the phase noise uncertainty decreases with increasing frequency due to higher sensitivity to imperfect settings.

Talbot effect

It has been shown that the temporal Talbot effect has further influence on the phase noise [45, 46]. The output RMS noise after the Talbot effect σ_o depending on the input noise σ_i is [119]

$$\sigma_o = \sigma_i \sqrt{m \sum_{p=-\infty}^{\infty} \left| \frac{T_0}{\sqrt{T_0^2 - \mathrm{j} T_r^2 \frac{s}{2\pi m}}} \mathrm{e}^{-\frac{p^2 T_r^2}{2(T_0^2 - \mathrm{j} T_r^2 \frac{s}{2\pi m})}} \right|^2} \tag{3.46}$$

where the temporal Talbot effect is characterized by its parameters: $\frac{s}{m}$ is the fraction of the Talbot length, T_r is the pulse repetition rate and T_0 is the 1/e-width of the input pulse which is linked to the more common full-width-half-maximum (FWHM) definition of the pulse width $T_{0,FWHM}$ as follows

$$T_0 = \frac{T_{0,\mathrm{FWHM}}}{\sqrt{2 \ln 2}} \ . \tag{3.47}$$

For frequency upconversion applications, m is the multiplication factor and $s = 1$. The duty cycle

$$d = \frac{T_0}{T_r} = \frac{T_{0,\mathrm{FWHM}}}{\sqrt{2 \ln 2} T_r} = \frac{d_{\mathrm{FWHM}}}{\sqrt{2 \ln 2}} \tag{3.48}$$

may be introduced. This duty cycle d is related to the the duty cycle d_{FWHM} using the FWHM definition instead of the 1/e definition. Furthermore, the RMS noise relation $r = \frac{\sigma_o}{\sigma_i}$ deduced from (3.46) between the noise of the input and the output pulses will be analyzed

$$r = \sqrt{m \sum_{p=-\infty}^{\infty} \left| \frac{\mathrm{e}^{-\frac{p^2}{2(d^2 - \frac{\mathrm{j}}{2\pi m})}}}{\sqrt{1 - \frac{\mathrm{j}}{2\pi m d^2}}} \right|^2} \ . \tag{3.49}$$

This noise relation is a measure how the input noise is decreased (by averaging) ($r < 1$) or increased ($r > 1$) by the temporal Talbot effect. Depending on the multiplication factor, Figure 3.34 shows the duty cycle required from the pulse laser source to maintain the RMS noise level ($r = 1$, black line). Lower duty cycles (the green area under the black curve) yields a phase noise improvement due to the Talbot effect. On the other hand, a bigger duty cycle results in a phase noise deterioration. For high multiplication factors, low duty cycles are required for low phase noise. The maximum duty cycle for the corresponding multiplication factor is given. An even higher duty cycle of the pulse laser source prevents the wanted frequency from being generated (red area). In time domain, this means overlapping pulses.

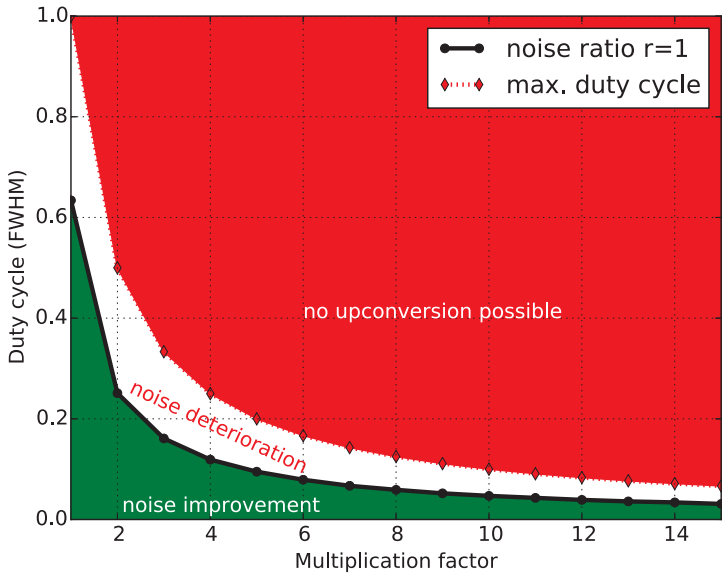

Figure 3.34: Total phase noise change compared to electrical upconversion for Talbot effect with different duty cycles and without Talbot effect

Total phase noise

The reference source and the pulse laser create noise in the optical pulses before applying the temporal Talbot effect in dispersive media ($L(f)$). Depending on the characteristics of the Talbot effect (duty cycle, multiplication factor), this noise is influenced by the Talbot upconversion. The total RMS noise can be calculated from the phase noise as follows [122]

$$\sigma^2 = \frac{2T^2}{\pi^2} \int_0^{f_{max}} L(f)\mathrm{d}f \tag{3.50}$$

where T is the period of the signal and f_{max} is the maximum frequency offset from the carrier. Taking into account that the time domain jitter σ changes by the factor r when applying the multiplication factor m and assuming that the noise characteristics (i.e. the shape of $L(f)$) stays constant, the noise of the upconverted tone is

$$r^2\sigma^2 = \frac{2T^2}{\pi^2 m^2} \int_0^{f_{max}} m^2 r^2 L(f)\mathrm{d}f \ . \tag{3.51}$$

The resulting phase noise is scaled by the factor of r^2, or in dB by $20\log_{10} r$. However, for the multiplication factor m, the period of the upconverted signal $T' = \frac{T}{m}$ scales with $\frac{1}{m}$ which also has to be taken into account for the phase noise of the upconverted

signal $L'(f) = m^2 r^2 L(f)$. The phase noise change in dB can be computed regarding both of the effects

$$\Delta L(f)/\mathrm{dB} = 20 \log_{10} r + 20 \log_{10} m \; . \tag{3.52}$$

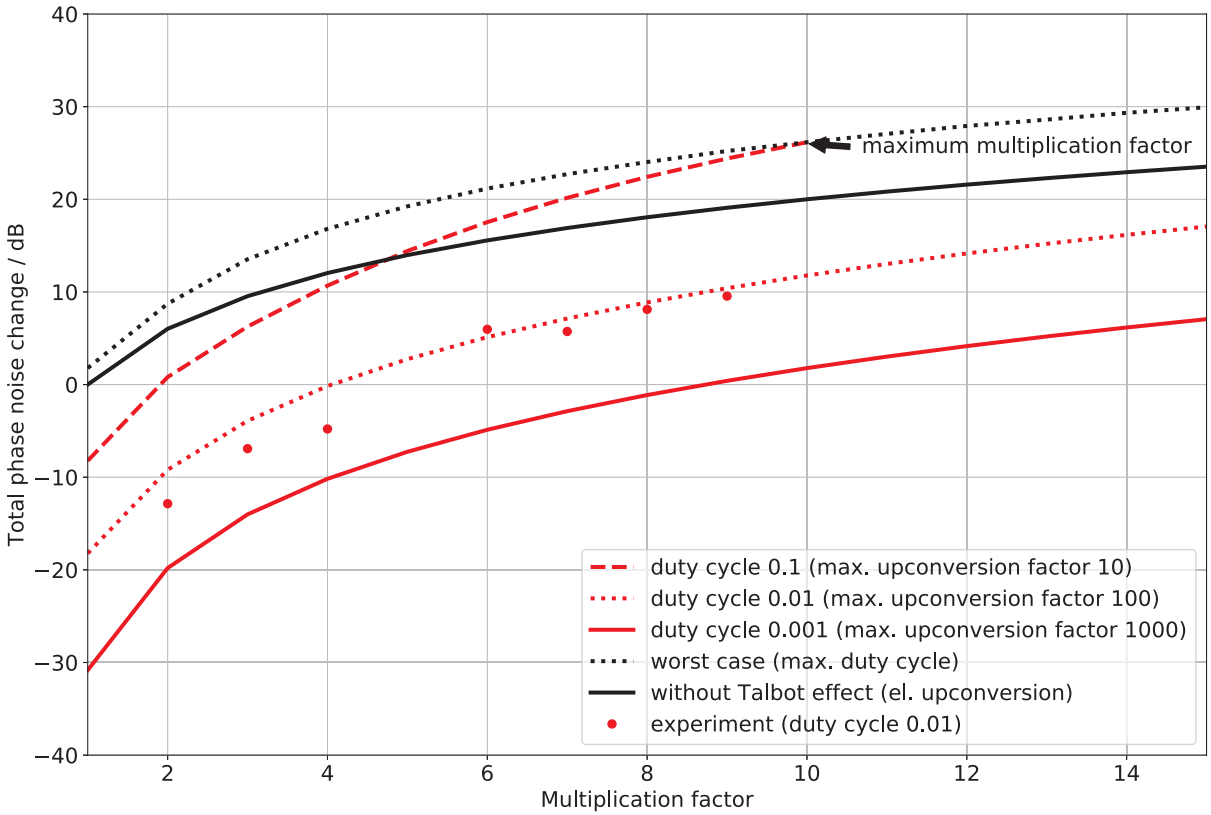

Figure 3.35: Calculated total phase noise change for Talbot effect with different duty cycles, experimental values and calculated phase noise change for electrical upconversion

Figure 3.35 shows the phase noise change (improvement or degradation, see equation (3.52)) of the laser pulses due to the Talbot effect RF generation for different duty cycles with respect to the multiplication factor. Classical electrical upconversion is equivalent to the case of no influence by the Talbot effect ($r = 1$). It can be seen that the duty cycle of the optical pulses should be as low as possible to achieve good phase noise conditions. However, for low duty cycles (i. e. short pulses) the spectrum of the comb laser source broadens. Using optical fibers as dispersive medium this may lead to situations where higher order dispersion may not be neglected and may affect the system performance [7].

Additionally, the measured total phase noise change at a 100 kHz frequency offset from the carrier with respect to the multiplication factor is plotted (red dots) for the pulse laser source that was used in the experiments (duty cycle $d_{\mathrm{FWHM}} = 0.01$). A very good match between these values and the theoretical prediction can be observed.

Laser mode locking and other effects lead to additional phase noise. As stated earlier, the measurement values depend strongly on the quality of laser mode locking where the deviations are bigger for smaller frequencies.

Efficiency improvement

Laser sources with a low duty cycle (which is favorable in terms of phase noise performance) have a broad spectrum due to the small pulse widths. In these broad combs, a large number of neighboring lines may mix and therefore contribute to the electrical output signal. However, this situation only exists when the dispersion matches in all parts of the spectrum according to equation (3.33). That means, standard single-mode fibers or typical fiber Bragg gratings with constant dispersion do not provide the best performance when used as dispersive element. For higher (λ_H) and lower (λ_L) wavelengths than the design wavelength λ_0, a delay mismatch occurs and not the full power of the comb can be used to generate the electrical signal at the photodiode. Consequently, an arbitrary dispersive element has to be designed that matches the required dispersion characteristic over the full spectral range of the comb [101].

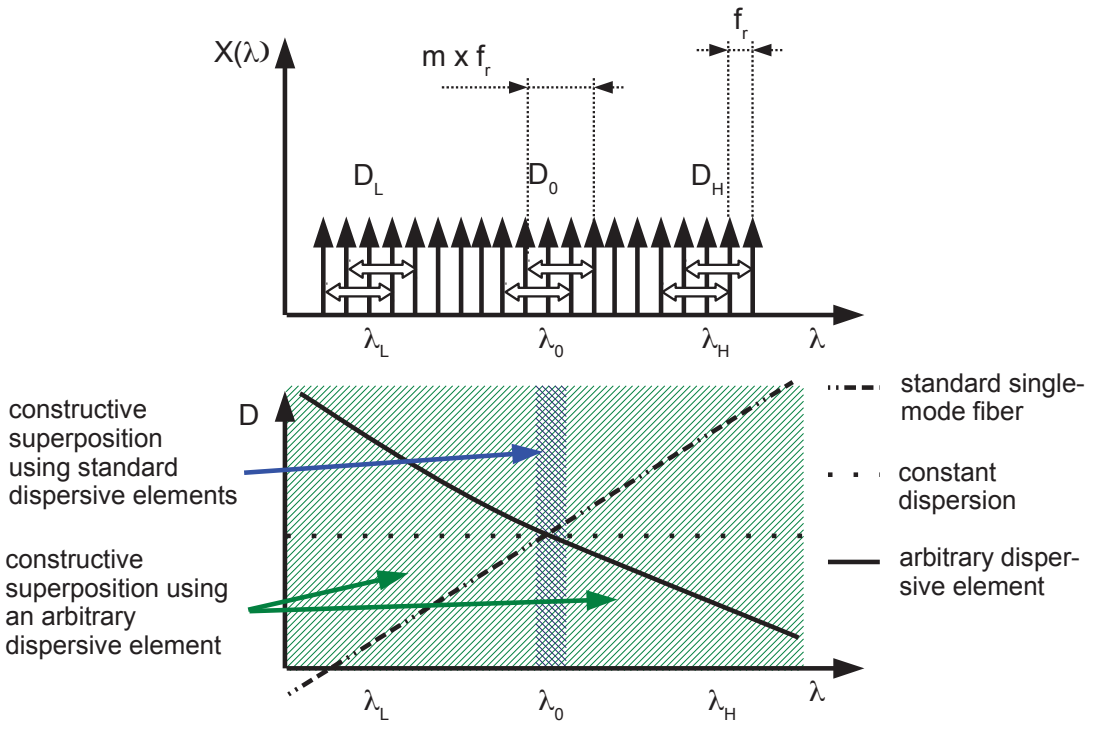

Figure 3.36: Principle of Talbot effect supported millimeter wave generation and efficiency improvement due to an arbitrary dispersive element

The upper part of Figure 3.36 illustrates the mechanism of the frequency multiplication. The pulsed source has a repetition frequency of f_r that appears in the spectrum. In this schematic picture, the multiplication factor is $m = 3$, i.e. hetero-

dyning of lines with a spectral distance of $3f_r$ leads to a constructive interference in electrical domain producing a RF tone with $3f_r$.

In the lower part, the efficiency improvement technique is explained: While for standard fiber and fiber Bragg gratings the required dispersion is only produced around λ_0, the arbitrary dispersive element provides the necessary frequency-dependent value D_L for low wavelengths λ_L, D_0 for the center wavelength λ_0 and D_H for higher wavelengths λ_H. That way, constructive interference is enabled over the full spectral width of the source.

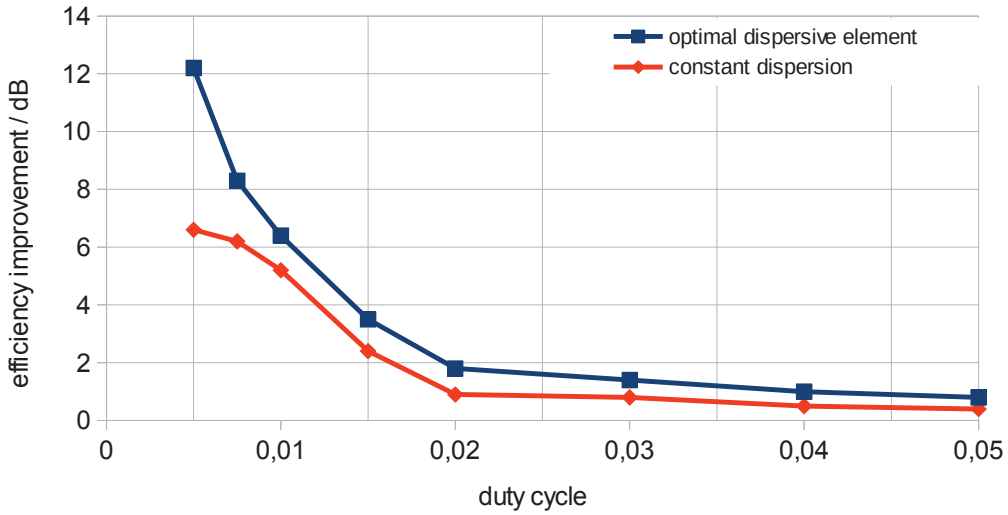

Figure 3.37: Efficiency enhancement compared to standard singlemode fiber for a four fold multiplication of a 10 GHz reference signal depending on the duty cycle of the pulse train

VPItransmissionMaker has been used to simulate the frequency multiplication setup (see Figure 3.28). A four-fold frequency multiplication of a pulse train with 10 GHz repetition frequency has been implemented. The spectral width of the source has been changed by varying the duty cycle of the pulses from 0.005 (0.5 ps pulse width at 10 GHz repetition frequency) to 0.05 (5 ps pulse width). The power of the generated 40 GHz component has been observed after the photodiode using a RF bandpass. Figure 3.37 shows the efficiency increase that can be achieved compared to a standard single mode fiber with a constant dispersion (red line) and with an optimal dispersion characteristic (blue). For the smallest duty cycle that has been simulated, the generated RF tone is more than 10 dB stronger than with standard single mode fiber and more than 6 dB stronger than with constant dispersion. For even lower duty cycles (i.e. smaller pulses), that effect grows. With increasing duty cycle, the spectral width of the source narrows and the difference becomes smaller. Anyway, this is not the beneficial use case where the phase noise can be improved. Additionally, reaching towards Terahertz frequencies requires broad combs and high multiplication factors implying sources with low duty cycles.

Conclusion

The temporal Talbot effect can be used to generate RF tones at high frequencies. The phase noise properties of microwave generation have been analyzed and experimentally verified. All parts of the system (reference source, mode-locked laser and Talbot effect) have been modeled. The results could be confirmed by measurements of generated RF tones up to 90 GHz. A comprehensive description employing the influence of all parts of the system has been developed. These results match very well with the measurements.

As a consequence, important directions for the design of a microwave source by means of Talbot effect can be given. Like for conventional systems, the properties of the reference source is of great importance. Using a mode-locked laser, good locking ensures low additional phase noise penalty. The smaller the duty cycle of the laser pulses is (i.e. short pulses) the higher is the possible multiplication factor and therefore the higher are the frequencies that can be generated. Finally, it can be taken advantage of the jitter smoothing quality of the Talbot effect. For low duty cycles, a reduction of phase noise can be achieved. The shorter the laser pulses are the higher is the reduction. Hence, for higher multiplication factors, the noise reduction effect decreases. That means, a laser source with short pulses and low jitter is advantageous for millimeter wave signals with low phase noise.

However, short pulses imply a broad comb in frequency domain. This sets special demands to the dispersive element to ensure high efficiency when generating the RF tone. It has been shown that an arbitrary dispersive element with optimal properties can significantly improve the efficiency.

In summary, generating microwave frequencies using the Talbot effect is an easy and potentially cost-effective method that is capable of providing signals with low phase noise (even lower compared to electrical upconversion). Numerous applications such as Radio-over-Fiber and radar can benefit from such a signal source. An integration on board-level or even as photonic circuit (when compact dispersive elements are available) is expected to reduce environmental influences (e.g. temperature and vibration).

3.3 System level applications

Extending microwave photonic solutions to kilometer ranges and adding complexity leads to system level applications. In these use cases, sub-systems mentioned in the previous chapters are included. This elaborate degree of sophistication enables smart systems with comprehensive functionality.

The first example is given in chapter 3.3.1 where Radio-over-Fiber systems help to facilitate the deployment of broadband wireless data at high carrier frequencies around 60 GHz. Two system approaches – RF-over-Fiber and IF-over-Fiber – are considered and discussed.

Fiber-to-the-antenna (chapter 3.3.2) systems based on the fiber-coupled Rx and Tx antennas introduced before (see 3.2.1 and 3.2.2) plus a central station extend the

Radio-over-Fiber concept by shifting the conversion between optical and electrical domain to the antenna element. This drastically simplifies and miniaturizes the base stations and is therefore a very interesting option for future systems. The examplary realization exhibits an outstanding performance in terms of transmission length and data rate for the given carrier frequency.

Radio-over-Fiber approaches can also be combined with optical sensors allowing them to be interrogated wirelessly. This paves the way for a multitude of new applications where optical sensors have not been possible before. As an example, the case of accessing optical temperature sensor data directly via radio signals is pointed out in chapter 3.3.3.

3.3.1 Radio-over-Fiber systems

Wireless systems – cellular ones as well as wireless LAN – have shown a tremendous growth in user number, data rate and, consequently, aggregated data rate. The rise of more and more multimedia (HD and 3D video, streaming, etc.) contents is going on. Therefore high performance and at the same time low-cost wireless systems are needed. While optical communication is omnipresent and unavoidable for the backbone and wireless communication becomes more and more powerful, one crucial task is to connect the end points of the wireless transmission efficiently with the backbone network.

Increasing the wireless carrier frequency provides a more broadband air interface. Furthermore, higher wireless carrier frequencies mean more free space attenuation resulting in less range. This leads to more base stations which are in closer vicinity to each other because the covered area of a single base station decreases. If less mobile units are served, the available data rate per mobile unit increases additionally. The drastically increasing number of base stations can only be connected efficiently to the backbone when they are far less complex than today. That means, data processing, frequency generation and other tasks that need costly equipment have to be shifted to a central station where these subsystems can be shared among different base stations. Moreover, the environmental requirements (e.g. climate control) for the base stations can be relaxed when they just consist of comparably simple hardware. This allows the design of cheap and lightweight units that can be easily deployed.

A typical RoF system is shown in Figure 3.38. In the central station (CS), the electrical carrier is generated and the baseband data is processed before transmitting and after receiving. Over optical waveguides (typically single-mode fibers), the Radio-over-Fiber signal is transported to base stations (BS) where after an opto-electrical conversion the wireless signal is transmitted to the mobile station (MS). In the uplink case, the BS receives the wireless signal from the MS, converts it to optical domain and forwards it to the CS. In any case, the BS will not carry out any signal processing. Therefore, sometimes it is also referred to as remote antenna unit (RAU) or remote radio head (RRH).

Radio-over-Fiber systems can be classified depending on the nature of the transmitted electrical carrier. If the carrier can be radiated by the base station directly

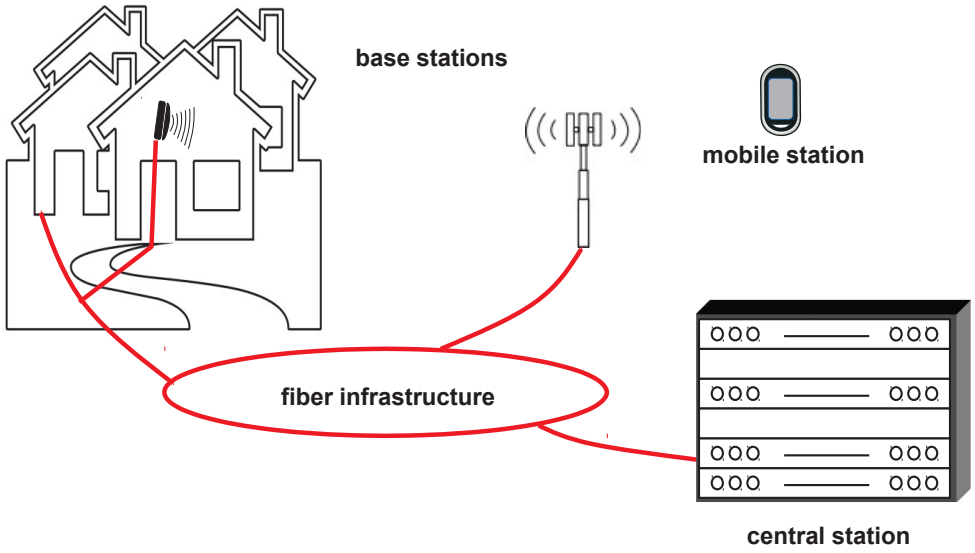

Figure 3.38: Radio-over-Fiber system consisting of central station (CS), base stations (BS) and mobile stations (MS)

after reception in a photodiode, this scheme is known as RF-over-Fiber. If an up-conversion is necessary, the approach is named IF-over-Fiber. Other concepts work with transmission of digital baseband data which still requires a complex base station. These systems are not targetted here.

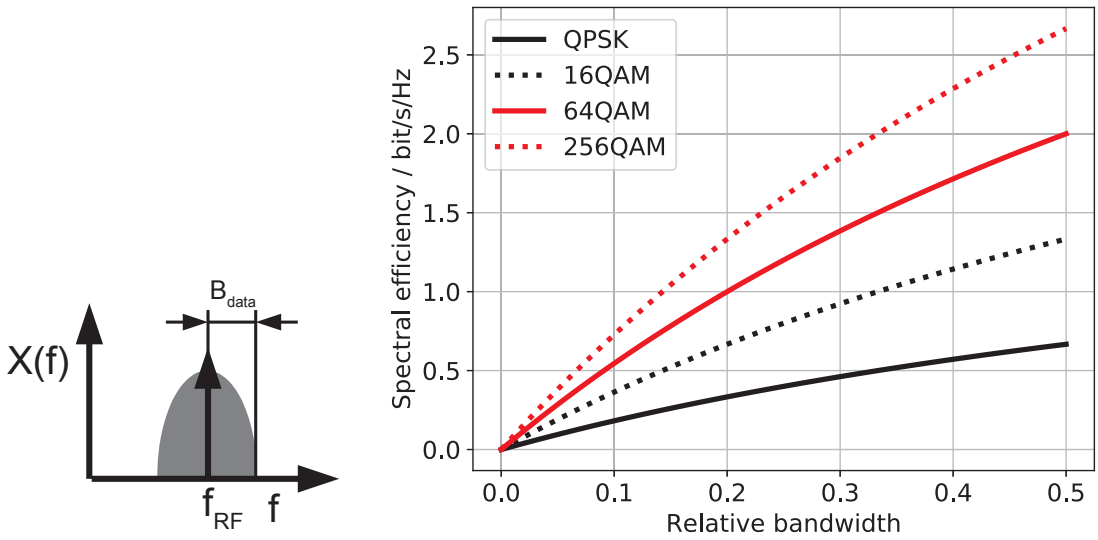

Figure 3.39: Spectral efficiency of RoF system with respect to relative bandwidth

RF-over-Fiber enables the simplest base stations because just a photodiode, possibly a power amplifier and an antenna are needed for the downlink. As a drawback, high-end photodiodes are needed for high carrier frequencies (e.g. 60 GHz and above) and signal impairments (e.g. chromatic dispersion) have a stronger effect and scale

with the RF carrier frequency. These degradations are discussed in more detail later in this chapter. Additionally, the spectral efficiency in the optical part is comparably low because of the large unused portion of the spectrum between optical carrier and modulated signal. For a given modulation format, it does not depend on the carrier frequency when the relative bandwidth (ratio of baseband data signal bandwidth to RF carrier frequency $\frac{B_{\mathrm{data}}}{f_{\mathrm{RF}}}$) remains constant. The relative bandwidth cannot exceed 0.5 for RoF systems, otherwise there would be interference with the baseband component of the received signal after the photodiode. Figure 3.39 shows the dependency of the spectral efficiency of RoF systems with respect to the relative bandwidth.

On the other hand, IF-over-Fiber systems avoid these drawbacks at the cost of a slightly more complex base station. Using an IF carrier at a rather low frequency (e.g. 10 GHz) eases the mentioned issues with signal impairments and spectral efficiency. However, at the base station, the received optical signal has to be upconverted. A mixer and corresponding drivers are needed. Generating the RF carrier on-site may be simplified by transmitting a reference tone that will be upconverted as well. However, a base station consisting of tens of ICs instead of just two or three increases the cost and power consumption of this unit.

RF-over-Fiber

For RF-over-Fiber systems with wireless carriers in the gigahertz range, optical generation of the carrier is advantageous. In [5], different approaches to generate RF carriers by optical means are discussed. Out of the variety of options – remote heterodyning, direct or external modulation, lasers providing multiple lines and many more – for the exemplary 60 GHz RF-over-Fiber system presented here an external optical double sideband modulation scheme with suppressed carrier (ODSB-SC) has been chosen. This setup requires only a 30 GHz input signal and therefore minimizes the electrical bandwidth of the MZM due to frequency doubling in optical domain. Measurements of the phase noise of the generated 60 GHz tone have been carried out to assess different possible setups with and without fiber Bragg grating for residual carrier suppression as well as with and without optical amplifier [5].

When using optical generation for the wireless carriers, IQ modulation is needed in a subsequent stage in order to provide complex modulation formats, e.g. QPSK. The bandwidth of such modulators may be much smaller because they operate in baseband and take the I and Q signals as input. For the 60 GHz systems aimed at, the whole wireless band covers less than 10 GHz so that this RF bandwidth is sufficient for the data modulators. A modulation scheme with with data on both generated lines with 60 GHz spectral distance has some disadvantages with respect to performance, like bit walk-off as discussed in depth later in this chapter. Separating the two tones and only modulating one of them (optical single-sideband) is possible with an optical filter.

The complete carrier generation and data modulation chain is shown in Figure 3.40. A laser source, typically a DFB laser diode, is externally modulated with the electrical carrier frequency. By biasing the Mach-Zehnder modulator (MZM) in its minimum

point, frequency doubling in the optical domain lowers the requirements on the RF bandwidth of the external modulator, its driver amplifier and the electrical signal generator. The generated two-tone signal with 60 GHz spectral distance between the components is fed into the IQ data modulator. In order to realize single sideband (SSB) modulation, the two tones have to be separated. A Mach-Zehnder interferometer (MZI) with 120 GHz spectral range can be tuned in a way that the minimum of the first output port is centered on the first line and, at the same time, the maximum of the first output is tuned to the second spectral line. Due to the properties of MZIs, the behavior is reversed for the second output: The first tone is transmitted and the second tone is suppressed. A suppression of more than 20 dB between the sidebands has been achieved [2]. Compared to other filters, only a small portion of the signal power is absorbed. This provides a very energy-efficient solution (the MZI realized in fiber optics has only around 1 dB insertion loss). While the one spectral component is modulated by an optical IQ-modulator (dual parallel MZM), the other one remains unmodulated. The amplitude of the unmodulated tone as well as its polarization is adjusted ensuring the wanted signal shape after recombination. Splitting the two tones and recombining them with a 3 dB coupler would form a parasitic MZI when the path lengths are unequal. Therefore, an optical delay line is added in one path to ensure equal lengths. This prevents from unwanted wavelength dependency of the modulation part. The output of the 3 dB coupler is ready to be amplified and fed into the fiber span. The input polarizations to all modulators have to be tuned to avoid high insertion loss. Additionally, the polarization has to be adjusted between the two paths in the IQ data modulation stage for efficient combining in the 3 dB output coupler.

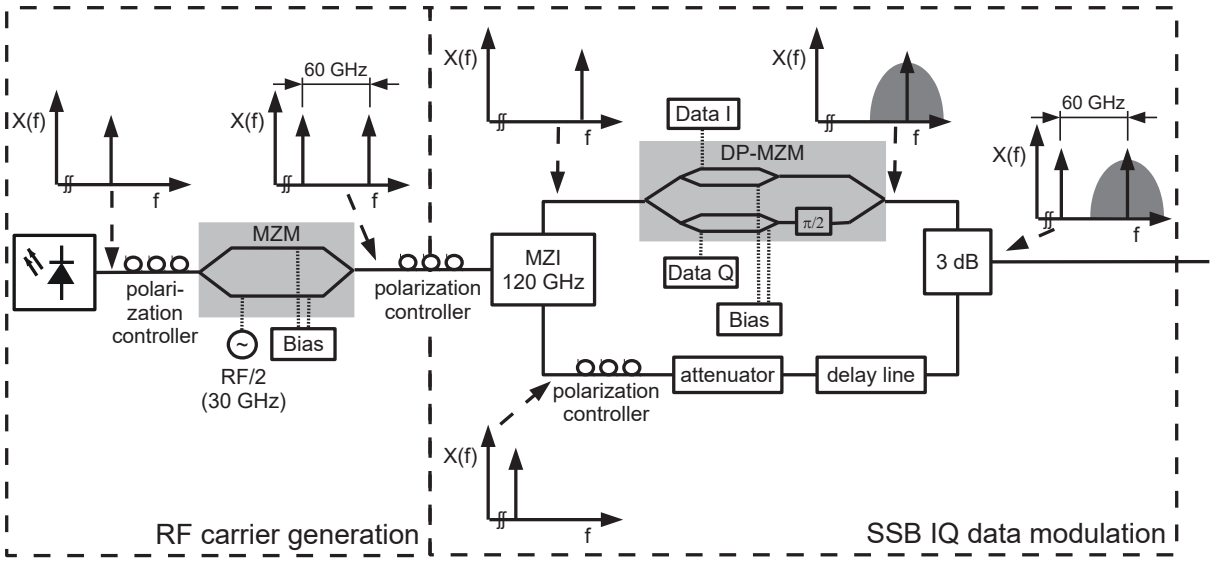

Figure 3.40: Carrier generation and IQ data modulation in central station of RF-over-Fiber systems

The base station of RF-over-Fiber systems is quite simple: After converting the optical signal to electrical domain, it may be directly radiated. The bandwidth of the photodiode is the bottleneck for the possible RF frequencies: It should at least allow for the RF carrier frequency plus the spectral width of the baseband data ($f_{\mathrm{RF}} + B_{\mathrm{data}}$).

The use of IQ modulation allows the use of advanced modulation formats with higher spectral efficiency such as QPSK [3]. At the mobile station, a free-running local oscillator in conjunction with digital signal processing may be used for carrier and data recovery [2, 4, 6].

IF-over-Fiber

As mentioned before, another option are IF-over-Fiber systems. Transmitting an IF carrier modulated with the data and upconverting it to RF at the base station results in more effort for the electronics. A detailed discussion may be found in [35, 36]. However, the lower IF carrier frequency enables a higher spectral efficiency. Another advantage is the smaller susceptibility to dispersive effects in optical domain and other signal impairments.

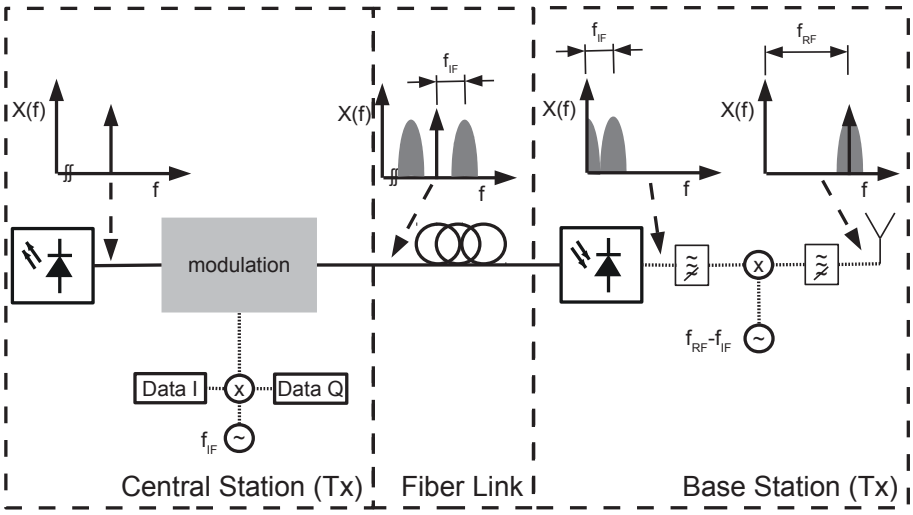

Figure 3.41: IF-over-Fiber central station and base station (transmitter part)

Figure 3.41 depicts a block diagram of the transmitter chain of an IF-over-Fiber system. In the central station, the data is electrically modulated on the IF carrier using an IQ modulator. To ensure high spectral efficiency and to enable the use of components (e.g. optoelectronics) with low RF bandwidth, the IF carrier frequency f_{IF} should be chosen as small as possible. However, for a given baseband data bandwidth B_{data}, it should be at least $2B_{\mathrm{data}}$ to avoid aliasing after direct detection. Moreover, higher IF frequencies have a smaller relative bandwidth ($\frac{B_{\mathrm{data}}}{f_{\mathrm{IF}}}$) which means that components are typically easier to realize. Chosing $f_{\mathrm{IF}} = 10\ \mathrm{GHz}$ is a good compromise and allows for passband data bandwidths of up to 7 GHz including

some guard band. The data on the IF carrier can be amplitude modulated on the laser source using either direct modulation or a simple external amplitude modulator. The RF bandwidth of the electrooptical conversion should be at least $B_{\mathrm{RF}} = f_{\mathrm{IF}} + B_{\mathrm{data}}$. Compared to the RF-over-Fiber solution this is even less than required for the optical RF carrier generation.

Also the photodiode converting the IF-over-Fiber signal back to electrical domain needs less bandwidth ($f_{\mathrm{IF}} + B_{\mathrm{data}}$ instead of $f_{\mathrm{RF}} + B_{\mathrm{data}}$). However, the signal cannot be radiated directly but has to be upconverted. The RF carrier is produced by mixing the IF signal (the baseband components created by the photodiode have to be filtered out) with a locally generated tone. It is worth mentioning that this tone can be formed by upconverting a reference signal that is also transmitted over the same fiber. After filtering the images caused by the mixer the RF signal can be wirelessly transmitted.

Signal impairments

The impairments of the optical channel affect Radio-over-Fiber signals in different ways. Nonlinear effects (e.g. self-phase mixing) and linear distortions (mainly chromatic dispersion) may cause signal outages.

For optical baseband transmission, chromatic dispersion leads to inter-symbol interference within the data. For RoF signals, the dispersion-induced phase shift between the data and the carrier induces additional power fading. Moreover, in the case of DSB modulation, the phase shift between upper and lower sideband results in overlapping eye diagrams after reception in the mobile station known as bit-walkoff effect. All the dispersive effects become stronger with increasing electrical carrier frequency. That means, for RF-over-Fiber systems an equalization to ensure low bit-error rates is needed at much shorter distances than for IF-over-Fiber systems. Polarization mode dispersion causes similar symptoms as chromatic dispersion: The mismatch between carrier and data polarization produces power fading. The varying propagation speed of different polarizations is the reason for inter-symbol interference. However, usually the effects originating in chromatic dispersion are dominating.

A RoF system is not a classical optical single carrier system (even if only one channel is used) because of the RF carrier. Provided that sufficiently high powers are transmitted, there may not just be self-phase modulation affecting the data but also cross-phase modulation between carrier and data. A nonlinear phase shift between carrier and data manifests itself the same way as the dispersive effects described above. Four-wave mixing may produce new frequency components in-band and out-of-band. Transfering the power from the signal to other frequencies leads to a power penalty. In-band frequency components additionally lead to interference.

Signal processing can be used to equalize the effects introduced by the optical channel. Algorithms known from classical optical communication as well as from wireless links can be adapted and re-used [2].

3.3.2 FTTA system

Radio-over-Fiber systems as described in the previous section can be evolved in terms of electro-optical convergence to Fiber-to-the-Antenna (FTTA) setups. The major building blocks for FTTA systems are fiber-coupled Rx and Tx antennas as described in chapter 3.2.1 and 3.2.2. A fiber network connects the antennas with the central station (CS) of the RoF system that may be located kilometers away from the antenna site.

Several FTTA systems have been realized in the past. The high bandwidth needed for the ultra-wideband radio technology (UWB) calls for the use of FTTA techniques. In the UWB over Fiber system presented in [114], a fiber-coupled remote Tx antenna was realized (i.e. no back channel was available). Combining a commercial antenna with the optical receiver only led to a low degree of integration comparable with the system in [76]. Horn antennas provide high gain and have been used in some full-duplex systems with externally connected optical receivers [140]. Complete full-duplex systems have rarely been accomplished. Some of them have only been measured without wireless link (i.e. without antennas) [43]. Others are limited to only MHz bandwidth [88] for IEEE 802.11b/g Wireless LAN support. In general, migrating to higher frequencies pushes towards higher integration because of the high losses of even short electrical waveguides [27].

Therefore, designing a broadband full-duplex FTTA system is a challenge. An example system and its design are presented here. The building blocks, Tx and Rx antennas integrated on PCB, have already been introduced in sections 3.2.1 and 3.2.2. Now, the focus is on the system setup (including base station) and demonstrating the system performance [107].

Setup

With the available building blocks, a system with a high relative antenna bandwidth of 133% (corresponding to a relative baseband bandwidth of 67%) could be set up. That means, a certain level of interference between the received baseband signal and the received RF signal at the photodiode of the Tx antenna is tolerated. Covering the frequencies from 500 MHz to 2.5 GHz enables the parallel broadcasting of numerous existing standards. The transparent transport over the fiber ensures the compatibility to existing mobile devices. For the system demonstration, just one broadband signal will be modulated on a 1.5 GHz carrier. In metro networks, tens of kilometers may have to be traversed between the central station and the fiber-coupled antennas. In the experiment, fiber spools up to tens of kilometer length have been used. The wireless transmission distance is limited by the available Tx power of only some mW to only a few meters. Figure 3.42 summarizes the general setup of the RoF FTTA system.

The wireless signal is generated in the CS by modulating the data on an electrical carrier. Modulation format, carrier frequency and other specifications depend on the wireless standard. Being modulated on an optical carrier, this signal can be

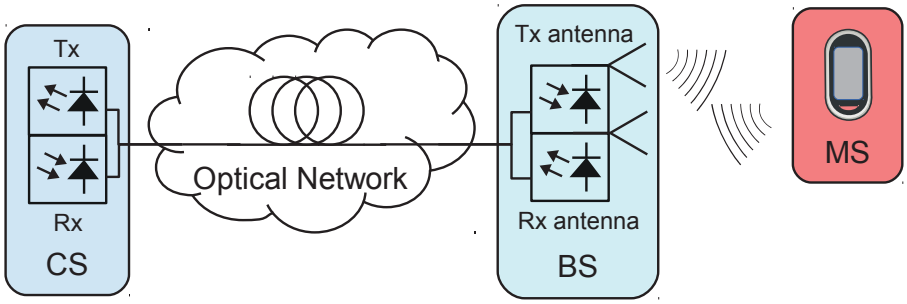

Figure 3.42: RoF / FTTA system with Central Station (CS), Optical Fiber Network, Base Station (BS) including fiber-coupled Rx antenna and Mobile Station (MS)

transported over existing fiber infrastructure. For cost and performance reasons, a directly modulated DFB laser diode is used as optical source (see chapter 2.1). Known as RF-over-Fiber scheme, this approach leads to the most simple BS configuration. The uplink from the MS is also transported over optical fiber. Photodetectors at the CS convert the RoF signal back to electrical domain. The resulting electrical signal can be demodulated to retrieve the data which is further processed. Taking into account the superior broadband frequency behavior of the fiber, only its attenuation of about 0.2 $\mathrm{dB/km}$ has to be taken into account. For the frequencies used here and distances within tens of kilometers, chromatic dispersion is not an issue. However, for higher carrier frequencies or longer distances, this effect has to be considered.

Frequency characteristic

The frequency characteristic is one of the most important features of a transmission system. With the fiber being a transparent medium, the bandwidth is determined by the combination of the active Rx and Tx antenna systems. In Figure 3.43, the transmission function of the Tx and Rx antenna are shown. Measured with a network analyzer, known test antennas and test senders and receivers (Agilent 83403C / Agilent 83411D), the electro-optical and opto-electrical performance of the Rx and Tx antenna could be characterized. The flat frequency response of both antennas is achieved by balancing increasing antenna gain, increasing losses and decreasing amplifier gain as well as decreasing modulation response with frequency as described in chapters 3.2.1 and 3.2.2. The antenna matching and gain limits the lower operating frequency while the higher frequencies are limited by the electronic components.

Nonlinearities

For systems with analog modulation as in RF-over-Fiber approaches, nonlinearities may limit the system performance. E.g., in multi-carrier systems, intermodulation can lead to serious distortions. Unfortunately, in in microwave photonic links, many components introduce nonlinear distortions. Being a cross-domain technology, microwave

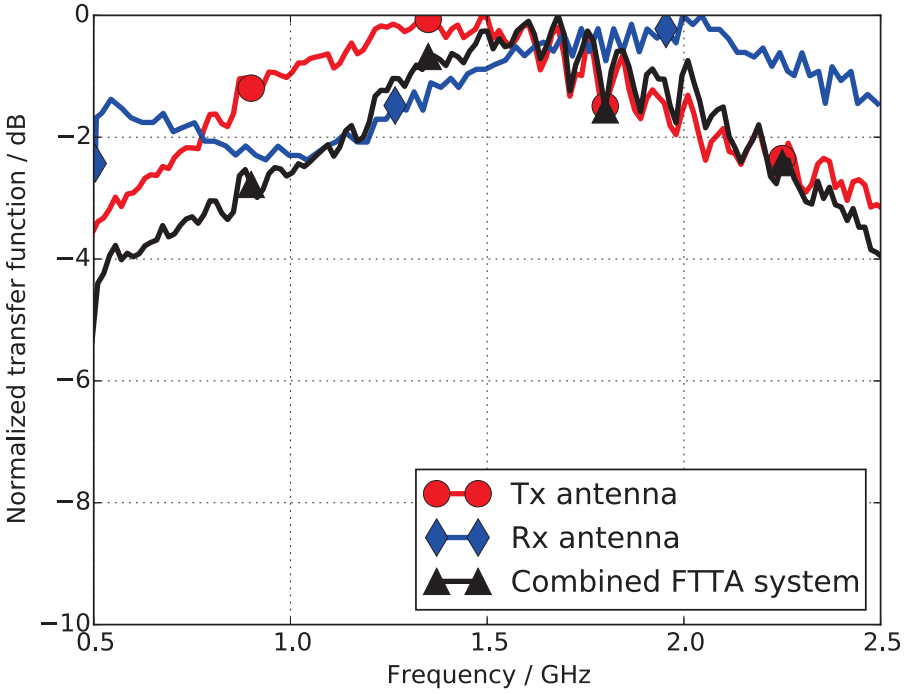

Figure 3.43: Measured Frequency characteristics of the fiber-coupled active antenna system: Rx antenna (blue), Tx antenna (red), combined (black)

photonics has to deal with different kinds of nonlinear effects. In electrical domain, components may have a nonlinear characteristic between (electrical) input and output, e.g. amplifiers. The opto-electrical conversion at the photodiode exhibits a square-law characteristic. In other words, the photocurrent has a linear dependency on the optical power. Therefore, it is desirable to also have a linear dependency between modulation voltage or current and optical power. Furthermore, nonlinear responses such as Kerr effect or stimulated scattering may occur in the optical waveguides. The separate effects have been discussed in chapter 2 on the basics of microwave photonic systems.

As mentioned in chapter 2.2, the optical transmitter suffers from a nonlinear characteristic. For direct modulation, the dependency between optical power and electrical input is exponential. When an external Mach-Zehnder modulator is used, the relationship is cosine-like. In the configuration used in this experiments, most of the nonlinearities are introduced by the limiting amplifier in the Rx antenna. The system has not been optimized for linear behavior as can be seen in Figure 3.44. Cost-effective off-the shelf components for digital systems have been used. Specialized counterparts designed for analog systems exist but are more costly. Consequently, the 3rd order harmonic is only suppressed by 9 dB. Anyway, the eye diagrams from the system demo in the next section do not show any major influence. When transmitting more than one signal with strong tones, this may change, though. Research in that direction was out of scope for this trial.

It is worth mentioning that for optical baseband transmission, first investigations regarding the influence of (electrical) nonlinearities on the performance of higher-order modulation formats have been carried out [98]. Exemplary, the PAM4 modulation format was studied a direct modulation / direct detection scheme. This is also the significant scheme for Radio-over-Fiber / FTTA transmission. With the error vector magnitude as metric, it could be demonstrated that the common noise-loading at the receiver is not advisable anymore under nonlinear conditions. Due to the performance increase of low-pass filtering, the bandwidth of the components should not exceed the two-fold of the symbol rate. It could be motivated that the 1 dB compression point of electrical components is a good parameter to characterize the performance deterioration due to nonlinearities. First indications show that for input powers 3 dB below the 1 dB compression point nonlinear effects can be neglected.

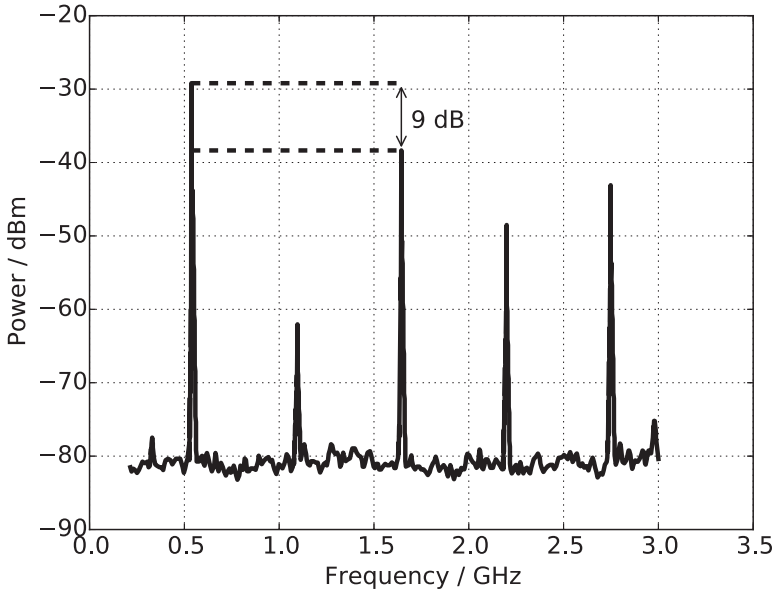

Figure 3.44: Measured spectrum for single tone (537 MHz) excitation

System demonstration

To experimentally verify the FTTA system, pseudo random NRZ OOK data from a Centellax PRBS generator modulated on a 1.5 GHz carrier using a MiniCircuits ZX05-42MH mixer served as wireless signal. This signal fills the entire available bandwidth from 500 MHz to 2.5 GHz. Unlike multiple signals on different carriers, this case relies on a flat channel covering the whole bandwidth. Therefore, this test case is considered most critical. Implementing IQ mixers for electrical up and downconversion (as in the RoF transmitters in chapter 3.3.1) enables complex modulation formats such as QPSK. That would increase the spectral efficiency and achievable data rate.

The downstream wireless signal was directly modulated on a DFB laser diode at the central station. It should be noted that no additional filtering (e.g. mirror frequencies) was carried out because the Tx antenna frequency characteristic could be used as bandpass filter for the wireless signal. The upstream signal was received by a photodiode in the central station. After amplification (PicoSecond Pulselabs 5828-108 and MiniCircuits ZJL-7G), downconversion (MiniCircuits ZX05-42MH) and lowpass filtering (to avoid the mirror frequencies), the eye diagrams of the baseband data were measured with an Agilent 90804A realtime scope.

The fiber network consisted of SMF spans (25-50 km) from the CS to the Tx antenna array (introduced in section 3.2.1) in 2x1 configuration steered with the optical beamforming network (from 3.2.1) at 0°. The wireless signal was transmitted only over a few meters due to Tx power restrictions to some milliwatts. The laser diode on the Rx antenna has a lower optical output power than the one in the CS. Hence, only shorter fiber lengths from the Rx antenna to the CS (0-20 km) could be realized. Figure 3.45 summarizes the setup.

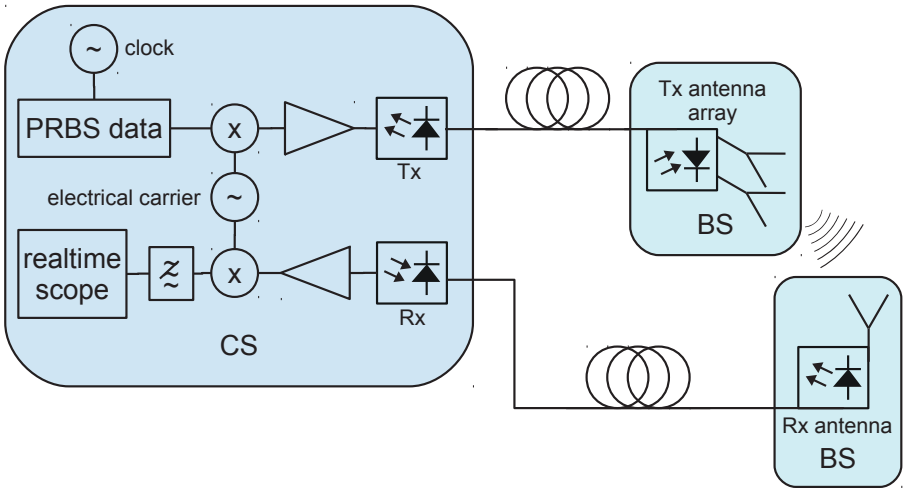

Figure 3.45: Block diagram of experimental setup

The maximum data rate that could be shown was 1 $\mathrm{Gbit/s}$. Figure 3.46 shows the eye diagram at the receiver. The measured average Q factor of 5.6 corresponds to a bit error rate of $1 \cdot 10^{-8}$. Being at the bandwidth limit of the system, a deteriorated signal-to-noise ratio permitted only shorter transmission distances over the fiber link. While the more advanced transmitter at the CS could support up to 25 km to the Tx antenna, distances over tens of meters between the Rx antenna and the CS lead to high bit error rates. Low optical powers at the CS photodiode imply weak electrical signals that suffer from LO interference after mixing with the carrier for downconversion.

With lower data rates, also longer optical spans could be demonstrated at low bit error rates. 45 kilometers between CS and Tx and 10 kilometers between Rx and CS or 25 km CS-Tx and 20 km Rx-CS are typical metro network scenarios. At a data rate of 750 $\mathrm{Mbit/s}$, in both cases error-free transmission has been shown. The Q

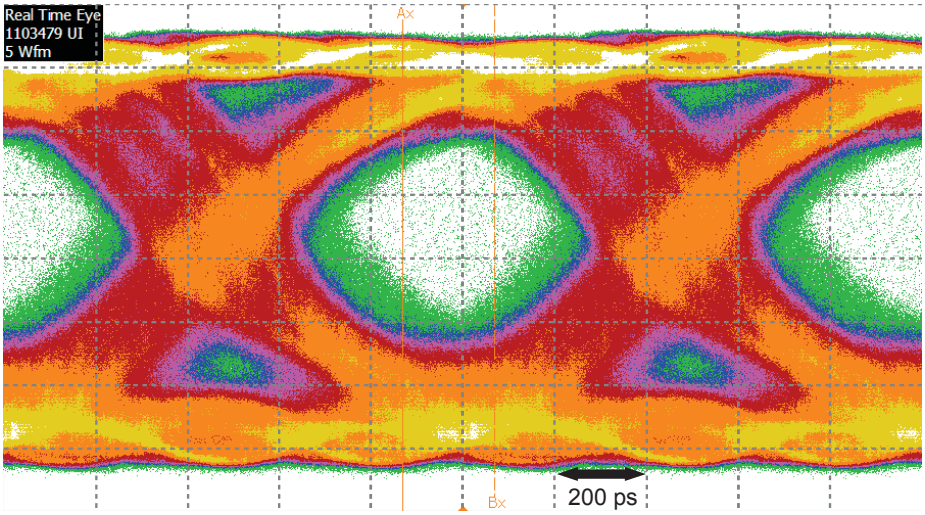

Figure 3.46: Measured eye diagram of received signal at 1 Gbit/s (25 km transmission distance between CS and Tx antenna)

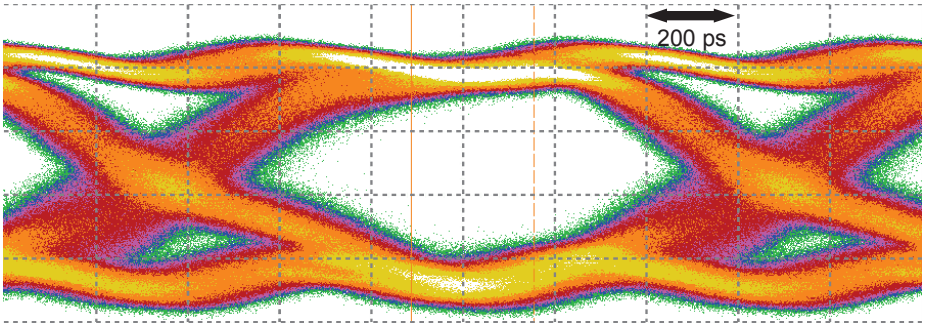

Figure 3.47: Measured eye diagram of received signal at 750 Mbit/s (45 km transmission distance between CS and Tx antenna and 10 km between Rx antenna and CS)

factors were 10.2 and 8.2, respectively. Figure 3.47 shows the eye diagram retrieved with the first setup.

Due to the comparably low carrier frequency of 1.5 GHz and transmission distances below 60 km, no influences of chromatic dispersion could be observed. Lower data rates (e.g. 500 Mbit/s) have been tested with carrier frequencies in the range between 1 GHz and 2 GHz without any influence on the bit error rate. In general, the smaller the bandwidth occupied by the service is, the less vulnerable it is to channel distortions.

The main reason for the use of higher carrier frequencies is the availability of more bandwidth. This enables larger data rates that can be even increased when using advanced modulation formats like mPSK or mQAM. These formats require a modification in the central station and the mobile unit: IQ mixers have to be used for upconversion and downconversion (see chapter 3.3.1). The optical part of the system (Rx / Tx antennas) does not have to be upgraded because the RF signal is transported transparently over the fiber.

However, when migrating to higher frequencies (e.g. 60 GHz), power fading is expected. Single sideband modulation used for the Radio-over-Fiber system in section 3.3.1 will relax this issue. For signal bandwidths of more than 10 GHz, dispersive effects may affect the data itself. Electronic equalization at the receiver can be applied in that case [2, 4, 6]. Also, dispersion compensation schemes from optical communication can be applied. This effort can be reduced if shorter achievable transmission distances are sufficient.

Up to 40 GHz, directly modulated laser diodes (discussed in chapter 2.1) are available. For even higher frequencies, external modulators have to be used. Of course, components (substrates, amplifiers, laser diodes etc.) are more costly for higher frequencies as well. Loss in electrical domain increases and antenna size decreases with increasing frequency. This indicates a higher level of integration. For example, in K band, interesting solutions with directly modulated laser diodes and integrated antennas are presumable for satellite links.

Wavelength division multiplexing (i.e. lasers with different wavelengths) helps handling more than one remote antenna unit from one central station. Separated by WDM demultiplexers, more than 100 antenna units may be addressed by one fiber.

Conclusion

FTTA is a very promising approach within the scope of microwave photonic systems. The combination of optical components, electronics and antennas enables a new class of systems that has to be designed and analyzed in a holistic way as presented in this section. The exemplary full-duplex up- and downlink FTTA system with integrated optical fiber-coupled antennas has a huge relative antenna bandwidth of 133% (i.e. baseband data bandwidth of 67%). Thus, the simultaneous transmission of many wireless signals is supported. A data rate of 1 $\mathrm{Gbit/s}$ has been modulated on a 1.5 GHz carrier frequency using simple OOK modulation. Fiber distances of up to 60 km have been shown. That validates the system in a typical optical metro network environment. Starting from around 60 GHz, in-package antennas are an interesting option. This implies an electro-optical RF capable package. For even higher frequencies (e.g. 180 GHz), a direct integration of antennas in a silicon photonics process will be attractive due to the smaller footprints of the antennas. Summarizing, future system architectures of wireless networks with higher levels of centralization and deeply integrated antenna sites are expected to be built on the basis of the early results demonstrated in this chapter. A scaling towards mm-wave frequencies renders the FTTA concept even more valuable.

3.3.3 Wireless readout of optical sensors

The versatile use for optical sensors is justified by their low susceptibility to electromagnetic interference, high precision, excellent compatibility with biological substances and favorable handling in peculiar environmental conditions. A broad range

of physical or mechanical parameters like temperature, pressure, strain, bending, refractive index, humidity and many more can be measured. Chemicals and biological agents in liquid and gaseous samples, radiation, electrical and magnetical fields can be detected, too. Among others, the field of use includes automotive, avionic, geological, environmental and medical applications as well as tasks in health monitoring and industrial fabrication processes.

Typically, optical sensors are read out using costly and bulky evaluation units such as spectrometers being attached to the sensors by optical fiber. Not only is this difficult in harsh environments (e.g. in production plants) or when dealing with mobile sensing targets (for health monitoring of sick or elderly people or in assisted living scenarios) but also must the evaluated sensor signal be transmitted to a central unit, converted and processed. The standard approach of using a wireless modem attached to the evaluation unit adds extra cost and complexity while not fully addressing the size and mobility issues. The solution described in this chapter offers a compact read-out that comes with wireless transmission and a potentially low power usage.

Combining the RoF / FTTA concept (see chapter 3.3.2) using a fiber-coupled antenna (section 3.2.1) with optical sensors provides a flexible system where the evaluation takes place at the radio receiver simplifying the evaluation unit [104, 127]. No on-site processing is necessary any more. However, this implies that the optical source used for the interrogation of the optical sensor has to be modified. First, the design of possible optical sensors is discussed and a long-period-grating (LPG) temperature sensor for use in the exemplary implementation will be introduced. Following, the system design, the novel evaluation scheme and calibration procedures are explained. Finally, a proof-of-concept setup is characterized.

Optical Sensor

Regardless of the specific operation scenario and the transducer principle of an optical sensor, it always modifies its input signal in terms of spectral or polarization behavior, delay or phase. This change can be modeled using a transfer function. The evaluation of the sensor quantities always takes place in electrical domain. That means, any change induced by the sensor has to be translated in a modulation of the optical power in order to use a photodetector for opto-electrical conversion. This instantaneously yields compatibility with the previously proposed RoF transmission and evaluation scheme. The heritage from optical communications offers a broad range of cost-effective fiber-coupled components (laser source, modulator, couplers, detectors, ...) supporting low-loss coupling which improves the available dynamic range of the sensor system.

A resonant sensor mechanism is particularly beneficial. The optical resonantor absorbs the power from the input in a small portion of the spectrum depending on the sensed quantity. When the input signal generated by the RoF transmitter is located at the rising or falling slope of the resonator spectrum, high sensitivity can be achieved. All kinds of interferometers are good candidates to provide resonators, e.g. built up with planar waveguides [70]. Micro-mechanical structures [143] allow

the implementation of very compact and robust sensors. Also plasmonic effects [128], photonic crystals [53] and grating couplers realized with optical fibers [125] can be used. Especially fiber-based sensors can be conveniently integrated into RoF systems.

In fibers with Germanium doped core, UV exposure leads to an increase of the refractive index. A periodic refractive index modulation as shown in Figure 3.48 is called grating. In the grating, power is exchanged between different guided fiber modes due to constructive interference of light scattered at the periodic refractive index variations within the grating. The light transfered by the grating from the basic mode of the fiber can be seen as a notch in the optical transmission spectrum at the resonance wavelength λ_R. The resonance condition depends on the grating period Λ and the difference of the effective refractive indices of the modes participating in the coupling process Δn_{eff} [41]

$$\lambda_R = 2\Lambda\Delta n_{\text{eff}} \,. \tag{3.53}$$

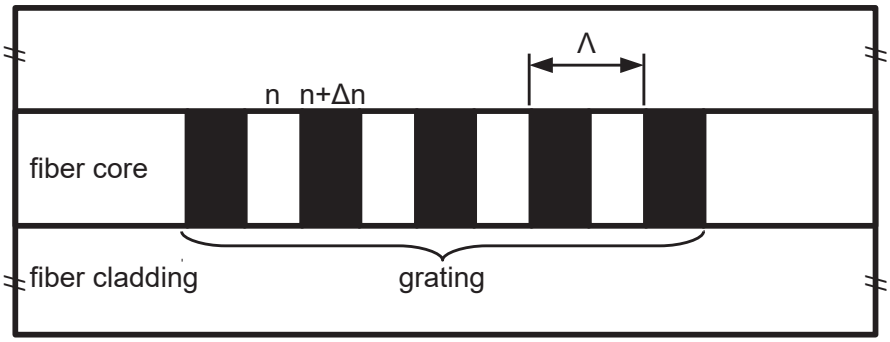

Figure 3.48: Grating in single-mode fiber.

The grating period can be used to classify different grating types. Small periods of a few hundred nanometers lead to so-called fiber Bragg gratings (FBG) coupling counter-propagating core modes. They can be used e.g. for temperature and strain sensing [118]. Longer periods in the micrometer range forming a so-called Long Period Grating (LPG) couple core modes and co-propagating cladding modes ($\mathrm{HE}_{1,\mathrm{X}}$). The $\mathrm{HE}_{1,\mathrm{X}}$ modes reveal an evanescent field outside the fiber cladding. The interaction of this field with the outside medium can be used to detect refractive index changes of the surrounding medium leading to a shift of the resonance wavelength λ_R due to a changing effective refractive index. Receptor molecules attached to the fiber cladding within the decaying evanescent field help detecting corresponding biochemical substances [126]. Coating the fiber with a hydrogel can be used for pH [132] and humidity [146] measurements. Surface plasmon resonance (SPR) boosts the sensitivity of the refractive index evaluation by adding a thin metal coating to the fiber [128].

Among the multitude of fiber-optical sensors, a LPG-based temperature sensor is chosen for the demonstration. The effective refractive index of the fiber changes with temperature and results in a shift of the resonance wavelength. Compared to FBGs, the sensitivity when coupling in cladding modes is two orders of magnitude

higher [61]. In Figure 3.49 (bottom), the change of the effective refractive indices of the core mode and of different $\mathrm{HE}_{1,\mathrm{X}}$ cladding modes is shown. The evaluation of equation (3.53) leads to the grating line. Whenever the grating line and a higher mode intersect, coupling is possible (dashed vertical lines in both subplots). Thus, the sensor may be operated at different wavelengths. A temperature-induced change of the effective refractive index of the fiber leads to a different position in the spectrum where higher order modes and grating line intersect and, consequently, in a different wavelength of the resonance. The notch in the transmission spectrum moves as shown in Figure 3.49 (top). A lower angle between the cladding mode line and the grating line in Figure 3.49 (bottom) leads to a higher spectral shift caused by the temperature change. Therefore, an intersection point like at about 1550 nm ($\mathrm{HE}_{1,10}$) should be chosen for high sensitivity. This matches well the typical wavelengths of transmitters in the third optical window used by RoF transmitters.

The LPG temperature sensor could be further optimized by changing the amplitude of the refractive index modulation which affects the effective refractive index. The behavior of the cladding modes can be tuned by adjusting the cladding diameter. However, that was out of scope for the proof-of-concept demonstration.

A precise point-to-point writing process [113] has been carried out to realize the 30 mm long LPG using a focused beam of a frequency-doubled argon-ion laser (244 nm wavelength). The grating inscribed into standard single-mode fiber that was hydrogenated for two weeks to increase photosensitivity has a period of 243 $\mu\mathrm{m}$. In the spectrum of the temperature sensor (Figure 3.49, top) at 23°C, the resonances caused by transfering the input power of the core mode into different cladding modes can be seen. At 1530 nm, the grating couples around 15 dB of optical power from the core mode to the $\mathrm{HE}_{1,10}$ cladding mode. The measured spectrum matches well with numerical simulations by Optiwave IFO-Gratings.

RoF transmission

As mentioned before, the traditional way to evaluate an optical sensor is to use a laser line at the wavelength of the sensor slope in order to convert the spectral change of the sensor characteristic into an attenuation of the optical signal. This change of optical power can be detected by a photodiode. However, this produces a DC signal that cannot be wirelessly transmitted. That's why the laser source has to be changed to a Radio-over-Fiber transmitter (similar to those used in chapter 3.3.1 and 3.3.2). In Figure 3.50, the block diagram of the proposed system is shown. For the proof-of-concept implementation, a carrier frequency of 2.5 GHz has been chosen. Also WiFi and Bluetooth transmitters operate in this ISM band. The electrical carrier modulated on the laser source within the RoF transmitter enables a direct transmission of the RoF signal after being influenced by the sensor (a temperature sensor in this example). The wireless signal is received and its power fluctuations are evaluated. The evaluation and calibration procedure is discussed in detail in the next subsection.

The signals propagating through the system are shown in Figure 3.51: In subplot a), the output spectrum of the RoF transmitter can be seen. Being connected by optical

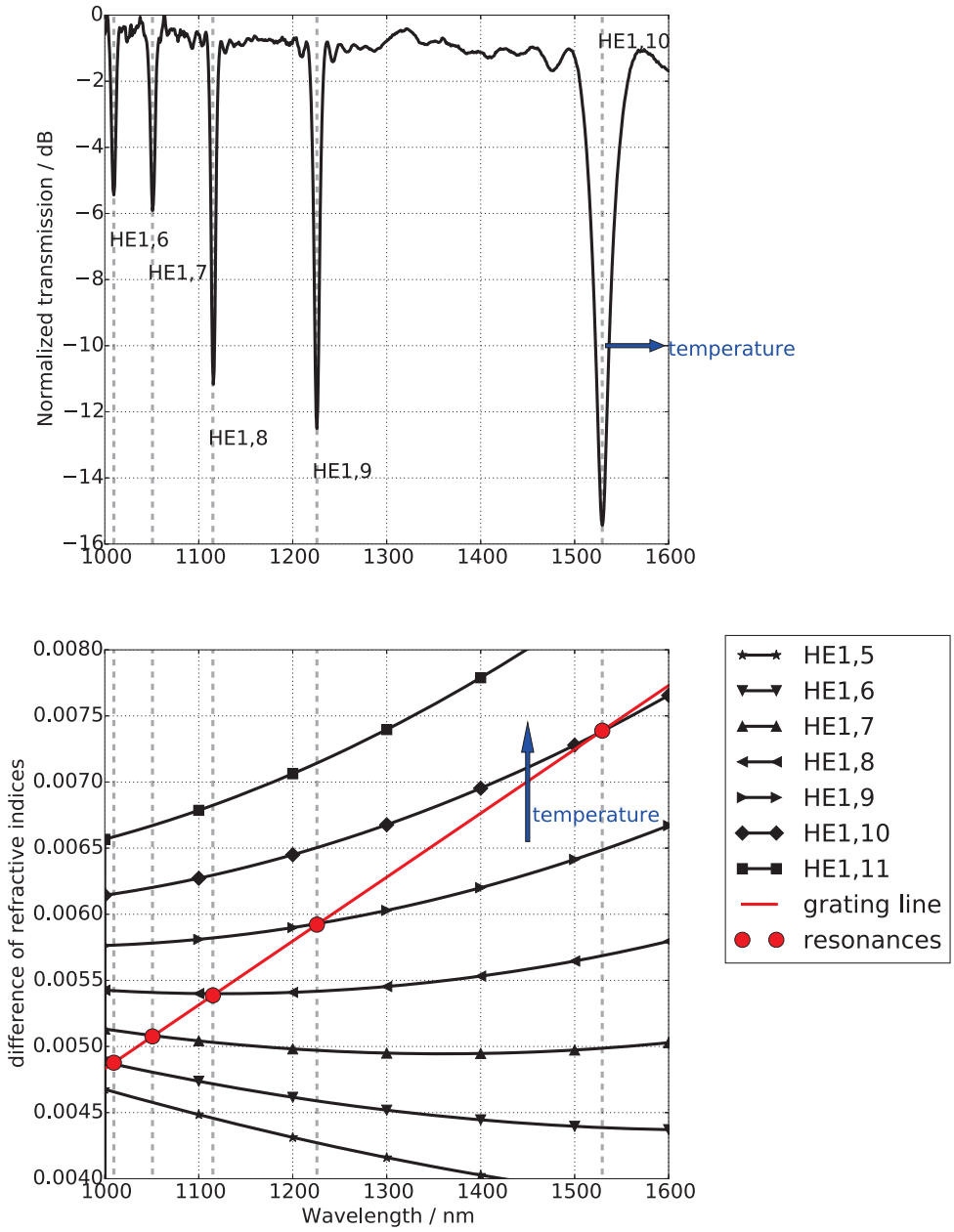

Figure 3.49: Top: Transmission spectrum of LPG-based temperature sensor at 23°C environmental temperature. Each notch corresponds to the coupling of optical power from the core mode to a certain $HE_{1,X}$ cladding mode (resonance). Bottom: Wavelength-dependent difference of the effective refractive indices of the core and $HE_{1,X}$ cladding modes. Intermodal coupling causing energy transfer (resonance) between the the modes takes place at the intersections with the grating line (see equation (3.53)). The spectral shift of the resonance wavelength is higher if the intersection angle is flatter.

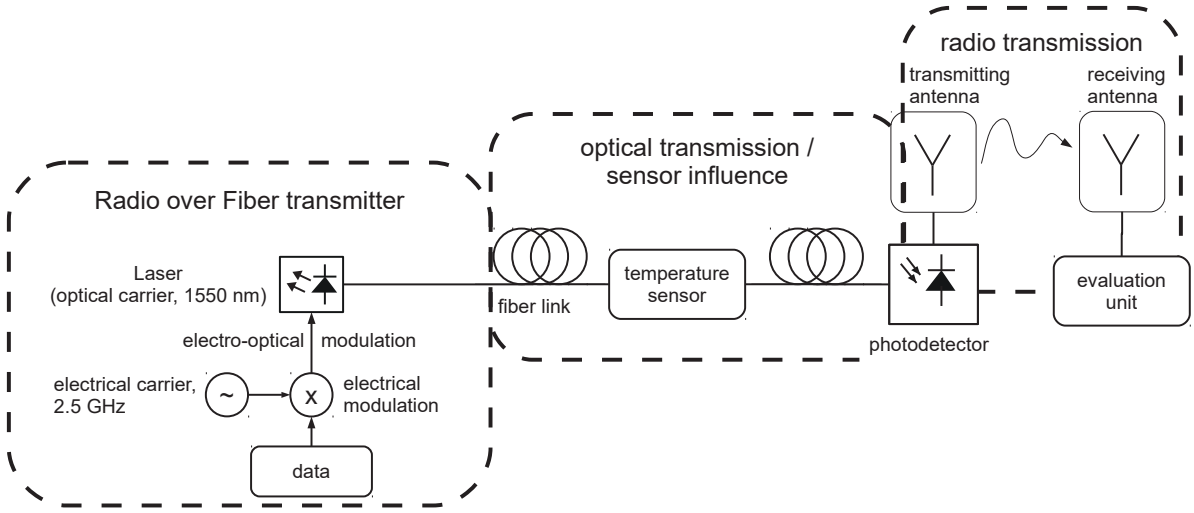

Figure 3.50: Block diagram of wireless transmission of optical sensor data using Radio-over-Fiber approach

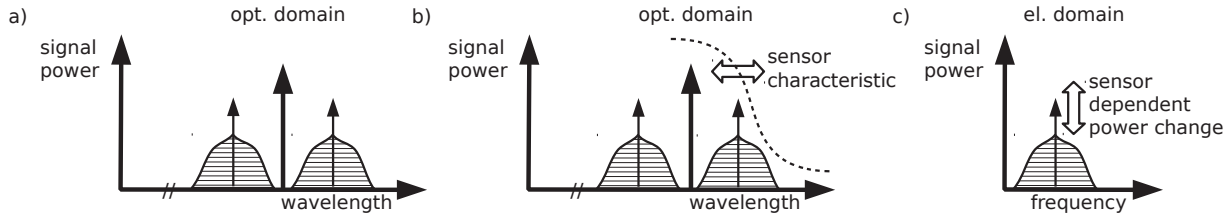

Figure 3.51: Simultaneous wireless transmission and evaluation of optical sensor: a) RoF transmitter output signal, b) signal being influenced by the optical sensor, c) received sensor signal after wireless transmission

fiber, it can be installed conveniently at a remote location. The sensor itself can be located within a hostile environment (high fields, exceptional temperature, limited space, no external power etc.). After being influenced by the sensor characteristic, the RoF signal with imprinted sensor value (Figure 3.51 b)) is transported over fiber to the antenna location. A photodiode converts the signal from optical to electrical domain and an antenna transmits the electrical signal wirelessly. The antenna acts as bandpass filter and radiates only the electrical carrier generated before at the RoF transmitter. DC and mixing components are blocked. At the remote wireless receiver, the signal shown in Figure 3.51 c) is recovered and can be evaluated as follows.

Evaluation and calibration

To be able to distinguish between the sensor influence and cross dependencies, a calibration procedure is needed. Unwanted effects on the received signal include the wireless channel and parasitic effects during the optical transmission.

Different architectures for providing the reference signal can be used as shown in Figure 3.52. The most simple and flexible appproach is to add the reference signal after the sensor. The disadvantage of this approach is that parasitic effects at the transmitter, on the connection of the transmitter to the sensor as well as the combiner cannot be calibrated. Also, this scheme requires two Radio-over-Fiber transmit units. When synchronized, the same wireless carrier frequency f_c and the same laser wavelength λ can be used. However, in order to prevent interference between both lasers, one has to be switched off while the other is transmitting. The turn-on delay of the laser of around 1 ns [1, 153] limits the switching speed between sensor and reference signal. It is also possible to work at different wavelengths and different wireless frequencies at the cost of reduced calibration reliability due to possibly wavelength dependent or frequency selective channels.

Adding an optical switch reduces the need to only one RoF transmit unit. The switch and the combiner cannot be calibrated but fluctuations in the RoF Tx can be canceled out that way. Optical switches are usually micro-mechanical devices, therefore the switching speed is limited to typically 10 ms [112].

The third option is to use one electrical laser driver and switch it electronically to drive two laser diodes with different wavelengths. This enables high switching speeds and reliability. The wavelength of the laser diode for the reference has to be spectrally separated from the operational wavelength of the sensor so that it may pass the sensor without being influenced. This way, parasitic effects in the laser driver but not in the lasers itself can be calibrated. It is worth mentioning that for sensors operating in reflection, additional effort has to be spent, e.g. inserting a mirror after the sensor. This may lead to additional uncertainties in the calibration process.

The subsequent investigations focus on realizing a simple frontend working at low frequencies in the megahertz range. Consequently, a second electrical carrier at a different frequency near the wireless sensor signal frequency is used, i.e. the first reference signal architecture shown in Figure 3.52 a) is applied. Under adverse conditions in the wireless channel, its transfer function may change from maximum to minimum

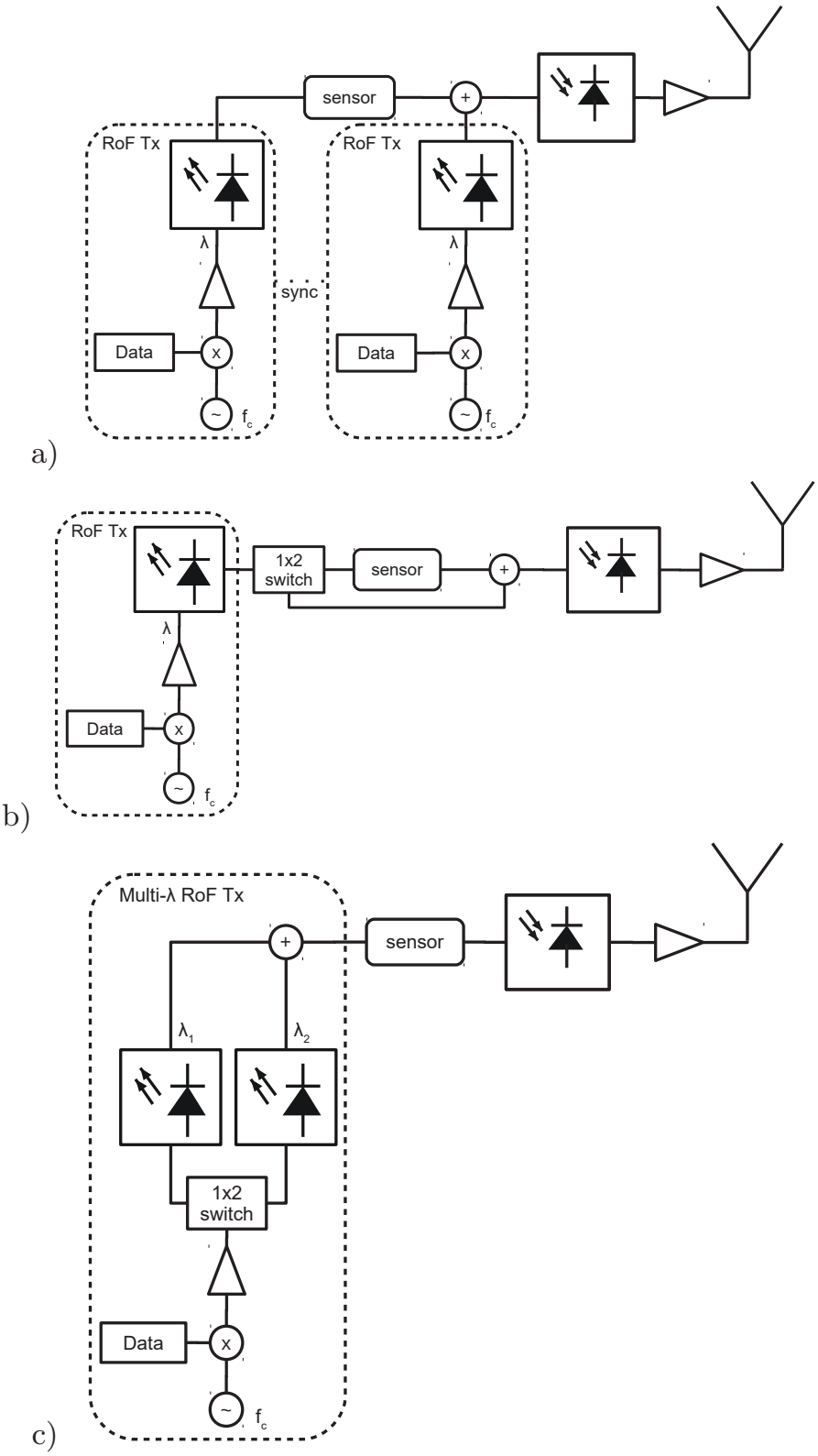

Figure 3.52: Reference signal architectures: a) reference signal added after sensor, b) reference signal added after sensor (optically switched), c) reference signal added before sensor at different wavelength.

within a frequency range of a few megahertz, e.g. two paths with length difference of 15 m lead to a 20 MHz channel periodicity. If both paths have equal power, total extinction of the signal is possible. However, for typical scenarios, the wireless channel is flat for such small frequency offsets. Being not influenced by the optical sensor but experiencing the same radio channel and impairments in optical domain, the parasitic effects can be separated from the sensor impact. It may be transmitted with the same antenna as the sensor signal after optical combining (option (1)) or with a second antenna (option (2)) in the vicinity of the first one to ensure a similar radio channel. The proposed setup is depicted in Figure 3.53.

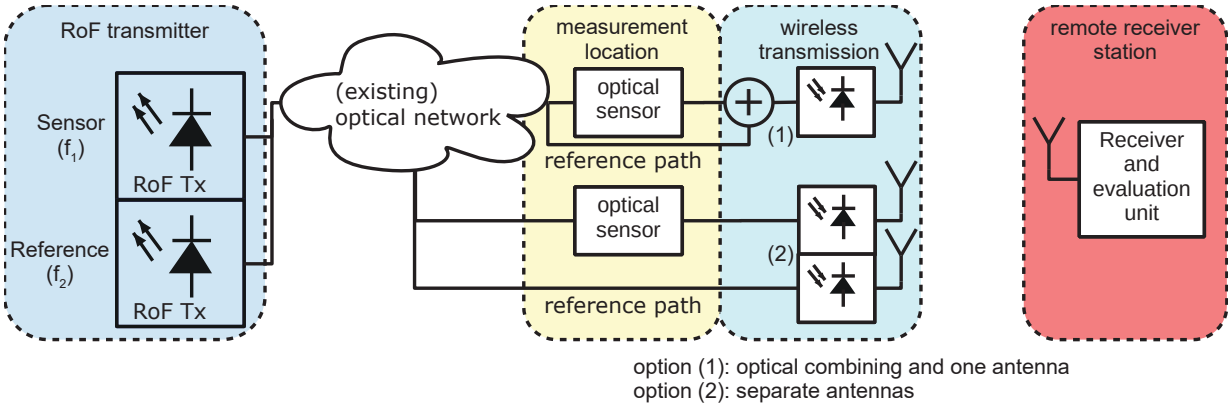

Figure 3.53: Setup with wireless transmission options (optical combining and one antenna or two antennas in close vicinity) using reference paths to calibrate out cross dependencies of the sensor and the link

Following, the processing of the received wireless signals is explained. Although the sensor signal as well as the reference carrier may be modulated with data (e.g. for identification of the sensor or for sensitivity enhancement with spread codes similar as in navigation systems), the comparably narrowband system can be treated as single tone to simplify the mathematical derivations.

The received wireless sensor signal x_1 is characterized by its amplitude a_1, frequency $\omega_1 = 2\pi f_1$ and phase φ_1

$$x_1 = a_1 \sin(\omega_1 t + \varphi_1) \; . \tag{3.54}$$

Depending on the sensor value, a_1 changes. The amplitude a_2 of the received reference signal x_2, however, is not influenced by the sensor. As stated before, the reference tone operates at the different frequency $\omega_2 = 2\pi f_2$. It is used as phase reference ($\varphi_2 = 0$).

$$x_2 = a_2 \sin(\omega_2 t) \tag{3.55}$$

It is worth mentioning that the phase of the wireless sensor signal φ_1 changes constantly due to the frequency offset between the reference signal f_2 and the sensor signal f_1. A fixed phase relation would only occur when there is no frequency offset or when the reference signal frequency is a multiple or fraction of the sensor signal frequency. This is clearly not the case. The phase change repeats itself with the

frequency difference of both signals ($\Delta f = f_1 - f_2$) in the megahertz range (i.e. nanoseconds)

$$T_{\mathrm{LF}} = \frac{1}{\Delta f}\,. \tag{3.56}$$

Thus, the initial phase difference φ_1 does not have any impact on the further evaluation. The reference and sensor signals do not interact in optical domain. Propagating through (approximately) identical wireless channels results in an identical attenuation of both amplitudes a_1 and a_2. Hence, the ratio $\frac{a_1}{a_2}$ remains constant and can be used as a criterion to determine the sensor signal.
After self-mixing of the received signal consisting of sensor and reference contribution

$$y = (x_1 + x_2)^2 \tag{3.57}$$

the produced spectral components may be evaluated. Limiting the evaluation to the DC component and the low-frequency (LF) beating frequency Δf between the sensor tone and the reference tone allows the use of low frequency hardware (with upper frequencies in the megahertz range). Components at higher frequencies (i.e. f_1, f_2, $2f_1$, $2f_2$, ...) can be ignored. That way, a cheap, simple and energy-efficient system may be designed.
The DC component is

$$y_{DC} = \frac{a_1^2}{2} + \frac{a_2^2}{2}. \tag{3.58}$$

The LF beating signal at Δf can be expressed as

$$y_{LF} = a_1 a_2 \left[\cos(2\pi \Delta f t - \varphi_1)\right]\,. \tag{3.59}$$

Measuring the power of both components

$$P_{DC} = \frac{1}{T_{\mathrm{LF}}} \int_0^{T_{\mathrm{LF}}} y_{DC}^2 \mathrm{d}t = \left(\frac{a_1^2}{2} + \frac{a_2^2}{2}\right)^2 \tag{3.60}$$

$$P_{LF} = \frac{1}{T_{\mathrm{LF}}} \int_0^{T_{\mathrm{LF}}} y_{LF}^2(t) \mathrm{d}t = \frac{1}{2} a_1^2 a_2^2 \tag{3.61}$$

the ratio between P_{DC} and P_{LF}

$$\gamma = \frac{P_{DC}}{P_{LF}}\,. \tag{3.62}$$

can be evaluated. The ratio between the amplitude of the sensor signal a_1 and of the reference signal a_2 is a function of the measured ratio of the DC and LF power

$$\frac{a_1^2}{a_2^2} = \sqrt{\gamma^2 - 2\gamma} + \gamma - 1\,. \tag{3.63}$$

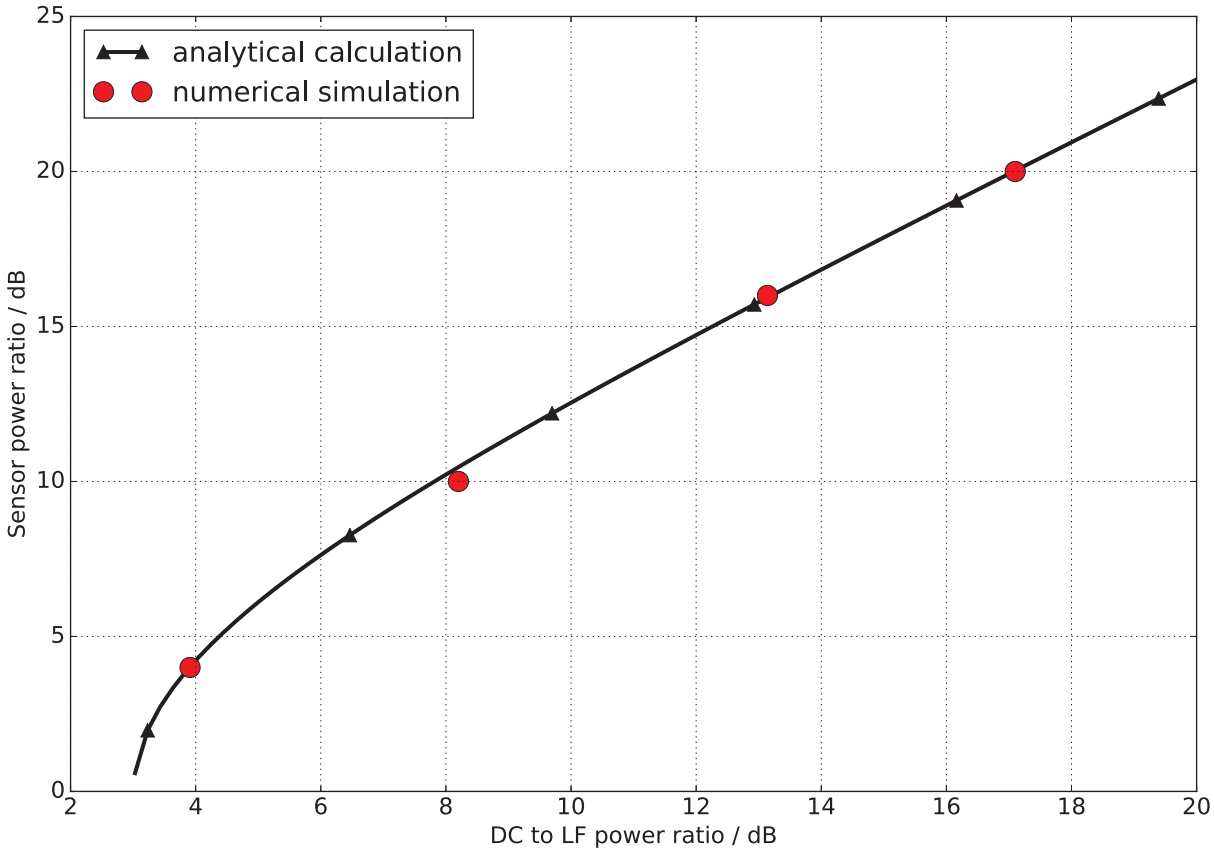

Figure 3.54: Sensor value to reference power ratio ($\frac{a_1^2}{a_2^2}$) depending on measured DC to LF power ratio $\gamma = \frac{P_{DC}}{P_{LF}}$

In order to validate the analytical calculations when the sensor system is realized with typical components, it has been simulated with VPItransmissionMaker. For the simulation, no data has been moduated on the laser sources. Two DFB lasers have been used: The first one (wavelength $\lambda_1 = 1552.8$ nm, modulation frequency $f_1 = 2.45$ GHz) served as source for the sensor signal and the second one (wavelength $\lambda_2 = 1553.6$ nm, modulation frequency $f_2 = 2.55$ GHz) was used as reference. The sensor influence was modeled as variable attenuation of laser 1. The optically combined signal of laser 1 and laser 2 was received with a photodiode. At the output of the self-mixing setup, the power of the DC component and the produced line at $f_1 - f_2 = 100$ MHz was measured. Additionally, the laser powers a_1^2 and a_2^2 were probed. Figure 3.54 underlines the good match between simulated results and the analytical computation.

Measurements

A simplified proof-of-concept measurement has been carried out with the temperature sensor discussed earlier. Measuring directly at the output of the wireless transmit-

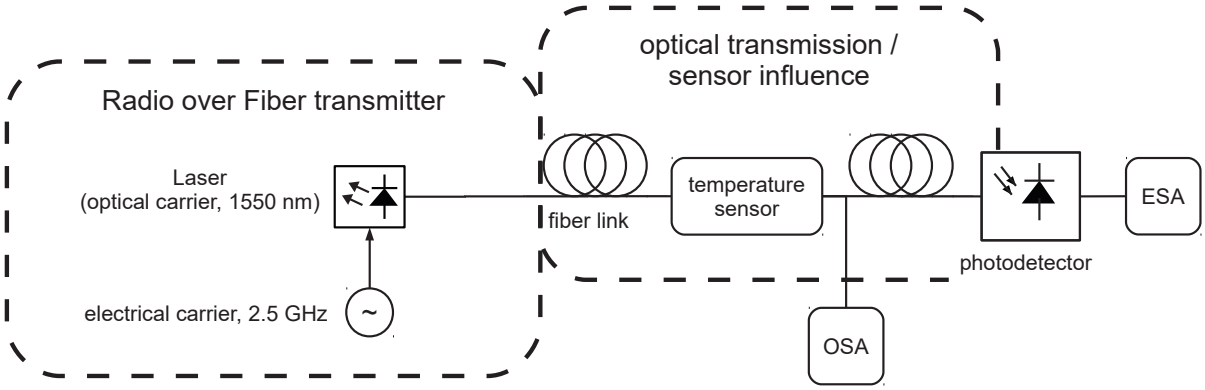

Figure 3.55: Simplified measurement setup for RoF sensor validation

ter (i.e. without wireless channel, see Figure 3.50) and by carefully controlling the environmental conditions in the lab (in other words, minimizing influences from the optical part), the calibration procedure described in the previous section could be avoided. Therefore, no reference RoF transmitter is needed in the experimental setup shown in Figure 3.55. The electrical carrier frequency was set to 2.5 GHz. An electrical spectrum analyzer (ESA) has been used to measure the power of the generated wireless signal. For a more detailed analysis, an optical spectrum analyzer (OSA) has been added to monitor the spectrum after the optical sensor. However, in a practical realization, such sophisticated measurement equipment will not be needed. No measurement devices are involved in optical domain. In electrical domain, just (low-cost) filters and power detectors are required.

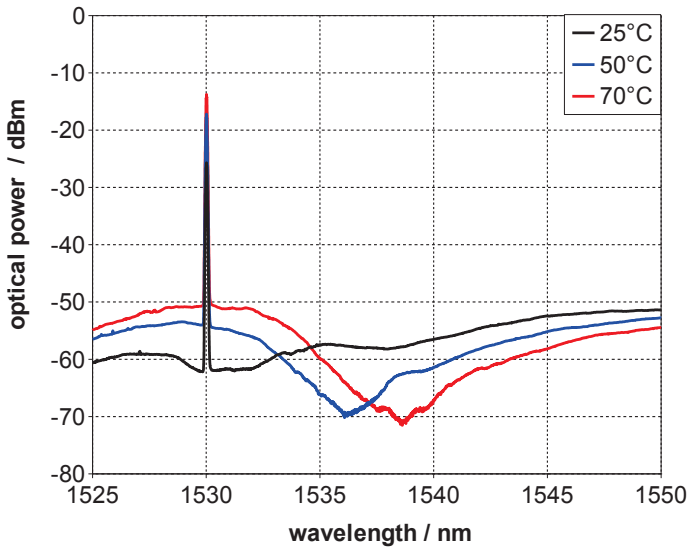

Figure 3.56: Temperature dependent measured optical spectra after the optical sensor

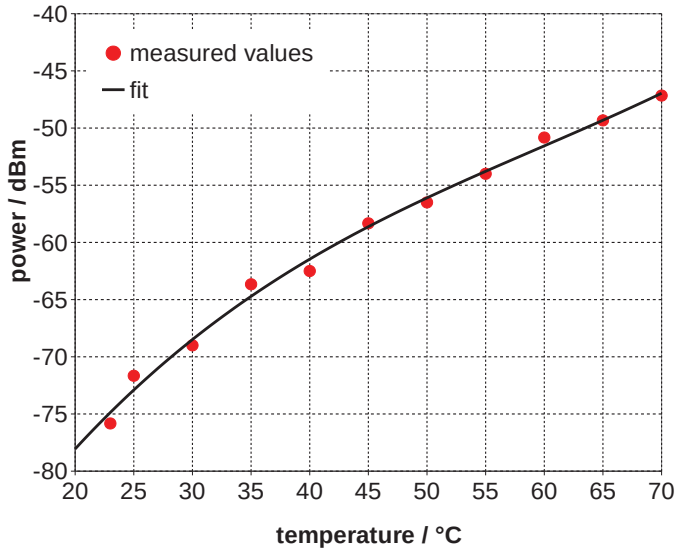

Figure 3.57: Measured electrical power depending on temperature

Figure 3.56 shows the optical spectra after the sensor effect at temperatures of 25°C, 50°C and 70°C. As can be seen in Figure 3.51, the temperature induced wavelength shift of the sensor attenuates the optical signal. This results in a higher attenuation for lower temperatures. After the opto-electrical conversion, also the power of the produced electrical signal that will be transmitted depends on the temperature. The dependency of the wireless signal power from frequency is shown in Figure 3.57. The power-temperature characteristic is unambiguous. Hence, the temperature reading can be extracted from the power measurement.

Application example

One important scenario for optical sensors is the monitoring of buildings, bridges and other critical infrastructure. Also temperature monitoring is a big issue for energy-efficient houses. In new constructions, concrete with carbon fiber instead of steel as reinforcement (carbon concrete composite) can be used as a promising material with lots of benefitial properties. For example, fiber sensors can be directly embedded in the carbon fiber reinforcement. This is a big advantage over bulk electrical sensors such as strain gauges. Also temperature sensors can be realized, e.g. with LPGs as discussed before. Humidity inside the concrete is another quantity that can be sensed with optical fibers being coated with a hydrogel. However, a break-through of this approach is expected when reading out the optical sensors wirelessly is possible. [105]

Proper packaging of the sensors is crucial for their operation. When the fiber sensor is tethered to the carbon fiber reinforcement, shrinking concrete may cause small curvatures along the fiber axis. Furthermore, within the aggressive chemical environment of the concrete, the acrylate coating of the fiber could lose its protective function. This increases the loss in the fiber (microbending loss and ingress of moisture) and

lowers the lifespan of the sensor. There is even the risk that the sensor might be damaged. Macroscopic bending or mechanical shear force will shift the resonance wavelength of the sensor and have to be avoided. On the other hand, the packaging shall not impair the mechanical properties of the reinforcement and the immersion of the sensor in the concrete shall not be interfered with. For strain sensors, a homogeneous strain distribution has to be ensured, e.g. by a frictional connection. The cross-sensitivity of fiber-optical temperature and humidity sensors to strain has to be minimized, i.e. a force neutral connection has to be applied.

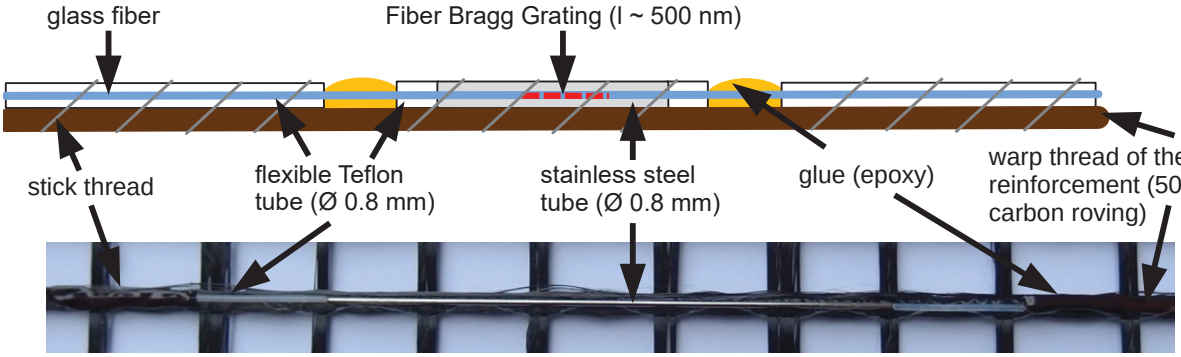

Figure 3.58: Packaged fiber-based sensor stitched on reinforcement carbon roving

Stainless steel tubes have a high tensile strength. It also shields the optical fiber sensor from parasitical shearing forces. That renders the steel tubes most suitable for strain sensors that are able to measure until the carbon fiber reinforcement fails. The drawback of the stainless steel tubes is their low flexibility which prevents them from being integrated directly during the production of the carbon fiber reinforcement. Instead, they are stitched in a second step after production onto the reinforcement. Local gluing ensures a force-fit connection between the reinforcement and the packaged sensor. Figure 3.58 shows the developed package for the strain sensor.

a)

b)

Figure 3.59: Packaging: a) Packaged optical fiber based moisture sensor embedded in carbon reinforcement for carbon concrete composite, b) stitching process

The moisture sensor needs interaction with its environment in close vicinity. Because glass has a similar thermal expension coefficient as the fiber, a glass packaging

reduces thermally induced cross-sensitivity. Also, shielding from parasitic shearing forces is achieved. In order to ensure the wanted interaction with the environment, a half open glass tube is chosen as package. The permeable polyester braid allows moisture to enter the hydrogel coated fiber sensor area but at the same time prevents the concrete from a direct interaction with the hydrogel. In Figure 3.59 a), the packaged moisture sensor is shown. Figure 3.59 b) depicts the stitching process used to fix the package of strain and moisture sensor on the carbon roving.

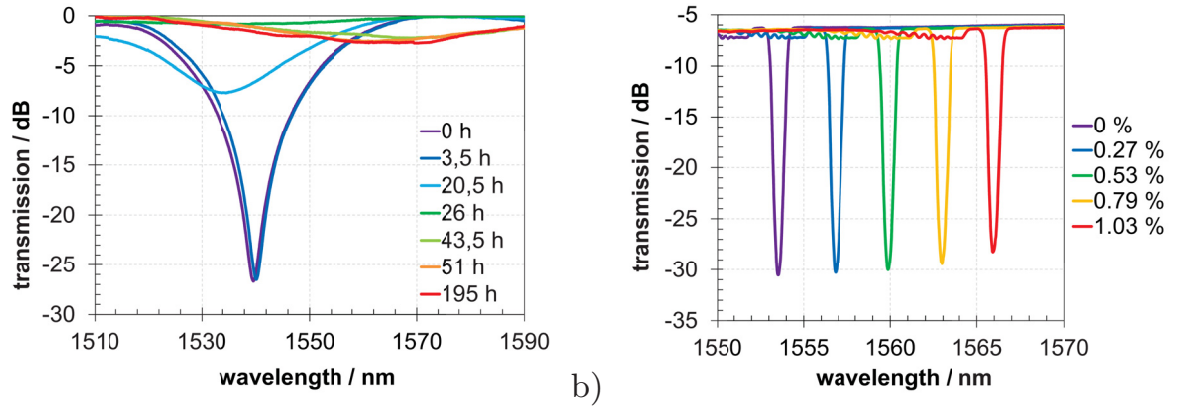

a) b)

Figure 3.60: Sensor spectra: a) humidity sensor during drying of carbon concrete composite, b) strain sensor with respect to applied strain

Figure 3.60 a) shows the measured spectra of the moisture sensor during the drying process of carbon concrete composite. It can be seen that two processes influence the spectral behavior. The clear grating resonance being present under heavy moisture is first blue-shifted during the drying process. At the same time, the depth of the resonance decreases, i.e. its quality factor decreases implying loss. Then, the minimum red-shifts again while the quality factor of the resonance further decreases. Therefore, a direct wireless readout with a RoF signal centered at one specific wavelength is not easily possible due to potentially ambiguous values.

The strain sensor shows a straight-forward shift of the resonance with increasing strain 3.60 b). Therefore, the wireless readout is much easier to implement. Figure 3.62 shows the spectrum of a RoF signal (a DFB laser directly modulated with a RF carrier) for changing spectral characteristics of the strain sensor. The RoF signal power changes when the resonance of the FBG moves. As a result, the radiated wireless power depends on the relative spectral position between FBG and laser. This power is directly connected with the measured strain. Cracking could be successfully detected with a packaged sensor inside carbon concrete composite as shown in Figure 3.61. The sensor characteristic follows nicely the extrusion of the carbon fiber reinforced concrete.

As in the previous measurements, a careful experimental design allows to omit the calibration of the wireless channel because a reflection-free environment leads to a flat channel characteristic with just free space loss that can be described with the Friis equation. Using relative measurements, this loss cancels automatically.

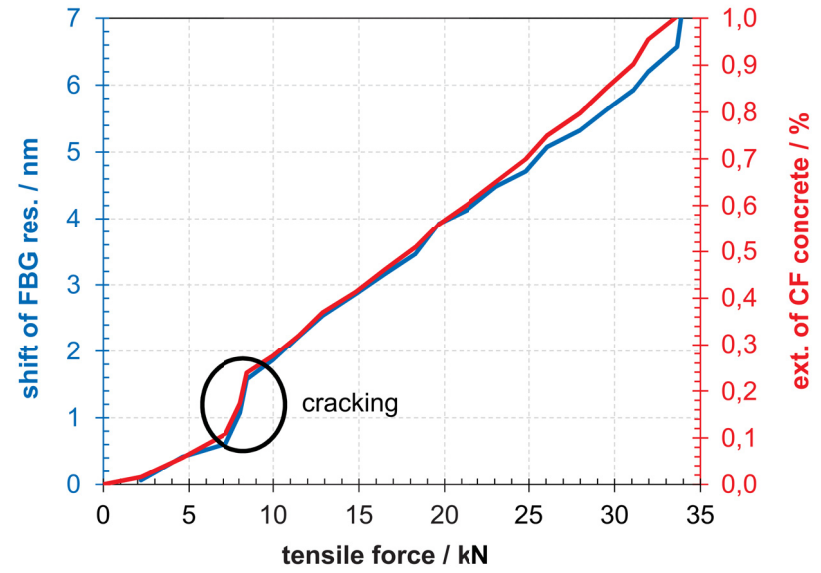

Figure 3.61: Strain sensor resonance wavelength shift

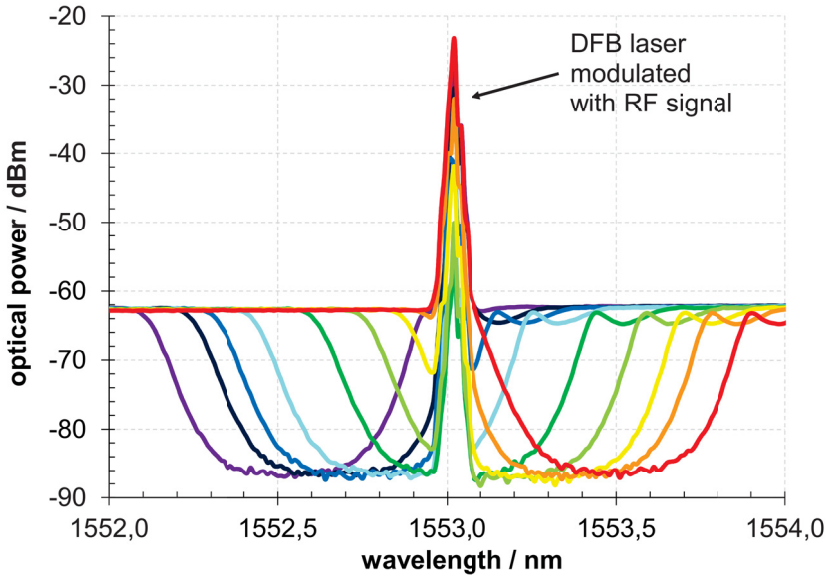

Figure 3.62: Spectra of DFB laser modulated with RF signal for changing spectral characteristic of the optical fiber sensor

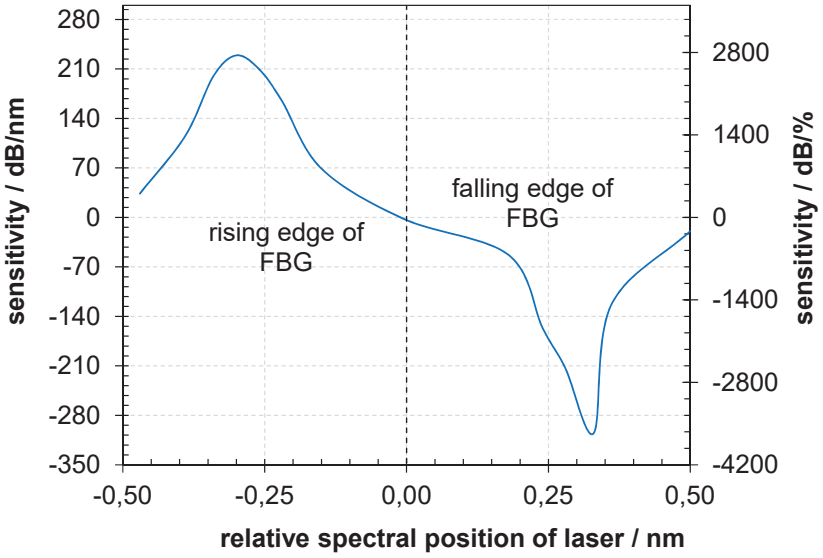

Figure 3.63: Sensitivity depending of the spectral position of the laser with respect to the resonance of the optical fiber sensor

Due to the electronic evaluation, in this microwave photonic system the sensitivity of the sensor scheme not only depends on the sensor itself (i.e. the FBG) but also on the RoF signal. Figure 3.62 implies that the relative spectral position between FBG and laser is the key characteristic. In Figure 3.63 shows the measured sensitivity of the sensor system with respect to the relative spectral position between FBG and laser. When the laser line is centered directly at the resonance of the FBG, the sensitivity is lowest. Higher sensitivity can be achieved at the slopes on both sides of the resonance. Far away from the resonance, the grating has no effect and the sensitivity converges to zero.

Conclusion

In this chapter, a novel approach to wirelessly transmit and evaluate the measurement of optical sensors after reception of the wireless signal in electrical domain has been presented and discussed. In order to suppress effects caused in optical domain and from the wireless channel, a calibration and evaluation procedure working with LF hardware has been presented. Combining photonic and RF techniques enabled a new system design with superior features being a good example for a holistic microwave photonic design approach. The concept is compatible with a variety of optical sensors and may be extended even to a sensor network.

One application example presented was embedding different fiber sensors into carbon concrete composite. A moisture sensor has been introduced and a strain sensor was demonstrated. Future work has to deal with the wireless channel that has been assumed flat so far. Attenuation or dispersive effects during the wireless propagation

through carbon concrete composite may affect the resolution and achievable sensitivity of the sensor system as well as the maximum transmission distance regardless of the proposed calibration with a second transmission. For steel-reinforced concrete, the RF properties are well-known. Carbon concrete composite, however, is expected to behave differently but only few publications exist so far. The conductivity of the carbon fibers is much lower than the one of steel but the carbon fiber mesh has a higher density than the steel reinforcement. Also, less concrete is used for carbon fiber reinforced structures.

3.4 Summary

The use cases discussed in this chapter range from small transmission distances of below one millimeter for chip-level applications to several kilometers for Radio-over-Fiber systems. Also, various ranges of use such as communications, sensors or the generation of RF signals have been covered. Despite of these differences, all these examples share a common approach – an end-to-end electro-optical cross-domain modeling and optimization process. Only this holostic microwave photonic approach ensures an optimal solution superseding the traditional concept where electronics and photonics are developed separately.

4 Future directions

The concepts of microwave photonic systems have the potential to be further developed in different directions. In this chapter, four major trends are discussed. First, the wireless frequencies are supposed to increase up to the sub-terahertz and terahertz region in order to provide more bandwidth, especially for short range communication. The transport and generation of these signals calls for microwave photonic approaches.

Second, microwave photonic methods and concepts could not only be applied to optical carriers at hundreds of THz but also to THz carriers which start to show a behavior that becomes more and more similar to photonics. A waveguide design with low loss such as the optical fiber is crucial here to enable transmission over longer distances.

The integration of optical functionality into semiconductor processes is an important point. Semiconductor manufacturing allows nanometer scales. However, typical optical components (lenses, waveguides, sources, detectors and many more) are much bigger than the respective optical wavelength. This limits the application areas and the performance of these components and makes a co-integration difficult (as known from silicon photonics).

Nanophotonics deals with the behavior and interaction of light in nanometer scales and empowers promising future applications especially containing interaction between electrical and optical domain – one core issue of microwave photonics.

4.1 THz and sub-THz wireless carriers

Analyzing the past and current wireless systems shows two trends: Short-range standards (WiFi) tend to support data rates of around 100 times their wireless (cellular) counterparts. Additionally, the data rates are increasing so that in 2025, data rates of 1 $\mathrm{Tbit/s}$ are expected [47]. The enourmous bandwidth needed to achieve such high data rates is only available above 100 GHz, i.e. in the sub-THz and THz region. For example, around 250 GHz, the atmospheric attenuation is around 0.002 $\mathrm{dB/m}$. Although it is about 10 times as high as the attenuation in fiber for optical frequencies, it can be regarded negligible for short-range communication. Furthermore, the high frequency bands are still available to be assigned for communication applications.

Despite huge efforts for the electronic generation of electrical carriers in the THz and sub-THz frequencies have been made, optical generation of the RF carrier (as discussed in the previous chapter) becomes more and more appealing. Possible concepts involve photonic upconversion using modulators [157], eventually in conjunction with filters [44, 55] or nonlinear effects [129]. The bottleneck is the conversion back from

optical domain to electrical domain. State-of-the-art photodiodes for optical communication operate from DC to a certain upper frequency. Today, such broadband components are limited to around 100 GHz. For microwave photonics, the lower frequencies are not needed, so photomixers that only support a frequency range around the RF carrier frequency [149] are an option. It can be foreseen, that such devices will become a key component in sub-THz and THz microwave photonic systems. It is worth mentioning that decreasing the size of the active area for photodiodes and photomixers for the sake of increasing the maximum frequency is closely connected to integrated optics (see chapter 4.3) and to nanophotonics discussed later in section 4.4.

4.2 Microwave photonic approaches for THz systems

In microwave photonic systems, the RF signal is modulated onto the optical signal in order to be processed and transported in optical domain and to gain advantage of the properties at optical frequencies. However, the available bandwidth at THz frequencies is already sufficient to accomodate today's and future RF signals below 100 GHz. Concepts similar to microwave photonics could be applied, i.e. using simple amplitude modulation and diodes as detectors. Although the physical principles of the sources and detectors are different, the microwave photonic concepts can be easily adapted. First components for these systems such as solid-state LO sources [32] and Schottky diodes as detectors with a large video bandwidth (70 GHz in [136]) become commercially available.

Without proper waveguiding concepts for THz waves, though, they will not become accepted as carriers. At THz frequencies, solutions with heritage in microwave as well as in photonic technologies are promising. Consequently, metal waveguides, fibers and plastic ribbons have been proposed. That means, dielectric as well as conductive connections are researched. For competetiveness with optical solutions, a flexible connection would be advantageous. Moreover, low group velocity dispersion and low loss are the design goals. In [91], a flexible metal ribbon is proposed as THz interconnect with 0.5–1 $\mathrm{dB/cm}$ loss. This is already comparable to today's ribbon waveguides used for optical interconnects in the infrared region (see chapter 3.1). A metallic slit waveguide has been designed and measured with around 0.1 $\mathrm{dB/cm}$ [148]. The plastic fiber (PE wire) used in [23] also has a low attenuation of below 0.1 $\mathrm{dB/cm}$ at 300 GHz. Yet, coupling is difficult and results in a poor coupling efficiency below 20%. Theory [63] implies that with increasing frequency, the reachable attenuation of dielectric waveguide decreases from 0.2 $\mathrm{dB/m}$ at 300 GHz to below 0.05 $\mathrm{dB/m}$ at 700 GHz. Diametral, the attenuation of metallic waveguides increases (10^{-3} $\mathrm{dB/m}$ at 300 GHz vs. up to 1 $\mathrm{dB/m}$ at 700 GHz). As a consequence, for THz systems, dielectric waveguides should be preferred. Nevertheless, the demonstrated waveguides have typically a more than one magnitude higher attenuation than theoretically predicted. This gives space for improvement in the design of the waveguide structure and the used materials.

4.3 Integrated optics

Nowadays, the practical use of microwave photonic systems is often limited by optical parts being only available as discrete component. This only allows bulky setups which are prone to environmental effects. Moreover, tailored solutions are often not possible and the required interfaces (optical coupling as well as electrical connections) frequently limit the performance significantly.

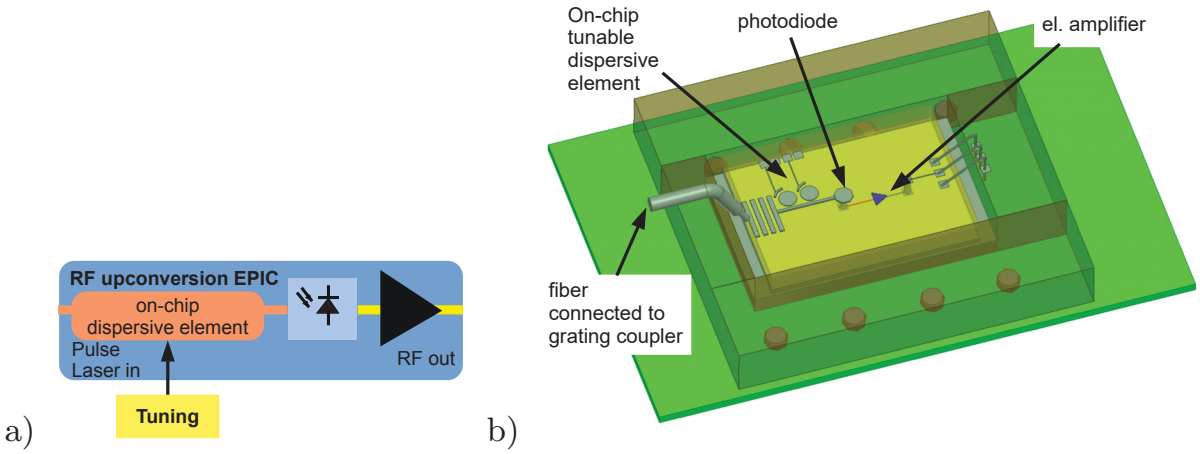

Figure 4.1: Talbot effect based RF upconversion: a) block diagram, b) proposed chip and package.

For the example of photonic RF generation by means of the Talbot effect presented in chapter 3.2.3, an integrated photonics solution would have some major advantages. The dispersive element could be tailored regarding its wavelength dependency enhancing the efficiency especially for spectrally broader sources needed for high upconversion factors and noise suppression. Co-integrating the photodiode for opto-electrical conversion with the optical dispersive element allows higher frequencies to be generated. Moreover, the envisioned on-chip solution (see Figure 4.1) will be small, robust and potentially cost-effective because it can be realized in standard SiGe EPIC technology. This technology has the potential to add further electronic functionality such as amplification, mixers or even complete frontends.

Especially for higher frequencies, a greater level of integration for Radio-over-Fiber and Fiber-to-the-Antenna systems is very appealing. On-chip and in-package antennas become a feasible option so that the functionality of a central station or a base station for these systems can be realized on a single chip. For systems discussed in chapters 3.3.1 and 3.3.2, central stations and base station functionality could be integrated as shown in Figure 4.2. Realizing carrier generation (in the example shown with a ring modulator) as well as data modulation (as Mach-Zehnder modulator in the graphic) on one chip removes loss at optical interfaces. Being in close vicinity, polarization or temperature drift related issues are suppressed. On-chip electronic interfaces between the driver circuits and the modulators can be made more energy-efficient and enhance the supported frequency for the carrier and bandwidth for the

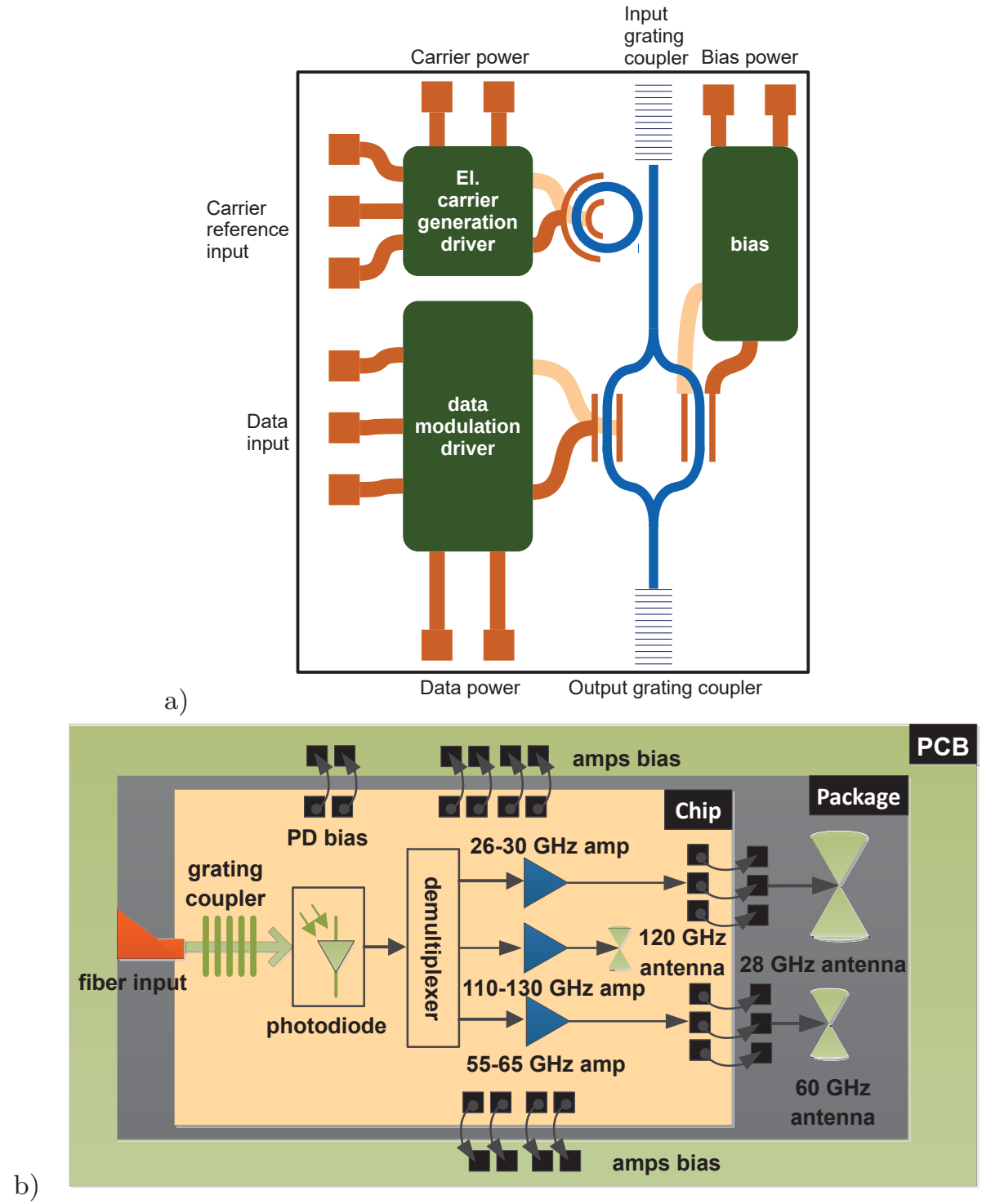

Figure 4.2: Possible electronic-photonic RoF / FTTA solutions: a) central station, b) multi-band base station.

data.
The multi-band base station chip (exemplary shown in Figure 4.2 b)) also carries electronic circuits. This kind of chip would be a key component for an integrated RoF / FTTA system. Multiple frequency bands such as 5G (around 30 GHz), Wireless Gigabit 802.11ad (at 60 GHz) or possible future systems at 120 GHz can be demultiplexed and amplified separately. While at 120 GHz, on-chip antennas will be used, for 60 GHz and 30 GHz in-package solutions are envisioned.

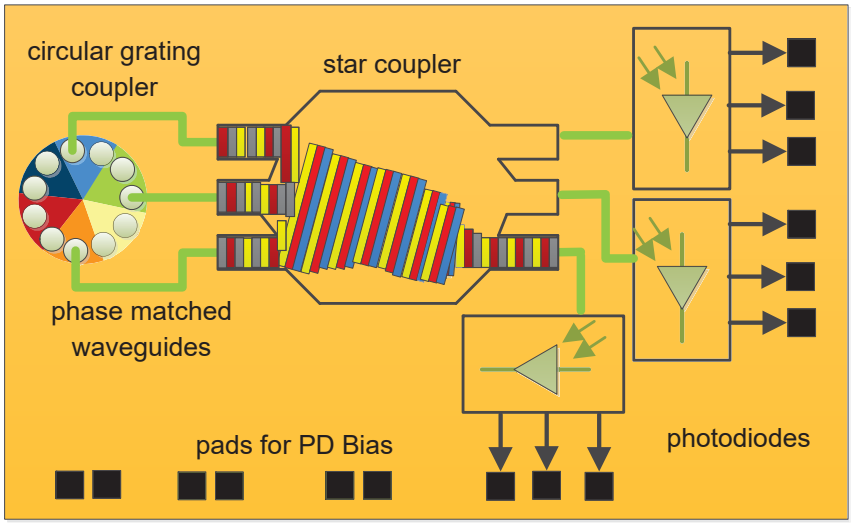

Figure 4.3: Proposed electronic-photonic integrated circuit for optical angular momentum receiver.

Integrated photonic solutions may also help to realize novel concepts, e.g. orbital angular momentum multiplexed transceivers. During the last decade, the optical fiber capacity has been increased by exploiting coherent transmission combined with advanced modulation formats (DP-QPSK, QAM) and the transition from the standard DWDM frequency grid to optical superchannels. However, the transmission capacity of standard optical fiber itself tends to be restricted by the nonlinear Shannon limit. To overcome the possible "capacity crunch", novel techniques on the physical layer are required, capable to provide more effective utilization of the optical fiber links. Therefore, spatial division multiplex (SDM) has attracted significant research interest [121, 165]. Apart from multicore fibers, mode division multiplexing (MDM) can be used [13, 135].
Being free to chose the basis of fiber modes used as orthogonal signal carriers for MDM transmission, vortex modes are an interesting choice [155]. Fibers with a special index profile (vortex fiber) minimize crosstalk between modal channels due to maximized diversity of their effective refraction indices [19, 20, 97]. The demonstrated distances are limited by the residual crosstalk within the interconnect / short-range / access network scenarios, and the scalability of such systems is limited by the fiber design. Anyway, demultiplexing may be achieved with all-optical components without the need for computational complex MIMO processing.

Although OAM-multiplexed optical fiber transmission over relevant distances has already been demonstrated successfully [19, 22], generation, modulation and detection of optical vortices are provided in current systems by bulk optical devices. Industry-scale OAM-based transmission requires robustness and repeatability, which is difficult to achieve with discrete components. Hence, the development of the compact integrated optical components, capable of on-chip generation, transmission and processing of optical vortices, is the next key step towards robust and energy- as well as cost-effective OAM-based information systems [161]. Moreover, the fabrication process of such components should be compatible with the existing microelectronic processes. Silicon photonics allows to manufacture the special optical structures (e.g. circular grating couplers, phase matched waveguides and couplers) as well as the opto-electrical conversion needed for an integrated OAM receiver as shown in Figure 4.3.

4.4 Nanophotonics

Integrating optical elements into microelectronics to an even higher degree than silicon photonics implies nanophotonic approaches [137]. Optical nanoantennas may help to efficiently convert free space optical fields into waveguiding structures and vice versa. The dimensions and feature sizes of such elements are very small, i.e. in the nanometer range. Today, no existing mass-market technology (e.g. photolithography) can provide such structures. Small numbers of samples can be manufactured with insufficient yield using focused ion beams. Also nano-imprinting is an option but has issues in high-volume production [110]. Hence, these technologies are not scalable, therefore new approaches are needed.

One promising option are self-assembly (also refered to as bottom-up) strategies. Based on chemical reactions, millions of nanoscale elements can be manufactured simultaneously. Using DNA as scaffold has the potential to provide arbitrary forms [42, 93]. Nano-particles such as metals, quantum dots, fluorophores and many more can be attached at specific points on the structure composing a sophisticated nanoscale element. This element then has to be attached to the microelectronic circuit at designated places where the macroscopic world is interfaced. Figure 4.4 illustrates the approach. This way, traditional microelectronic manufacturing is linked with self-assembly nanoscale fabrication. This self-assembly approach has the potential to enable easy and cost-effective production of sophisticated elements such as threshold-less nano lasers [66].

Nowadays, nano-structures are already used for example in sensing applications based on surface plasmon resonance (SPR) [57]. The evanescent field of light guided in microscopic waveguides excites SPR depending on the refractive index of the surrounding medium. The refractive index near the surface changes e.g. with biochemical reactions that bind biomolecules on functional groups. Nano-particles enhance this effect [152]. However, random layout of these particles decreases the quality of

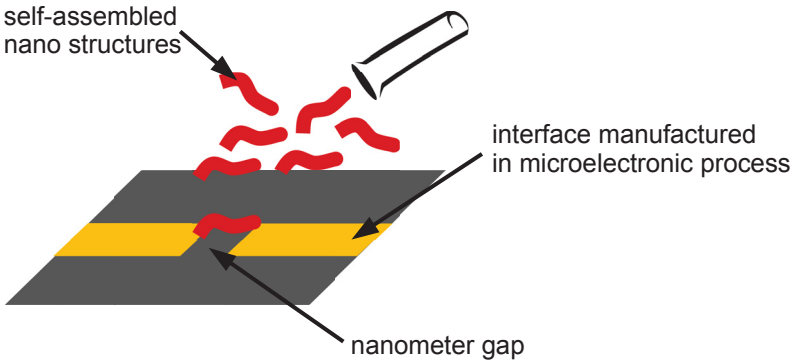

Figure 4.4: Co-integration between self-assembled nano-scale devices and microelectronics.

the SPR due to scattering. The sensivity of the sensor can be improved by applying grating structures [17].

These concepts may be merged by using magnetic core-shell particles carrying the biofunctionalization and arranging them as a grating [53]. This has several advantages: The grating formed by the functionalized nano-particles enhances the sensitivity of the sensor. Second, a mobile substrate like the magnetic core-shell particles can be used within micro-fluidic cells to regenerate the sensor surface. Moreover, the magnetic field that moves and places the nano-particles can also be used to provide different sensing capabilities on demand. Finally, the waveguide design is simplified by having more degrees of freedom due to the flexible substrate. Figure 4.5 shows the setup. The microscopic waveguide supplies the optical signal that is changed due to the SPR interaction with the core-shell particles. The grating structure helps to couple the energy between the surface plasmon wave and the guided mode in the waveguide. Thus, an interface between the nanoscopic world (core-shell particles) and the microscopic world (optical waveguide) is created.

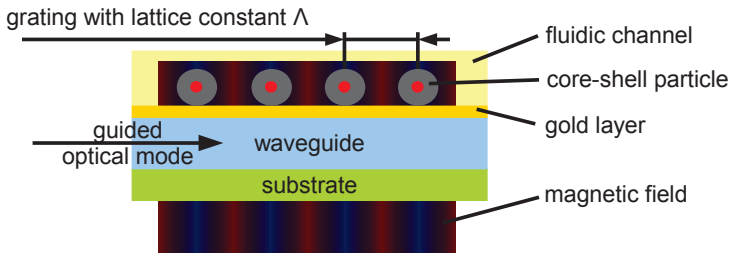

Figure 4.5: Optical biosensor employing dielectric core-shell particles arranged as grating.

Simulations have been carried out [53, 54] and provide first insights to the design constraints for a sensor arrangement as shown in Figure 4.5. In general, the principle has been validated: Changing the lattice constant helps tuning the resonance for

a given waveguide. While pure dielectric nano-particles exhibit a clear resonance, gratings consisting of dielectric-metallic core-shell particles show poor results due to the conduction loss in the metal. This loss prevents the energy to couple efficiently from the guided mode to the surface plasmon wave. Consequently, the effective length of the grating is too short. Anyway, metal is needed for the magnetic behavior. That's why it has to be covered with a sufficiently thick dielectric coating so that the electromagnetic field does not penetrate the metallic core and the particle acts as dielectric. In the future, this kind of core-shell particles can be produced in a bottom-up process and will be used together with the microscopic waveguide and microfluidic system. Depending on the change of refractive index caused by the biochemical reaction that shall be detected, the lattice and waveguide have to be designed.

A second promising application of nanophotonics has also been investigated using simulations [52]. All-optical signal processing may prevent from unnecessary opto-electrical conversions that limit the bandwidth and lower the energy efficiency. Key applications are all-optical switching and all-optical modulation, i.e. one optical signal may directly trigger a change on a second optical signal without any conversion as intermediate step. Photonic antennas are a pivotal component in this scope. Additionally, first nanoantenna samples have been manufacured and a suitable measurement setup has been realized and characterized [51].

A cross-dipole antenna as shown in Figure 4.6 can be used to accomplish this task. The short arm (length l_s) of the antenna is sensitive to the switching or modulating signal at a shorter wavelength λ_s.

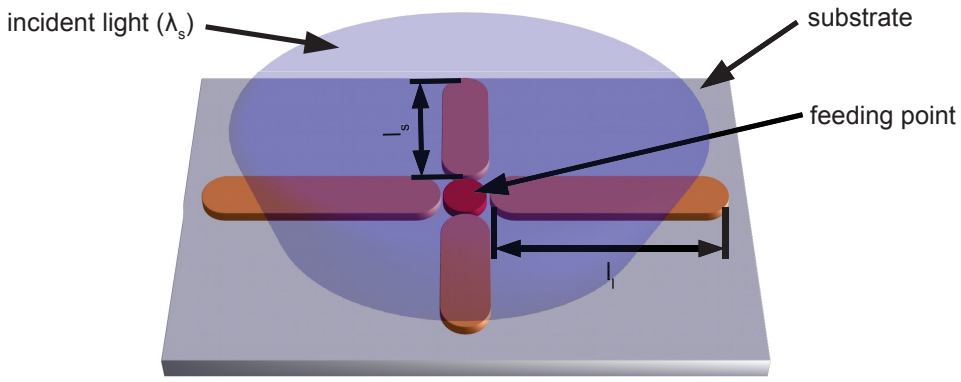

Figure 4.6: Photonic cross-dipole antenna.

The photonic antenna converts the far-field of the incident short wavelength light (λ_S) into a localized near-field. The peak field intensity in the feeding point of the dipole affects the refractive index within the narrow gap. This changes the effective length of the cross dipole arms. However, the simulations indicate that the wavelength shift of the long arm's resonance is more sensitive by orders of magnitude than the one of the short arm. Tuning the resonance of the long arm can be used to switch on or off an optical signal with long wavelength λ_l depending on a short wavelength signal λ_s. Also, amplitude modulation can be carried out the same way (see Figure 4.7).

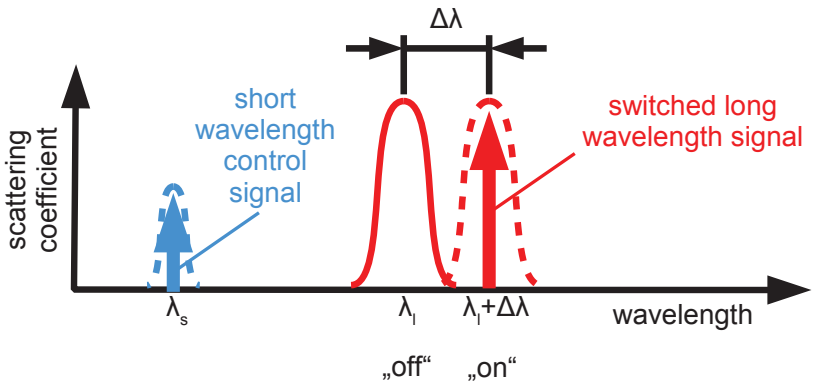

Figure 4.7: Principle of all-optical switching and modulation using nanophotonics: In the presence of the short wavelength control signal, the resonance of the long arm of the photonic antenna shifts by $\Delta\lambda$ switching on the long wavelength signal.

4.5 Summary

Beyond the current applications, microwave photonics will expand in different directions. Driven by advances in technology and the need for higher bandwidths and frequencies, systems operating at sub-THz and THz frequencies will be realized next. Furthermore, the design and system concepts from microwave photonics can be adapted to THz carriers instead of optical ones to a certain extend. Regarding the realization, electronic-photonic integrated circuits and building blocks are starting to become widely available enabling more efficient and powerful microwave photonic systems. For THz bandwidths and a new level of interaction between optical and electrical features, small-scale nanophotonic devices are needed.

5 Conclusion

The hybridization between microwave and optical technologies – microwave photonics – is an emerging field with high potential. Benefitting from the best of both worlds, microwave photonics has many use cases and is just at the beginning of its success story. The availability of a higher degree of integration and new technologies such as silicon photonics paves the way for new concepts, new components and new applications.

With a heritage from communications, system scenarios employing the microwave photonic paradigm are already common today. Radio-over-Fiber is a well-established technique to transport modulated RF signals over fiber. Extending this approach to the device level leads to fiber-coupled antennas in fiber-to-the-antenna configurations. Here, the transmission distance remains in the range of meters to kilometers. For optical intra-chip and inter-chip connections, the spans are much smaller. Yet, microwave photonics helps to provide a broadband channel within and between integrated circuits. Especially for the 3D integration and on interposers, optical TSVs are one key element. Combining optical sensors with microwave photonics extends their fields of application and builds the bridge to the wireless world. Being a powerful general concept, microwave photonics is not limited to today's state-of-the-art. Emerging fields like nanophotonics show lots of options for the application within microwave photonic system concepts.

In this thesis, selected examples for the use of microwave photonic approaches have been presented and discussed. The aim was to cover the whole spectrum of integration – ranging from chip level and board level to system level. Additionally, a cross-section of distinct applications is sampled: communications (point to point as well as networked) and sensing but also important building blocks such as RF generation. It has been shown how the common concepts of microwave photonics are shared among the disparate use cases and how traditional design concepts have to be extended to provide an optimized design. An end-to-end electro-optical modeling and cross-domain (electrical and optical) optimization as demonstrated in this work are inevitable in order to provide optimal solutions.

Based on the findings, it can be stated that microwave photonics is just beginning to spread throughout many fields. These concepts are foreseen to be extended into different directions: First, the frequencies in electrical domain constantly expand towards shorter wavelengths, i.e. millimeter-wave and sub-millimeter wave, or, sub-THz and THz. Second, the proven concepts from optical domain may be re-used for quasi-optical carriers at lower frequencies (THz). For some purposes it might be more interesting to use THz carriers instead of optical ones, when available. In that case, many of the properties known from optical domain are still valid and

mature approaches known from optics can be re-applied. Third, electronic-photonic co-integration and nanophotonics will be the next fields where a deep interaction of optical and electrical features will drastically enhance the usability which requires microwave photonic solutions also in this small scale devices.

Bibliography

[1] M. S. Ab-Rahman and M. R. Hassan. Turn-on time delay of uncooled semiconductor laser diode subject to external optical feedback: Theoretical analysis. In *Computer Technology and Development, 2009. ICCTD'09. International Conference on*, volume 1, pages 53–57. IEEE, 2009.

[2] Z. Al-Husseini. *Channel characterization in wireless mm-wave communication and Radio-over-Fiber systems*. PhD thesis, TU Dresden, 2015.

[3] Z. Al-Husseini, N. Neumann, and D. Plettemeier. A 60 GHz Radio-over-Fiber System Performance Analysis for Different Data Modulation Formats. In *International Students and Young Scientists Workshop "Photonics and Microsystems"*, St Marienthal, Germany, 2013.

[4] Z. Al-Husseini, N. Neumann, and D. Plettemeier. Digital Carrier Recovery Algorithm Simulation of 60 GHz RoF system. In *Photonic Networks, 14. 2013 ITG Symposium. Proceedings*, pages 1–6, 2013.

[5] Z. Al-Husseini, N. Neumann, and D. Plettemeier. Residual carrier influence on system performance of a 60 GHz Radio over Fiber system. In *Optical Wireless Communications (IWOW), 2013 2nd International Workshop on*, pages 89–93. IEEE, 2013.

[6] Z. Al-Husseini, N. Neumann, and D. Plettemeier. Estimation and equalization techniques applied to Radio over Fiber System. In *Advances in Wireless and Optical Communications (RTUWO), 2015*, pages 30–33, Nov 2015.

[7] S. Arahira et al. Repetition-Frequency Multiplication of Mode-Locked Pulses Using Fiber Dispersion. *Journal of Lightwave Technology*, 16(3), 1998.

[8] J. Azana et al. Frequency shifting of microwave signals by use of a general temporal self-imaging (Talbot) effect in optical fibers. *Optics Letters*, 29(24), 2004.

[9] J. Azana and M. A. Muriel. Temporal Self-Imaging Effects: Theory and Application for Multiplying Pulse Repetition Rates. *IEEE Journal of Selected Topics in Quantum Electronics*, 7(4), 2001.

[10] M. S. Bakir, C. King, D. Sekar, H. Thacker, B. Dang, G. Huang, A. Naeemi, and J. D. Meindl. 3D heterogeneous integrated systems: liquid cooling, power delivery, and implementation. In *Custom Integrated Circuits Conference, 2008. CICC 2008. IEEE*, pages 663–670. IEEE, 2008.

[11] C. A. Balanis. *Antenna Theory: Analysis and Design*. Wiley, 2012.

[12] R. Beausoleil, J. Ahn, N. Binkert, A. Davis, D. Fattal, M. Fiorentino, N. P. Jouppi, M. McLaren, C. M. Santori, R. S. Schreiber, et al. A nanophotonic interconnect for high-performance many-core computation. In *Integrated Photonics and Nanophotonics Research and Applications*. Optical Society of America, 2008.

[13] S. Berdagué and P. Facq. Mode division multiplexing in optical fibers. *Applied optics*, 21(11):1950–1955, 1982.

[14] K. Bergman. Invited talk: Nanophotonic interconnection networks for performance-energy optimized computing. In *Microelectronics and Electron Devices (WMED), 2012 IEEE Workshop on*, April 2012.

[15] W. Bogaerts, P. De Heyn, T. Van Vaerenbergh, K. De Vos, S. Kumar Selvaraja, T. Claes, P. Dumon, P. Bienstman, D. Van Thourhout, and R. Baets. Silicon microring resonators. *Laser & Photonics Reviews*, 6(1):47–73, 2012.

[16] W. Bogaerts, P. Dumon, D. Van Thourhout, and R. Baets. Low-loss, low-cross-talk crossings for silicon-on-insulator nanophotonic waveguides. *Optics letters*, 32(19):2801–2803, 2007.

[17] N. Bonod, E. Popov, and R. C. McPhedran. Increased surface plasmon resonance sensitivity with the use of double Fourier harmonic gratings. *Optics express*, 16(16):11691–11702, 2008.

[18] S. Borkar. 3D integration for energy efficient system design. In *Proceedings of the 48th Design Automation Conference*, pages 214–219. ACM, 2011.

[19] N. Bozinovic, Y. Yue, Y. Ren, M. Tur, P. Kristensen, H. Huang, A. E. Willner, and S. Ramachandran. Terabit-scale orbital angular momentum mode division multiplexing in fibers. *science*, 340(6140):1545–1548, 2013.

[20] C. Brunet, B. Ung, L. Wang, Y. Messaddeq, S. LaRochelle, and L. A. Rusch. Design of a family of ring-core fibers for OAM transmission studies. *Optics express*, 23(8):10553–10563, 2015.

[21] L. Brusberg, S. Whalley, R. C. A. Pitwon, F. R. Faridi, and H. Schröder. Large optical backplane with embedded graded-index glass waveguides and fiber-flex termination. *Journal of Lightwave Technology*, 34(10):2540–2551, 2016.

[22] J. A. Carpenter, B. C. Thomsen, and T. D. Wilkinson. Optical vortex based mode division multiplexing over graded-index multimode fibre. In *Optical Fiber Communication Conference*. Optical Society of America, 2013.

[23] L. J. Chen, H. W. Chen, T. F. Kao, J. Y. Lu, and C. K. Sun. Low-loss subwavelength plastic fiber for terahertz waveguiding. *Optics Letters*, 31(3):308–310, 2006.

[24] X. Chen, A. Al Amin, A. Li, and W. Shieh. *Optical Fiber Telecommunications VIB: Chapter 8. Multicarrier Optical Transmission*. Elsevier, 2013.

[25] X. Chen et al. Photonic Generation of Microwave Signal Using a Dual-Wavelength Single-Longitudinal-Mode Fiber Ring Laser. *IEEE Transactions on Microwave Theory and Techniques*, 54(2), 2006.

[26] M. Chin and W. S. Chang. Theoretical design optimization of multiple-quantum-well electroabsorption waveguide modulators. *IEEE journal of quantum electronics*, 29(9):2476–2488, 1993.

[27] C. W. Chow, F. M. Kuo, J. W. Shi, C. H. Yeh, Y. F. Wu, C. H. Wang, Y. T. Li, and C. L. Pan. 100 GHz ultra-wideband (UWB) fiber-to-the-antenna (FTTA) system for in-building and in-home networks. *Optics express*, 18(2):473–478, 2010.

[28] B. Ciftcioglu, R. Berman, S. Wang, J. Hu, I. Savidis, M. Jain, D. Moore, M. Huang, E. G. Friedman, G. Wicks, et al. 3-D integrated heterogeneous intra-chip free-space optical interconnect. *Optics express*, 20(4):4331–4345, 2012.

[29] B. Ciftcioglu, R. Berman, J. Zhang, Z. Darling, S. Wang, J. Hu, J. Xue, A. Garg, M. Jain, I. Savidis, et al. A 3-D integrated intrachip free-space optical interconnect for many-core chips. *IEEE Photonics Technology Letters*, 23(3):164–166, 2011.

[30] B. Ciftcioglu, J. Gao, R. Berman, M. Jain, D. Moore, G. Wicks, M. Huang, E. G. Friedman, and H. Wu. Recent progress on 3-D integrated intra-chip free-space optical interconnect. In *Optical Interconnects Conference, 2012 IEEE*, pages 56–57. IEEE, 2012.

[31] J. L. Corral, J. Marti, S. Regidor, J. M. Foster, R. Laming, and M. J. Cole. Continuously variable true time-delay optical feeder for phased-array antenna employing chirped fiber grating. *IEEE Transactions on Microwave Theory and Techniques*, 45(8):1531–1536, 1997.

[32] T. W. Crowe, J. L. Hesler, S. A. Retzloff, C. Pouzou, and G. S. Schoenthal. Solid-state LO sources for greater than 2 THz. In *22nd Int. Symp. Space Terahertz Technol*, pages 209–212, 2011.

[33] J. E. Cunningham, A. V. Krishnamoorthy, R. Ho, I. Shubin, H. Thacker, J. Lexau, D. C. Lee, D. Feng, E. Chow, Y. Luo, et al. Integration and packaging of a macrochip with silicon nanophotonic links. *IEEE Journal of Selected Topics in Quantum Electronics*, 17(3):546–558, 2011.

[34] N. Daix, E. Uccelli, L. Czornomaz, D. Caimi, C. Rossel, M. Sousa, H. Siegwart, C. Marchiori, J. M. Hartmann, K. T. Shiu, et al. Towards large size substrates for III-V co-integration made by direct wafer bonding on Si. *APL Materials*, 2(8):086104, 2014.

[35] J. Damas, N. Neumann, and D. Plettemeier. Cost effective printed circuit board intermediate frequency over fiber central station. *International Journal of Microwave and Optical Technology*, 10(6), November 2015.

[36] J. Damas, N. Neumann, and D. Plettemeier. Printed circuit board intermediate frequency over fiber central station. In *ISMOT2015, 15th International Symposium on Microwave and Optical Technology*, Dresden, Germany, 29.Jun.-01.Jul. 2015.

[37] A. Demir et al. Phase noise in Oscillators: A Unifying Theory and Numerical Methods for Characterization. *IEEE Transactions on Circuits and Systems I: Fundamental Theory and Applications*, 47(5), 2000.

[38] F. Devaux, Y. Sorel, and J. F. Kerdiles. Simple measurement of fiber dispersion and of chirp parameter of intensity modulated light emitter. *IEEE Journal of Lightwave Technology*, 11(12):1937–1940, 1993.

[39] D. C. S. Dumas, K. Gallacher, S. Rhead, M. Myronov, D. R. Leadley, and D. J. Paul. Ge/SiGe quantum confined Stark effect electro-absorption modulation with low voltage swing at $\lambda=$ 1550 nm. *Optics express*, 22(16):19284–19292, 2014.

[40] I. M. Elfadel and G. Fettweis. *3D Stacked Chips: From Emerging Processes to Heterogeneous Systems*. Springer International Publishing, 2016.

[41] T. Erdogan. Fiber grating spectra. *Journal of Lightwave Technology*, 15(8):1277–1294, 1997.

[42] C. Erler, K. Günther, and M. Mertig. Photo-induced synthesis of DNA-templated metallic nanowires and their integration into micro-fabricated contact arrays. *Applied Surface Science*, 255(24):9647–9651, 2009.

[43] W. J. Fang, X. G. Huang, K. Yang, and X. M. Zhang. Full duplex dense-wavelength-division-multiplexing radio-over-fiber system transmission of 75-GHz W-band frequency multiple-input multiple-output orthogonal-frequency-division-multiplexing signals with 3$\times$ 12 Gbps downstream and 6 Gbps upstream. *Optical Engineering*, 51(9):095004–1, 2012.

[44] F. Ferdous, H. Miao, D. E. Leaird, K. Srinivasan, J. Wang, L. Chen, L. T. Varghese, and A. M. Weiner. Spectral line-by-line pulse shaping of on-chip microresonator frequency combs. *Nature Photonics*, 5(12):770–776, 2011.

[45] C. R. Fernández-Pousa and F. Mateos. Timing jitter smoothing by Talbot effect. I. Variance. *J. Opt. Soc. Am. B*, 21(6), 2004.

[46] C. R. Fernández-Pousa and F. Mateos. Timing jitter smoothing by Talbot effect. II. Intensity Spectrum. *J. Opt. Soc. Am. B*, 22(4), 2005.

[47] G. Fettweis, R. Irmer, P. Zillmann, U. Barth, E. Kühn, K. Strohm, R. Kraemer, E. Grass, G. Tränkle, U. Trautwein, et al. System concept for 1 Gbit/ s and beyond. *Tutorial IEEE 802 Plenary*, 2005.

[48] I. González Insua, D. Plettemeier, and C. G. Schäffer. Simple remote heterodyne radio-over-fiber system for gigabit per second wireless access. *Journal of Lightwave Technology*, 28(16):2289–2295, 2010.

[49] B. W. Hakki. Evaluation of transmission characteristics of chirped DFB lasers in dispersive optical fiber. *IEEE Journal of Lightwave Technology*, 10(7):964–970, 1992.

[50] S. E. Hamran, T. Berger, L. Hanssen, M. J. Oyan, V. Ciarletti, C. Corbel, and D. Plettemeier. A prototype for the WISDOM GPR on the ExoMars mission. In *Advanced Ground Penetrating Radar, 2007 4th International Workshop on*, pages 252–255. IEEE, 2007.

[51] T. Haugwitz, J. W. Erben, N. Neumann, D. Reuter, and D. Plettemeier. Plasmonic dipole nanoantennas on a SiO2/Si substrate and their characterization. In *SPIE Photonics Europe 2018*, Strasbourg, France, 23.-26.Apr. 2018.

[52] T. Haugwitz, N. Neumann, and D. Plettemeier. Tunable optical cross-dipole antenna. In *ISMOT2015, 15th International Symposium on Microwave and Optical Technology*, Dresden, Germany, 29.Jun.-01.Jul. 2015.

[53] T. Haugwitz, N. Neumann, T. Schuster, and D. Plettemeier. Advanced planar-optical SPR based biosensor using magnetic-dielectric core-shell-particles as mobile substrate. In *2013 IEEE Sensors*, pages 1–4. IEEE, 2013.

[54] T. Haugwitz, T. Schuster, N. Neumann, and D. Plettemeier. Simulation of submicrometer photonic structures using high performance computing. In *Problems of technics and technology of telecommunications (PTT) / Optical Technology in Telecommunications (OTT) 2012*, Ufa, Russia, 21.-24. Nov. 2012.

[55] K. P. Ho and J. M. Kahn. Optical frequency comb generator using phase modulation in amplified circulating loop. *IEEE Photonics Technology Letters*, 5(6):721–725, 1993.

[56] J. Hofrichter, O. Raz, S. Keyvaninia, T. de Vries, H. J. S. Dorren, T. Morf, and B. J. Offrein. High-speed direct-modulation of InP microdisk lasers. In *39th European Conference and Exhibition on Optical Communication (ECOC-2013)*, 2013.

[57] J. Homola and M. Piliarik. *Surface plasmon resonance (SPR) sensors*. Springer, 2006.

[58] R. Hui and M. O'Sullivan. *Fiber Optic Measurement Techniques*. Elsevier Science, 2009.

[59] S. K. Hwang, J. M. Liu, and J. K. White. 35-GHz intrinsic bandwidth for direct modulation in 1.3-μm semiconductor lasers subject to strong injection locking. *IEEE Photonics Technology Letters*, 16(4):972–974, 2004.

[60] B. Jalali, V. Raghunathan, D. Dimitropoulos, and O. Boyraz. Raman-based silicon photonics. *IEEE Journal of Selected Topics in Quantum Electronics*, 12(3):412–421, 2006.

[61] S. W. James, R. P. Tatam, et al. Optical fibre long-period grating sensors: characteristics and application. *Measurement Science and Technology*, 14(5):R49–R61, 2003.

[62] T. Jannson and J. Jannson. Temporal self-imaging effect in single-mode fibers. *J. Opt. Soc. Am.*, 71(11), 1981.

[63] Y. Jiang, C. Jing, W. A. Peebles, D. L. Brower, and J. L. Doane. Improved performance of an optically pumped FIR laser using metallic waveguide". *Review of Scientific Instruments*, 63(10):4672–4674, 1992.

[64] I. Kaminow, T. Li, and A. E. Willner, editors. *Optical fiber telecommunications VA: Components and Subsystems*, chapter Polarization Mode Dispersion, pages 605–670. Elsevier, 2010.

[65] J. U. Kang et al. Demonstration of microwave frequency shifting by use of a highly chirped mode-locked fiber laser. *Optics Letters*, 23(15), 1998.

[66] M. Khajavikhan, A. Simic, M. Katz, J. H. Lee, B. Slutsky, A. Mizrahi, V. Lomakin, and Y. Fainman. Thresholdless nanoscale coaxial lasers. *Nature*, 482(7384):204–207, 2012.

[67] S. Killge, S. Charania, K. Richter, N. Neumann, Z. Al-Husseini, D. Plettemeier, and J. Bartha. Realization of optical multimode TSV waveguides for Si-Interposer in 3D-chip-stacks. In *Micro-structured and Specialty Optical Fibres V*, volume 10232, page 102320T. International Society for Optics and Photonics, 2017.

[68] J. Kim and J. F. Buckwalter. A 40-Gb/s optical transceiver front-end in 45 nm SOI CMOS. *Solid-State Circuits, IEEE Journal of*, 47(3):615–626, 2012.

[69] J. S. Kim, J. W. Kang, and J. J. Kim. Simple and low cost fabrication of thermally stable polymeric multimode waveguides using a UV-curable epoxy. *Japanese journal of applied physics*, 42:1277, 2003.

[70] R. Kirchner, A. Finn, R. Landgraf, L. Nueske, L. Teng, M. Vogler, and W. J. Fischer. Direct UV-Imprinting of Hybrid-Polymer Photonic Microring Resonators and Their Characterization. *Journal of Lightwave Technology*, 32(9):1674–1681, 2014.

[71] C. Knochenhauer, S. Hauptmann, C. Scheytt, and F. Ellinger. A compact, low-power 40 Gbit/s differential laser driver in SiGe BiCMOS technology. In *Microwave Integrated Circuits Conference, 2009. EuMIC 2009. European*, pages 324–326. IEEE, 2009.

[72] C. Knochenhauer, C. Scheytt, and F. Ellinger. A compact, low-power 40-Gbit/s modulator driver with 6-V differential output swing in 0.25-μm SiGe BiCMOS. *Solid-State Circuits, IEEE Journal of*, 46(5):1137–1146, 2011.

[73] R. Krähenbühl, T. Lamprecht, E. Zgraggen, F. Betschon, and A. Peterhans. High-precision, self-aligned, optical fiber connectivity solution for single-mode waveguides embedded in optical PCBs. *Journal of Lightwave Technology*, 33(4):865–871, 2015.

[74] J. H. Lau. TSV manufacturing yield and hidden costs for 3D IC integration. In *Electronic Components and Technology Conference (ECTC), 2010 Proceedings 60th*, pages 1031–1042. IEEE, 2010.

[75] J. H. Lau. Recent advances and new trends in nanotechnology and 3D integration for semiconductor industry. In *3D Systems Integration Conference (3DIC), 2011 IEEE International*, pages 1–23. IEEE, 2012.

[76] M. J. Lee, H. S. Kang, K. H. Lee, and W. Y. Choi. Fiber-fed 60-GHz self-heterodyne system using a self-oscillating harmonic optoelectronic mixer based on a CMOS-compatible APD. In *Microwave Symposium Digest, 2008 IEEE MTT-S International*, pages 587–590. IEEE, 2008.

[77] L. Li, P. Su, J. Xue, M. Brillhart, J. Lau, P. J. Tzeng, C. K. Lee, C. J. Zhan, M. J. Dai, H. C. Chien, et al. Addressing bandwidth challenges in next generation high performance network systems with 3D IC integration. In *Electronic Components and Technology Conference (ECTC), 2012 IEEE 62nd*, pages 1040–1046. IEEE, 2012.

[78] D. Liang and J. E. Bowers. Recent progress in lasers on silicon. *Nature Photonics*, 4(8):511–517, 2010.

[79] R. A. Linke. Transient chirping in single-frequency lasers: lightwave systems consequences. *Electronics Letters*, 20(11):472–474, 1984.

[80] J. Liu, M. Beals, A. Pomerene, S. Bernardis, R. Sun, J. Cheng, L. C. Kimerling, and J. Michel. Waveguide-integrated, ultralow-energy GeSi electro-absorption modulators. *Nature Photonics*, 2(7):433, 2008.

[81] J. Liu, R. Camacho-Aguilera, J. T. Bessette, X. Sun, X. Wang, Y. Cai, L. C. Kimerling, and J. Michel. Ge-on-Si optoelectronics. *Thin Solid Films*, 520(8):3354–3360, 2012.

[82] J. Liu et al. Single longitudinal mode multi-wavelength fiber ring laser. *IEEE Photonics Technology Letters*, 16(4), 2004.

[83] J. Liu, X. Sun, R. Camacho-Aguilera, L. C. Kimerling, and J. Michel. Ge-on-Si laser operating at room temperature. *Optics letters*, 35(5):679–681, 2010.

[84] A. Loayssa and F. J. Lahoz. Broad-band RF photonic phase shifter based on stimulated Brillouin scattering and single-sideband modulation. *IEEE Photonics Technology Letters*, 18(1):208–210, 2006.

[85] L. Lorenz, K. Nieweglowski, Z. Al-Husseini, N. Neumann, D. Plettemeier, K.-J. Wolter, T. Reitberger, J. Franke, and K. Bock. Asymmetric optical bus coupler for interruption-free short-range connections on board and module level. *Journal of Lightwave Technology*, 35(18):4033–4039, 2017.

[86] J. A. Lott, A. S. Payusov, S. A. Blokhin, P. Moser, N. N. Ledentsov, and D. Bimberg. Arrays of 850 nm photodiodes and vertical cavity surface emitting lasers for 25 to 40 Gbit/s optical interconnects. *physica status solidi (c)*, 9(2):290–293, 2012.

[87] R. Ludwig and A. Ehrhardt. Turn-key-ready wavelength-, repetition rate and pulsewidth-tunable femtosecond hybrid modelocked semiconductor laser. *Electronics Letters*, 31(14), 1995.

[88] A. Łysiuk, K. Godziszewski, Y. Yashchyshyn, and J. Modelski. Design and Investigation of Photonic Remote Antenna Units for Bidirectional Transmission in the Last Mile Wireless over Fiber System. *Radioengineering*, 22(4):1239, 2013.

[89] R. McIntyre. Multiplication noise in uniform avalanche diodes. *IEEE Transactions on Electron Devices*, 13(1):164–168, 1966.

[90] S. Meister, M. Grehn, H. Rhee, M. Vitali, C. Theiss, S. Kupijai, A. Al-Saadi, D. Bronzi, S. Otte, M. Henniges, D. Selicke, M. Atif, E. Schwartz, S. Lischke, D. Stolarek, A. Mai, M. Kaynak, H. H. Richter, and L. Zimmermann. Silicon photonics for 100 Gbit/s intra-data center optical interconnects. volume 9753, pages 975308–975308–7, 2016.

[91] R. Mendis and D. Grischkowsky. THz interconnect with low-loss and low-group velocity dispersion. *Microwave and Wireless Components Letters, IEEE*, 11(11):444–446, 2001.

[92] C. Merckling, N. Waldron, S. Jiang, W. Guo, N. Collaert, M. Caymax, E. Vancoille, K. Barla, A. Thean, M. Heyns, et al. Heteroepitaxy of InP on Si (001) by selective-area metal organic vapor-phase epitaxy in sub-50 nm width trenches: The role of the nucleation layer and the recess engineering. *Journal of Applied Physics*, 115(2):023710, 2014.

[93] M. Mertig, L. Colombi Ciacchi, R. Seidel, W. Pompe, and A. De Vita. DNA as a selective metallization template. *Nano Letters*, 2(8):841–844, 2002.

[94] R. Morris and A. K. Kodi. Exploring the design of 64-and 256-core power efficient nanophotonic interconnect. *Selected Topics in Quantum Electronics, IEEE Journal of*, 16(5):1386–1393, 2010.

[95] P. Moser, W. Hofmann, P. Wolf, J. A. Lott, G. Larisch, A. Payusov, N. N. Ledentsov, and D. Bimberg. 81 fJ/bit energy-to-data ratio of 850 nm vertical-cavity surface-emitting lasers for optical interconnects. *Applied Physics Letters*, 98(23):231106, 2011.

[96] N. F. Nanyan, R. Ngah, T. Prakoso, Y. Rahayu, and T. A. Rahman. An active downlink photonic antenna. In *Photonics (ICP), 2010 International Conference on*, pages 1–5. IEEE, 2010.

[97] R. M. Nejad, K. Allahverdyan, P. Vaity, S. Amiralizadeh, C. Brunet, Y. Messaddeq, S. LaRochelle, and L. A. Rusch. Mode division multiplexing using orbital angular momentum modes over 1.4-km ring core fiber. *Journal of Lightwave Technology*, 34(18):4252–4258, 2016.

[98] N. Neumann, Z. Al-Husseini, and D. Plettemeier. Nonlinearity, noise and bandwidth influence for PAM4 modulation format. In *19. ITG Fachtagung Photonische Netze*, Leipzig, Germany, 11.-12.Jun. 2018.

[99] N. Neumann, S. Charania, S. Killge, Z. al Husseini, R. Henker, F. Ellinger, J. Bartha, and D. Plettemeier. Modeling and characterization of optical TSVs. In *Optical Fibers and Their Applications 2017*, volume 10325. International Society for Optics and Photonics, 2017.

[100] N. Neumann, S. Frach, and D. Plettemeier. Active Integrated Fiber-Coupled Receiving Antenna. In *2013 Loughborough Antennas & Propagation Conference (LAPC 2013)*, Burleigh Court International Conference Centre, Loughborough University, United Kingdom, Nov. 2013.

[101] N. Neumann, M. Haas, and D. Plettemeier. DE10201002976.9, Verfahren und Anordnung zur Erzeugung einer elektromagnetischen Schwingung in einem hohen Frequenzbereich, 17. Mar. 2010.

[102] N. Neumann, M. Haas, D. Plettemeier, and C. G. Schäffer. Talbot effect supported millimeter wave generation. In *18th International Conference on Microwave Radar and Wireless Communications (MIKON)*, Vilnius, Lithuania, 14.-16. Jun. 2010.

[103] N. Neumann, M. Jenning, and D. Plettemeier. Millimeter wave generation with increased efficiency using the temporal talbot effect. In *2011 International Conference on Electromagnetics in Advanced Applications (ICEAA)*, pages 371–373, Torino, Italy, 12.-17. Sep. 2011. IEEE.

[104] N. Neumann, T. Schuster, and D. Plettemeier. Novel approach for simultaneous wireless transmission and evaluation of optical sensors (invited). In *Photonics Asia*. International Society for Optics and Photonics, 2014.

[105] N. Neumann, T. Schuster, D. Plettemeier, E. Häntzsche, and A. Nocke. Wireless read-out of optical fiber sensors. In *Proceedings Sensor*, 2017.

[106] N. Neumann, R. Trieb, W. S. Benedix, and D. Plettemeier. Active Integrated Photonic Antenna Array. In *2012 IEEE-APS Topical Conference on Antennas and Propagation in Wireless Communications (APWC)*, pages 648–651, Cape Town, South Africa, 2.-7. Sep. 2012.

[107] N. Neumann, R. Trieb, S. Frach, and D. Plettemeier. FTTA System Demo Using Optical Fiber-Coupled Active Antennas. *Photonics*, 1(3):198–210, 2014.

[108] N. Neumann, R. Trieb, and D. Plettemeier. Remotely Operated Active Integrated Photonic Antenna Array. In *2012 Loughborough Antennas & Propagation Conference (LAPC 2012)*, Burleigh Court International Conference Centre, Loughborough University, United Kingdom, Nov. 2012.

[109] W. Ng, A. A. Walston, G. L. Tangonan, J. J. Lee, I. L. Newberg, and N. Bernstein. The first demonstration of an optically steered microwave phased array antenna using true-time-delay. *IEEE Journal of Lightwave Technology*, 9(9):1124–1131, 1991.

[110] Y. Ofir, I. W. Moran, C. Subramani, K. R. Carter, and V. M. Rotello. Nanoimprint lithography for functional three-dimensional patterns. *Advanced Materials*, 22(32):3608–3614, 2010.

[111] R. Olshansky, P. Hill, V. Lanzisera, and W. Powazinik. Frequency response of 1.3 μm InGaAsP high speed semiconductor lasers. *Quantum Electronics, IEEE Journal of*, 23(9):1410–1418, 1987.

[112] Oplink. OFMS Series Full 2x2 Optical Fiber Switches. Technical report, 2009.

[113] M. Otto, F. Michael, T. Duthel, and C. G. Schäffer. Flexible manufacturing method for long-period fibre gratings with arbitrary index modulation profiles. In *Proceedings of 2002 IEEE/LEOS Workshop on Fibre and Optical Passive Components, 2002.*, pages 6–11. IEEE, 2002.

[114] S. Pan and J. Yao. A UWB over fiber system compatible with WDM-PON architecture. *IEEE Photonics Technology Letters*, 22(20):1500–1502, 2010.

[115] M. S. Parekh, P. A. Thadesar, and M. S. Bakir. Electrical, optical and fluidic through-silicon vias for silicon interposer applications. In *Electronic Components and Technology Conference (ECTC), 2011 IEEE 61st*, pages 1992–1998. IEEE, 2011.

[116] R. Paschotta. Noise of mode-locked lasers (Part I): numerical model. *Applied Physics B: Lasers and Optics*, 79(2), 2004.

[117] R. Paschotta. Noise of mode-locked lasers (Part II): timing jitter and other fluctuations. *Applied Physics B: Lasers and Optics*, 79(2), 2004.

[118] J. Peupelmann, M. Otto, K. Schuh, and C. G. Schäffer. Enhanced performance of fiber Bragg grating sensors. In *Proceedings of SPIE, the International Society for Optical Engineering*, volume 4185, pages 736–739. Society of Photo-Optical Instrumentation Engineers, 2000.

[119] D. Pudo and L. R. Chen. Simple estimation of pulse amplitude noise and timing jitter evolution through the temporal Talbot effect. *Optics Express*, 15(10), 2007.

[120] G. Qi et al. Optical generation and transmission of wideband, continuously tunable millimeter-wave signals. *IEEE Transactions on Microwave Theory and Techniques*, 53(10), 2005.

[121] D. Richardson, J. Fini, and L. Nelson. Space-division multiplexing in optical fibres. *Nature Photonics*, 7(5):354, 2013.

[122] W. P. Robins. *Phase Noise in Signal Sources*. IET, 1984.

[123] C. G. Schäffer and M. Sauer. Fiber Transmission Behavior of Millimeter-Wave-Electro-Optical Upconversion Systems with Transmitter Chirp. *Proceedings of the European Microwave Association*, 3:190–200, September 2007.

[124] T. Schneider, M. Junker, and D. Hannover. Generation of millimetre-wave signals by stimulated brillouin scattering for radio over fibre systems. *Electronics Letters*, 40(23):1500–1502, 2004.

[125] T. Schuster, R. Herschel, N. Neumann, and C. G. Schäffer. Miniaturized long-period fiber grating assisted surface plasmon resonance sensor. *Journal of Lightwave Technology*, 30(8):1003–1008, 2012.

[126] T. Schuster, R. Landgraf, A. Finn, M. Mertig, G. Gerlach, and K. J. Wolter. Biosensing with Optical Waveguides. In *Bio and Nano Packaging Techniques for Electron Devices*, pages 557–579. Springer Berlin Heidelberg, 2012.

[127] T. Schuster, N. Neumann, D. Plettemeier, R. Korbitz, and A. Richter. A fiber-optic ph sensor with wireless radio over fiber read-out. In *SENSORS, 2015 IEEE*, pages 1–4, Nov 2015.

[128] T. Schuster, C. G. Schäffer, M. Mertig, M. Bonsch, and D. Plettemeier. Fiber grating-assisted investigation on surface plasmon resonance of fiber cladding modes. In *2012 IEEE Sensors*, pages 1–4, Oct 2012.

[129] G. A. Sefler and K. I. Kitayama. Frequency comb generation by four-wave mixing and the role of fiber dispersion. *Journal of lightwave technology*, 16(9):1596, 1998.

[130] A. Shacham, K. Bergman, and L. P. Carloni. Photonic networks-on-chip for future generations of chip multiprocessors. *Computers, IEEE Transactions on*, 57(9):1246–1260, 2008.

[131] A. Shakoor, K. Nozaki, E. Kuramochi, K. Nishiguchi, A. Shinya, and M. Notomi. Ultra-Low Energy 1D Silicon Photonic Crystal Electro-Optic Modulator with Sub-100-mV Switching Voltage. In *Integrated Photonics Research, Silicon and Nanophotonics*, pages IW3A–6. Optical Society of America, 2014.

[132] L. Y. Shao, M. J. Yin, H. Y. Tam, and J. Albert. Fiber Optic pH Sensor with Self-Assembled Polymer Multilayer Nanocoatings. *Sensors*, 13(2):1425–1434, 2013.

[133] V. Sittakul and M. J. Cryan. A fully bidirectional 2.4-GHz wireless-over-fiber system using photonic active integrated antennas (PhAIAs). *IEEE Journal of Lightwave Technology*, 25(11):3358–3365, 2007.

[134] S. Sohr, R. Rieske, K. Nieweglowski, and K. J. Wolter. Assembly tolerant design of multi-cell laser power converters for wafer-level photonic packaging. In *Electronic Components and Technology Conference (ECTC), 2013 IEEE 63rd*, pages 1866–1873. IEEE, 2013.

[135] V. A. Soifer and M. A. Golub. *Laser beam mode selection by computer generated holograms*. CRC Press, 1994.

[136] H. J. Song, K. Ajito, A. Wakatsuki, Y. Muramoto, N. Kukutsu, Y. Kado, and T. Nagatsuma. Terahertz wireless communication link at 300 GHz. In *Microwave Photonics (MWP), 2010 IEEE Topical Meeting on*, pages 42–45. IEEE, 2010.

[137] M. R. Stan, P. D. Franzon, S. C. Goldstein, J. C. Lach, and M. M. Ziegler. Molecular electronics: From devices and interconnect to circuits and architecture. *Proceedings of the IEEE*, 91(11):1940–1957, 2003.

[138] A. Stöhr, S. Babiel, P. J. Cannard, B. Charbonnier, F. van Dijk, S. Fedderwitz, D. Moodie, L. Pavlovic, L. Ponnampalam, C. C. Renaud, et al. Millimeter-wave photonic components for broadband wireless systems. *IEEE Transactions on Microwave Theory and Techniques*, 58(11):3071–3082, 2010.

[139] A. Stöhr, K. I. Kitayama, and D. Jäger. Full-duplex fiber-optic RF subcarrier transmission using a dual-function modulator/photodetector. *IEEE Transactions on Microwave Theory and Techniques*, 47(7):1338–1341, 1999.

[140] C. Tang, J. Yu, X. Li, N. Chi, J. Xiao, Y. Tian, and J. Zhang. A 30 Gb/s full-duplex bi-directional transmission optical wireless-over fiber integration system at W-band. *Optics Express*, 22(1):239–245, 2014.

[141] L. Thévenaz. Slow and fast light in optical fibres. *Nature Photonics*, 2(8):474, 2008.

[142] C. A. Thraskias, E. N. Lallas, N. Neumann, L. Schares, B. J. Offrein, R. Henker, D. Plettemeier, F. Ellinger, J. Leuthold, and I. Tomkos. Survey of photonic and plasmonic interconnect technologies for intra-datacenter and high-performance computing communications. *IEEE Communications Surveys & Tutorials*, 2018.

[143] D. Tosi, S. Poeggel, G. Leen, and E. Lewis. Adaptive filter-based interrogation of high-sensitivity fiber optic Fabry-Perot interferometry sensors. *Sensors and Actuators A: Physical*, 206:144–150, 2014.

[144] E. Uccelli, N. Daix, L. Czornomaz, C. D, C. Rossel, M. Sousa, H. Siegwart, C. Marchiori, J. M. Hartmann, and J. Fompeyrine. III/V layer growth on Si and Ge surfaces for direct wafer bonding as a path for hybrid CMOS. In *Silicon-Germanium Technology and Device Meeting (ISTDM), 2014 7th International*, pages 25–26, June 2014.

[145] D. Vantrease, R. Schreiber, M. Monchiero, M. McLaren, N. P. Jouppi, M. Fiorentino, A. Davis, N. Binkert, R. G. Beausoleil, and J. H. Ahn. Corona: System implications of emerging nanophotonic technology. In *ACM SIGARCH Computer Architecture News*, volume 36, pages 153–164. IEEE Computer Society, 2008.

[146] T. Venugopalan, T. Sun, and K. T. V. Grattan. Long period grating-based humidity sensor for potential structural health monitoring. *Sensors and Actuators A: Physical*, 148(1):57–62, 2008.

[147] D. von der Linde. Characterization of the noise in Continuously operating Mode-Locked Lasers. *Applied Physics B: Photophysics and Laser Chemistry*, 39(2), 1986.

[148] M. Wächter, M. Nagel, and H. Kurz. Metallic slit waveguide for dispersion-free low-loss terahertz signal transmission. *Applied Physics Letters*, 90(6):1111, 2007.

[149] A. Wakatsuki, Y. Muramoto, and T. Ishibashi. Development of terahertz-wave photomixer module using a uni-traveling-carrier photodiode. *NTT Technical Review*, 10(2), 2012.

[150] J. Wang, M. K. Haldar, L. Li, and F. V. C. Mendis. Enhancement of modulation bandwidth of laser diodes by injection locking. *IEEE Photonics Technology Letters*, 8(1):34–36, Jan 1996.

[151] J. Wang and K. Petermann. Small signal analysis for dispersive optical fiber communication systems. *IEEE Journal of Lightwave Technology*, 10(1):96–100, 1992.

[152] Y. Wang, J. Dostalek, and W. Knoll. Magnetic nanoparticle-enhanced biosensor based on grating-coupled surface plasmon resonance. *Analytical chemistry*, 83(16):6202–6207, 2011.

[153] A. G. Weber, W. Ronghan, E. H. Bottcher, M. Schell, and D. Bimberg. Measurement and simulation of the turn-on delay time jitter in gain-switched semiconductor lasers. *IEEE journal of quantum electronics*, 28(2):441–446, 1992.

[154] L. D. Westbrook and D. G. Moodie. Simultaneous bi-directional analogue fibre-optic transmission using an electroabsorption modulator. *Electronics Letters*, 32(19):1806–1807, 1996.

[155] A. E. Willner, H. Huang, Y. Yan, Y. Ren, N. Ahmed, G. Xie, C. Bao, L. Li, Y. Cao, Z. Zhao, et al. Optical communications using orbital angular momentum beams. *Advances in Optics and Photonics*, 7(1):66–106, 2015.

[156] P. J. Winzer and R. J. Essiambre. Advanced optical modulation formats. *Proceedings of the IEEE*, 94(5):952–985, 2006.

[157] R. Wu, V. R. Supradeepa, C. M. Long, D. E. Leaird, and A. M. Weiner. Generation of very flat optical frequency combs from continuous-wave lasers using cascaded intensity and phase modulators driven by tailored radio frequency waveforms. *Optics letters*, 35(19):3234–3236, 2010.

[158] X. Wu, Y. Ye, W. Zhang, W. Liu, M. Nikdast, X. Wang, and J. Xu. Union: A unified inter/intra-chip optical network for chip multiprocessors. In *Proceedings of the 2010 IEEE/ACM International Symposium on Nanoscale Architectures*, pages 35–40. IEEE Press, 2010.

[159] Y. Y. Xie, Q. Kan, C. Xu, Y. X. Zhu, C. X. Wang, and H. D. Chen. Low threshold current single-fundamental-mode photonic crystal VCSELs. *IEEE Photonics Technology Letters*, 24(6):464–466, 2012.

[160] Y. Yashchyshyn, S. Malyshev, A. Chizh, P. Bajurko, and J. Modelski. Study of active integrated photonic antenna. In *Antennas and Propagation, 2009. EuCAP 2009. 3rd European Conference on*, pages 3507–3510. IEEE, 2009.

[161] S. Yu. Potentials and challenges of using orbital angular momentum communications in optical interconnects. *Optics express*, 23(3):3075–3087, 2015.

[162] J. J. Zayhowski and J. Harrison. *Handbook of Photonics*, chapter Miniature Solid-State Lasers, pages 326 – 393. CRC Press, 1997.

[163] W. Zhang and R. A. Minasian. Widely tunable single-passband microwave photonic filter based on stimulated brillouin scattering. *IEEE Photonics Technology Letters*, 23(21):1775, 2011.

[164] X. Zhang and A. Louri. A multilayer nanophotonic interconnection network for on-chip many-core communications. In *Proceedings of the 47th Design Automation Conference*, pages 156–161. ACM, 2010.

[165] N. Zhao, X. Li, G. Li, and J. M. Kahn. Capacity limits of spatially multiplexed free-space communication. *Nature photonics*, 9(12):822, 2015.